DOTTORATO DI RICERCA IN

Scienze Biomediche

CICLO XXXVIII - PNRR NextGenerationEU

A novel strategy to target colorectal cancer and the tumour microenvironment

Settore Scientifico Disciplinare

MEDS-26/D

Dottorando/a

Dott.ssa Propato Arianna Pia

Supervisore

Prof.ssa Luconi Michaela

Coordinatore

Prof. Chiti Fabrizio

Table of contents

1. Introduction

1.1 Large intestine: structure, development and function

The large intestine, together with the stomach and small intestine, is part of the gastrointestinal system, which is responsible for a wide range of functions, including digestion, absorption, excretion and protection against pathogens. In particular, the large intestine plays a key role in stool elimination, absorption of water, electrolytes and residual nutrients and is the site of the intestinal microbiota, which contributes significantly to the overall health of the individual (Cheng et al., 2010; Maqbool, 2023). Anatomically, the large intestine is divided into distinct segments: the cecum, which receive partially digested and undigested material and transfer into the colon; the colon; and the rectum, where feces are stored prior to excretion.

The colon, which is the focus of this thesis, originates at the ileocecal valve and can be distinguished into proximal and distal colon. The proximal colon includes the ascending colon and the proximal two-third of the transverse colon, whereas the distal colon consists of the distal third of the transverse colon, the descending colon and the sigmoid colon (Bhatia et al., 2025; Maqbool, 2023).

The ascending colon derives from the embryonic midgut and is therefore perfused by the superior mesenteric artery and innervated by nerves arising from the superior mesenteric plexus. It extends from the cecum to the hepatic flexure into the peritoneum and is involved in the support of microbial digestion and in the absorption of electrolytes, water and nutrients, supported by a higher presence of colonocytes. The ascending colon is characterised by a thin and less dense mucus layer, which represents the first line of defence in the colon. This is well balanced by an active immune surveillance, reflected

by increased expression of immune-related proteins, a fundamental feature given the high exposure of this region to the microbiota and dietary antigens (Maqbool, 2023; Sung et al., 2025).

In contrast, the descending colon derives from embryonic hindgut and is vascularised by the inferior mesenteric artery and innervated by the inferior mesenteric plexus. It runs distally and posteriorly from the splenic flexure to the sigma and is responsible for final water absorption. Compared to the proximal colon, it displays a thicker and denser mucus layer, supported by a higher abundance of goblet cells involved in mucin production. This is associated with increased expression of mucus-associate proteins MUC2 and MUC3 and a faster turnover of mucins, which together ensure a physical barrier protecting intestinal integrity from bacterial invasion. Additionally, the descending colon has more proliferative crypts than the proximal colon, a feature that may contribute to the higher incidence of cancerous lesions observed in this region (Sung et al., 2025).

The transverse colon displays mixed embryological, vascular, and neural characteristics, reflecting its anatomical position between the proximal and distal colon: its proximal two-thirds derive from the midgut, while the distal third originates from the hindgut. As a result of its predominantly midgut origin, it shares a similar bacterial composition to that of the ascending colon. It is the longest segment of the large intestine, extending from the hepatic flexure to the splenic flexure and, by supporting the greater omentum, exhibits varying degree of mobility that facilitate the transit of luminal material from ascending to descending colon (Bhatia et al., 2025; Maqbool, 2023; Roy et al., 2021).

Finally, the sigmoid colon is a mobile, S-shaped structure derived from hindgut, which connects the descending colon to the rectum and refines the functions performed by the preceding colonic portion. Thanks to strong peristaltic contractions, it allows the storage

of solid stool in the rectum, via the rectosigmoid sphincter, and initiates the defecation reflex (Harkins & Sajjad, 2025).

From a histological perspective, the intestinal wall is organised into four distinct layers: *mucosa*, *submucosa*, *muscularis propria* and *serosa*.

Starting from the outermost and moving inward, the *serosa* is the first layer. It has a protective function and consists of mesothelium, a monolayer of squamous epithelial cells. Beneath the *serosa* and separated by a thin layer of connective tissue, lies the *muscularis propria*, which is organised into an inner circular layer and an outer longitudinal layer of smooth muscle cells, with the Auerbach plexus - part of the enteric nervous system - interposed between them. It is responsible for involuntary peristaltic movement. The *submucosa* is composed of inflammatory cells, blood and lymphatics vessels and Meissner plexus (Bhatia et al., 2025; Rao & Wang, 2010).

The innermost layer is the *mucosa*, which consists of the intestinal epithelium, the *lamina propria* and the *muscularis mucosae* (Maqbool, 2023). The *lamina propria* is a subepithelial connective tissue rich in lymph nodes, while the *muscularis mucosae* consists in a smooth muscle cells layer (Rao & Wang, 2010).

The intestinal epithelium consists of a single layer of cells and its integrity is protected by an outer layer of mucus and junctional complexes, such as tight junctions, adherens junctions and desmosomes (Vancamelbeke & Vermeire, 2017). It is one of the most rapidly self-renewing tissues in the human body. In the colon, the epithelium is organised into crypts which contain pluripotent stem cells at their base (Figure 1). While functions development acquired by the gastrointestinal tract begins around the 24th week of foetal development, crypt formation and cellular differentiation start at the 12th week, with the intestinal architecture resembling that of the adult by 22 weeks (Bhatia et al., 2025). Stem cells, identified by the expression of the Lgr5 marker, are responsible for epithelial

renewal and for maintaining the hierarchical organisation of differentiated cell types, which is essential for proper tissue structure and function (Nguyen et al., 2025; Sato et al., 2009). Cell differentiation occurs through the generation of transit-amplifying cells, a population of progenitor cells that undergo rapid proliferation and migrate upward along the crypt axis. During this process, they progressively undergo terminal differentiation into specialised mature epithelial lineages, whose relative proportions vary depending on the specific region of the colon (Nguyen et al., 2025; Sung et al., 2025). Among these, colonocytes and goblet cells are the most abundant, characterised by absorptive and secretory functions, respectively. Colonocytes are characterised by short microvilli that increase the absorptive surface area and are primarily responsible for the absorption of fluids, electrolytes, and bacterial metabolites, as well as for the metabolism of short-chain fatty acids, thereby supporting colonic and microbiota homeostasis (Blachier et al., 2018; Nguyen et al., 2025). Goblet cells secrete mucins that form the mucus layer, which protects the epithelium and facilitates feces lubrication.

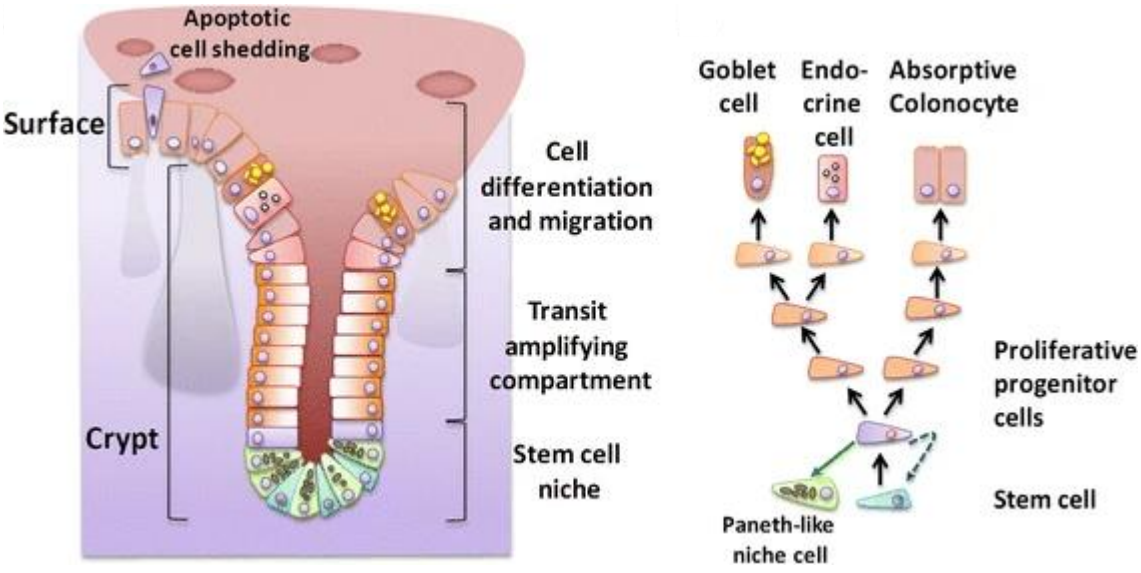

Figure 1. Cellular organisation of the colonic epithelium crypts. Reprinted from Pereira et al. 2016.

Other cell types are less abundant but remain essential for normal colonic function. Paneth-like cells, interspersed with stem cells at the base of the colonic crypts, secrete antimicrobial peptides, regulate the local microbiota, and contribute to the maintenance of epithelial integrity. In addition, enteroendocrine cells, which account for approximately 1% of the colonic epithelium, are believed to play a role in maintaining stem cell quiescence and function as microenvironmental sensors that regulate intestinal motility, secretion and appetite (Nguyen et al., 2025). Finally, M cells within the follicle-associated epithelium and tuft cells represent rare cell types: M cells are specialised for intraluminal antigen sampling and presentation to the immune system, whereas tuft cells act as chemosensory sentinels for parasite detection. Together with intraepithelial lymphocytes, they contribute to mucosal immune defence (Maqbool, 2023; Nguyen et al., 2025).

1.2 Colorectal cancer

The World Health Organisation (WHO) defines colorectal cancer (CRC) as a "type of cancer that affects the colon (large intestine) or rectum". More than 90% of CRC are adenocarcinomas originating from mucosal epithelial cells (Alzahrani et al., 2021).

1.2.1 Epidemiology and risk factors

GLOBOCAN 2022, an online database from the Global Cancer Observatory of the International Agency for Research on Cancer (IARC) - a specialised agency of the WHO - estimates CRC as the third cancer in terms of incidence and mortality worldwide, in both sexes (Figure 2).

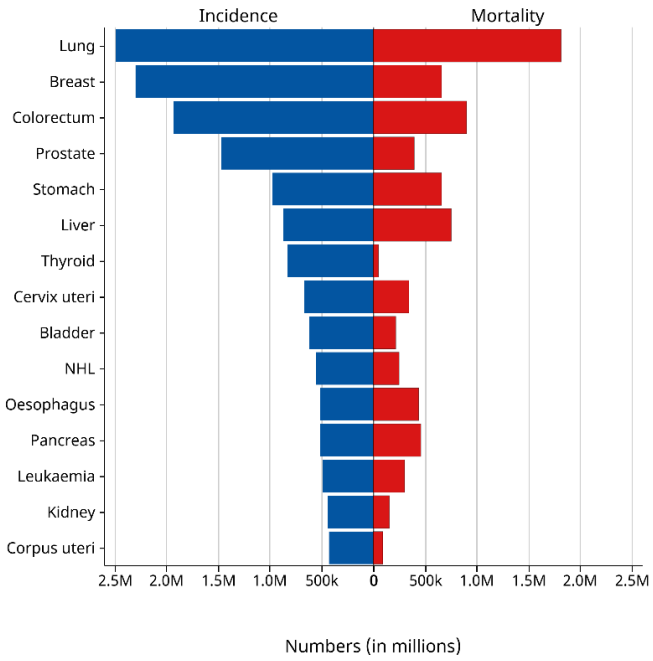

Figure 2. Absolute numbers in terms of incidence and mortality of the top 15 cancers in 2022, considering both sexes and all ages. Adapted from Cancer Today, IARC (data version Globocan 2022).

In 2022, more than 1.9 million new cases and more than 900,000 CRC-related deaths were recorded globally, with a higher prevalence in males than in females, with a male to female ratio of approximately 1.2:1 for both incidence and mortality (Cancer (IARC), s.d.). The five-year survival rate is 90 % for localised colorectal cancer compared to 63 % for all stages of disease and to 14% for metastatic CRC (Singh et al., 2025). When evaluating the Human Development Index (HDI), IARC data show that CRC is more prevalent in developed than in developing countries (Figure 3).

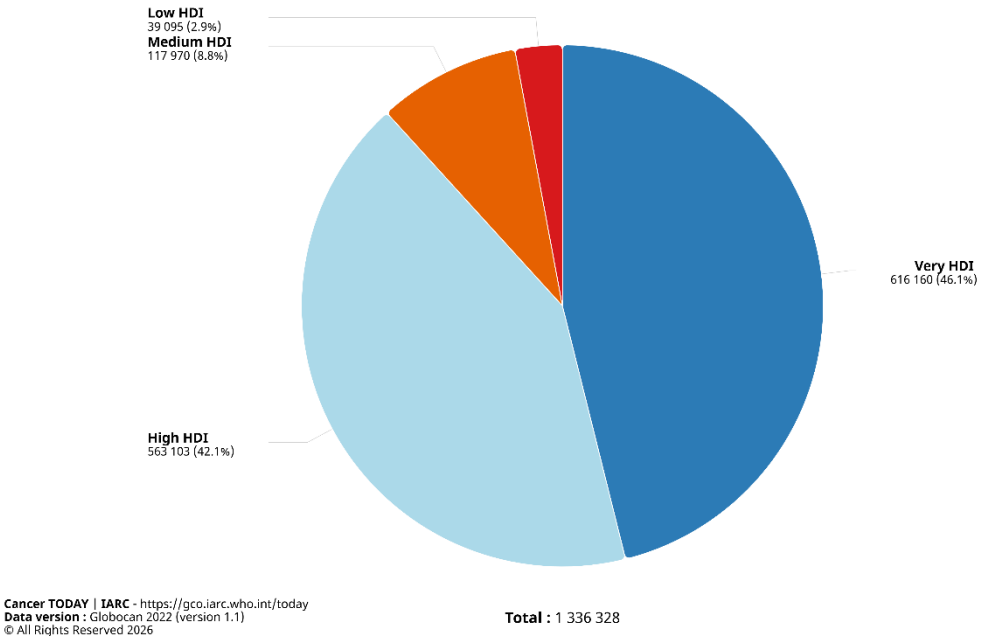

Figure 3. Absolute numbers of CRC incidence stratified by HDI, including both sexes and individuals aged between 0-74 years, for the year 2022. Adapted from Cancer Today, IARC (data version Globocan 2022).

Considering both sexes and all age groups, Oceania, Europe and Northern America exhibit higher age-standardised incidence and mortality rates. In particular, Oceania reports an incidence and mortality rate of 31.11 and 9.2 cases per 100,000 people, respectively. Europe shows the highest cumulative risk for both incidence and mortality, estimated at 3.6% and 1.3%, respectively. In contrast, continents with a lower HDI, such as Asia and Africa, present the lowest age-standardised incidence rates (12.6 and 7.1 cases per 100,000, respectively) as well as lower mortality rates (4.9 and 4.3 cases per 100,000) (Cancer (IARC), s.d.). These differences may be partly explained by genetic susceptibility, but are largely driven by socioeconomic factors, including dietary habits characterised by high-fat diet and consumption of red and processed meat, as well as alcohol use, tobacco smoking, environmental exposures, sedentary lifestyle and increased life expectancy (Akimoto et al., 2021; Thrumurthy et al., 2016).

Countries with historically higher CRC incidence have experienced stable or slightly declining trends, largely due to the implementation of effective screening programs; it is estimated that there will be a decreased rate of new cases by 2050, compared to 2022, in countries with a very high and high HDI (+44.3% and +79% respectively). On the other hand, countries with lower incidence rates - such as Japan and China - are showing a rising burden of the disease. It is estimated that there will be a 148.7% increase in new cases by 2050, compared to 2022, in low HDI countries. This increase likely reflects changes in the exposure to risk factors associated with urbanisation and the adoption of Western dietary and lifestyle habits (Akimoto et al., 2021; Cancer (IARC), s.d.; Matsuda et al., 2025).

CRC is more commonly diagnosed after the age of 65; however, the incidence of early-onset CRC (< 50 years) has been increasing globally in recent years (2.8 cases per 100,000). Among individuals younger than 40 years, Oceania reports the highest age-standardised incidence rate (1.9 cases per 100,000). In contrast, when considering individuals up to 50 years of age, Northern America exhibits the highest incidence rate, reaching 7.6 cases per 100,000. Europe ranks third in terms of early-onset CRC incidence, with an age-standardised rate of 3.8 cases per 100,000 individuals under 50 years of age (Akimoto et al., 2021; Cancer (IARC), s.d.). Considering US mortality data from "Surveillance, Epidemiology, and End Results" (SEER) database, supported by the National Cancer Institute (NCI), CRC is the only among the five leading cancers to show an increasing mortality rate in young adults, rising by 1.1% annually over the past 20 years (Siegel et al., 2026).

Early-onset CRC (EO-CRC) is emerging as a growing concern in countries that have recently undergone rapid westernisation (Akimoto et al., 2021). However, a major

limitation of the current evidence is that much of it derives from case-control studies or small cohorts with limited statistical power. Data from large-scale prospective studies suggest that increasing adiposity - reflected in rising obesity rate among young adults - along with smoking, alcohol consumption, and sedentary lifestyle, represent key risk factors for EO-CRC, largely overlapping with those observed in late-onset disease (Laskar et al., 2025). According to projections from “Cancer Tomorrow” (IARC), the number of estimated new colorectal cancer cases among individuals aged 20-49 years is expected to increase globally by 20.9% by 2050. In particular, Oceania and Northern America exhibit increases of 32.0% and 16.6%, respectively. Notably, Africa is expected to experience a marked increase of 107.4%, reflecting the ongoing upward trend in CRC incidence across the continent. In contrast, Europe is projected to show a decline of 20.5% in new cases within this age group (Cancer (IARC), s.d.) .

Besides ages and gender already highlighted, there are some risk factors that cannot be modified as the previous listed, such as ethnicity, positive family history of CRC or, even more so EO-CRC, a history of colon polyps, diabetes mellitus (Sawicki et al., 2021) and a personal history of colorectal cancer or inflammatory bowel disease (IBD). The chronic inflammation found in IBD (ulcerative colitis or Crohn’s disease) often produces dysplasia that does not imply malignancy but increases the likelihood of cells becoming anaplastic and forming a tumour (Mármol et al., 2017); individuals with this disease are estimated to have 1%, 2% and 5% risk of developing CRC after 10, 20 and > 20 years from diagnosis, respectively (Faye et al., 2022).

With regard to ethnicity, the issue is complex. Higher incidence and mortality rates in certain ethnic minorities, such as African Americans, are linked to disparities in participation to clinical trials, accessibility to screening programs and healthcare service in general and, in addition, to inequalities in socioeconomic status, dietary habits and

lifestyles, dictated by economic opportunities and neighbourhood environment. Together, these factors contribute to metabolic and biological alterations that increase the risk of CRC (Carethers, 2021).

The gut microbiome is also influent in terms of cancer risks. The dysbiosis, in which the balance between host and microbiota is disturbed in favour of proinflammatory bacteria is a condition that can be caused by antibiotic treatment or diet and is one of the most probable causes of inflammatory bowel disease or colorectal cancer. In addition, the toxic metabolites of some bacteria - e.g., *Fusobacterium nucleatum*, *Escherichia Coli* and *Bacteroides fragilis* - lead to a perturbation of intestinal barrier through DNA damage, suppression of immune response and dysregulation of oncogenic pathways (Sawicki et al., 2021; Singh et al., 2025).

1.2.2 Pathogenesis of colorectal cancer

The development of CRC - excluding hereditary non-polyposis CRC (HNPCC) and inflammation-driven CRC - is a multistep process that typically begins with the formation of polyps, defined as benign precursor lesions arising from the colonic *mucosa* and protruding into the intestinal lumen. These lesions are characterised by dysplastic epithelium, which have variable potential for malignancy. Malignant polyps are characterised by the presence of cancer cells invading through the *muscularis mucosa* into the underlying *submucosa* (Sawicki et al., 2021). The progression model underlying CRC pathogenesis was proposed by Fearon and Vogelstein in 1990 and is commonly referred to as the adenoma-carcinoma sequence. This model describes the malignant transformation of adenomatous polyps to adenocarcinoma, passing through dysplastic and hyperplastic changes caused by a multigene, clonal evolution and selection. *APC* (*Adenomatous Polyposis Coli*), *KRAS*, and *TP53* were identified as the key genes in

which mutations or epigenetic dysregulations contribute to the evolution of colon cancer (Fearon & Vogelstein, 1990) (Figure 4). Although later studies have validated this model, they have also demonstrated that colorectal tumorigenesis involves a broader spectrum of genetic alterations: the earliest event is commonly a mutation in the tumour suppressor gene *APC*, initiating adenoma formation, but this is subsequently accompanied by sequential mutations in oncogenes, additional tumour suppressor genes, and mismatch repair genes, which will be examined in the next section.

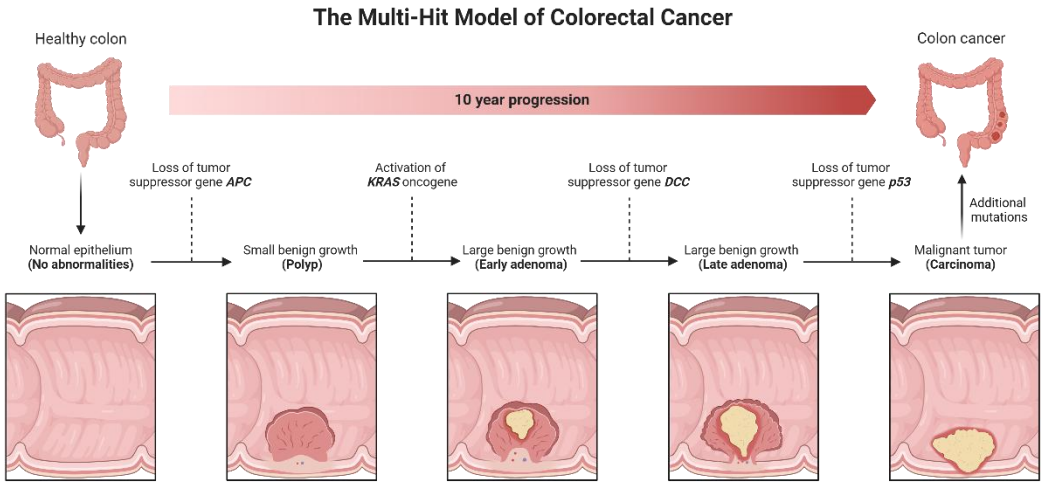

Figure 4. The adenoma-carcinoma sequence of colorectal cancer. Retrieved from BioRender (2026).

Morphologically, polyps can be classified as either pedunculated or sessile. Pedunculated polyps are those attached to the colonic *mucosa*, while sessile polyps grow in a more flattened pattern over the *mucosa*. Studies have shown that those polyps ≤ 5 mm have irrelevant risk of malignancy. Polyps with a depth of submucosal invasion > 1 mm are significantly associated with lymph node metastasis (Aarons et al., 2014).

Histologically, colon polyps are classified into two main categories: non-neoplastic (hamartomatous, hyperplastic and inflammatory polyps) and neoplastic (adenomatous)

polyps. Adenomatous polyps are responsible for 95% of colorectal cancers, but it is estimated that only about 5% of polyps progress to CRC (Sawicki et al., 2021). The sequence from precancerous adenoma to invasive and metastatic carcinoma requires several years during which somatic mutations cumulate. The process is often indolent and can be diagnosed after its clinical manifestation even 10 years or longer after the onset, when adenomas have progressed to the carcinoma stage (Requena & Garcia-Buitrago, 2020). The risk of malignant transformation increases with advancing age, larger polyp size, and higher degrees of dysplasia. In particular, dysplastic polyps measuring more than 1-2 cm in diameter are considered unfavourable prognostic factors (Sawicki et al., 2021).

In 2019, the World Health Organisation published the 5th edition of the Classification of Tumours of the Digestive System, which remains the current reference standard. One of the most significant updates was the introduction of the term "sessile serrated lesion" (SSL), replacing the previous designation "sessile serrated adenoma/polyp". Despite the serrated pathway has similar outcomes to adenocarcinoma, accounting for up to 30% sporadic CRCs, many of these lesions, indeed, do not have polypoid growth and so the conventional morphological dysplasia typical of an adenoma, justifying the revised nomenclature (Ahadi et al., 2021). During their evolution, sessile serrated lesions may show colorectal adenomas features or "serrated dysplasia". According to WHO Classification, the serrated lesions are categorised into four categories: hyperplastic polyps (HPPs), sessile serrated lesions (SSL) with or without dysplasia, traditional serrated adenomas (TSAs) and unclassified serrated adenomas. HPPs account for approximately 60-75% of serrated lesions; they are typically small (< 5 mm), flat, and predominantly located in the distal colon. SSLs represent 20-35% of serrated lesions, with

dysplasia observed in approximately 4-8% of cases. They are more frequently located in the proximal colon and generally measure 8-10 mm in diameter. TSAs are the least common subtype, usually measure < 5 mm, and are more often found in the distal colon. Although the serrated pathway does not follow the conventional adenoma-carcinoma sequence, these lesions have been strongly associated with *BRAF*^{V600E}-mutated carcinomas and are frequently linked to microsatellite instability and CpG methylator phenotype (Aiderus et al., 2024).

1.2.3 Molecular pathways involved in the carcinogenesis of colorectal cancer

CRC is a heterogeneous disease characterised by a multilevel molecular complexity (Sawicki et al., 2021). The molecular pathways involved in carcinogenesis can be basically included in three types (Harada & Morlote, 2020): chromosomal instability (CIN), microsatellite instability (MSI) and CpG methylator phenotype (CIMP).

1.2.3.1 Chromosomal instability (CIN pathway)

The CIN pathway is responsible for 85% of CRCs (Q. Li et al., 2024) and is characterised by aneuploidy, DNA amplifications, somatic copy number alterations (SCNAs), gains, deletions, structural rearrangement and loss of heterozygosity at tumour suppressor gene loci. CIN has been associated with inactivating mutations in *APC, SMAD4* and *TP53* genes and activating mutations in *KRAS* and *PIK3CA* genes, unbalancing the oncogene/tumour suppressor equilibrium and facilitating the adenoma-carcinoma sequence described by Fearon and Vogelstein's model (Harada & Morlote, 2020; Müller et al., 2016). The key pathways involved in CIN tumours are the Wnt, MAPK (mitogen-activating protein kinase), TGF-β (Transforming Growth Factor-beta), PI3K/Akt and p53 pathways (Harada & Morlote, 2020; Mármol et al., 2017).

Wnt/β-catenin pathway

In the absence of Wnt, ligand of the transmembrane Frizzled family receptor, β-catenin is phosphorylated resulting in its degradation by APC-dependent destruction complex (consisting of APC, Axin, the kinases glycogen synthase kinase GSK3β and casein kinase CK1α) in the cytoplasm; as a consequence, migration of β-catenin to the nucleus is prevented enabling the association between transcription factors TCF/LEF (T-cell and lymphoid enhancer factors) and transcriptional repressors TLE (Transducing-like enhancers)/Groucho. Conversely, the Wnt pathway is activated when Wnt protein binds its receptor and LRP (Lipoprotein Receptor-related Proteins) co-receptors, thus recruiting Dishevelled proteins and degrading the destruction complex by detaching Axin. In this condition, β-catenin accumulates in the nucleus, binds TCF/LEF by displacing TLE/Groucho and activates transcription of genes, such as *MYC* and *CCND1* (Cyclin D1 encoding gene) and genes related to the epithelial-mesenchymal transition (EMT) (Zhan et al., 2017). The key genomic aberration in 80% of adenomas and CRC, related to the hyperactivation of Wnt signalling pathway, is *APC* biallelic mutation that causes the translocation of β-catenin to the nucleus and drives the transcription of genes implicated in tumorigenesis and invasion. Additionally, approximately 5-10% of sporadic CRCs show activating mutations in other Wnt signalling components, such as *CTNNB1* (β-catenin-encoding gene) (Müller et al., 2016).

MAPK pathway

The MAPK pathway is activated by receptor tyrosine kinases. Activating mutation in one of the signalling molecules involved in this pathway, such as KRAS, RAF, or ERK, leads to a constitutive activation of the pathway resulting in uncontrolled cell proliferation

(Harada & Morlote, 2020). *KRAS (Kirsten rat sarcoma viral oncogene homolog)* is mutated in approximately 30% of cases, most frequently at codon 12, resulting in a constitutively active enzyme. This leads to a constitutive activation of downstream KRAS signalling through a cascade that sequentially involves RAF, MEK and MAPK/ERK (Q. Li et al., 2024; Müller et al., 2016). Moreover, *KRAS* mutations have been reported to promote a glycolytic metabolic phenotype, disrupt the physiological differences in microbiota composition between the ascending and descending colon, altering the intestinal microbial ecosystem, and facilitate liver metastasis (Meng et al., 2021).

TGF-β pathway

Chromosomal alterations are strongly associated with the CIN pathway in CRC. Allelic loss at 18q21.1 site, encoding the tumour suppressor genes *SMAD2* and *SMAD4,* is found in up to 60% of CRC cases. These genes are normally involved in apoptosis, cell cycle and EMT and are subjected to the main genomic aberrations related to the TGF-β pathway in colorectal cancer (Mármol et al., 2017).

PI3K/Akt signalling pathway

This signalling pathway is related to glucose metabolism in CRC. In normal cells, PI3K is activated downstream of receptor tyrosine kinases, leading to the conversion of phosphatidylinositol-4,5-bisphosphate (PIP2) into phosphatidylinositol-3,4,5-trisphosphate (PIP3) and the subsequent activating phosphorylation of the serine/threonine kinase Akt. Activated Akt, in turn, stimulates mTORC1 through phosphorylation, thereby promoting cell proliferation, protein synthesis, survival, motility and angiogenesis. In CRC, aberrant activation of this pathway is driven, in approximately one-third of cases, by missense mutations in the *PIK3CA* gene during the

adenoma-carcinoma transition. These mutations have been associated with chemoresistance and poor clinical prognosis. In addition, another common mechanism leading to pathway dysregulation involves loss of function mutations in the *PTEN* gene, which normally acts as a negative regulator of PI3K signalling (Leiphrakpam & Are, 2024).

p53 pathway

The p53 pathway is predominantly disrupted by allelic loss of chromosome 17p, where is the locus of *TP53* gene, or by missense mutations within the gene itself. *TP53* is a tumour suppressor gene that plays a central role in multiple cellular processes, including cell cycle regulation, DNA repair and the induction of apoptosis in response to DNA damage. p53 impairment is one of the last events in the adenoma-carcinoma sequence and is progressively associated with the advancement of the histological stages of malignant lesions, being detected in approximately 50-75% of CRCs (Worthley & Leggett, 2010).

1.2.3.2 Microsatellite instability (MSI pathway)

Microsatellites are non-coding tandem repeats of 2-6 base-pairs of DNA. Microsatellite instability is caused by loss of function in mismatch repair genes and thus, abnormal functioning of the DNA mismatch repair (MMR) mechanism. This condition promotes the accumulation of errors in microsatellite regions due to the slippage of DNA polymerase occurring during DNA replication (Harada & Morlote, 2020; Q. Li et al., 2024). Loss of expression of MMR genes can be caused by spontaneous mutations (even of only one of the mismatch repair genes among *MLH1*, *MSH2*, *MSH6*, or *PMS2*), by *MLH1* silencing through hypermethylation of CpG islands, or by germinal mutations,

such as those found in Lynch syndrome, the most common hereditary colon cancer related syndrome that increases EO-CRC risk to about 80%. Mutations can affect non-coding and coding regions causing the development of tumours by the alteration of the reading frames of oncogenes or tumour suppressor genes codified in microsatellites (Harada & Morlote, 2020). Many CRCs retain an intact MMR system but have frameshift mutations within microsatellite regions. To classify MSI, a standardised panel of five microsatellite markers has been established, allowing tumours to be categorised as MSI-high (MSI-H), MSI-low (MSI-L), or microsatellite stable (MSS), based on the presence of instability at more than two, one, or none of these loci, respectively. MSI-H tumours exhibit pronounced genomic instability independently of the CIN pathway (Worthley & Leggett, 2010). MSI accounts for approximately 15% of sporadic CRCs and arises most frequently in the proximal colon. Among hypermutated CRCs, around 75% are characterised by hypermethylation of the *MLH1* promoter, whereas the remaining 25% are associated with somatic mutations in MMR genes and mutations in DNA polymerase ε (Harada & Morlote, 2020).

1.2.3.3 CpG methylator phenotype (CIMP pathway)

The CpG island methylator phenotype is characterised by epigenetic instability. The main characteristic of CIMP-positive tumours is the widespread hypermethylation of numerous promoters, resulting in transcriptional silencing of more than 100 tumour suppressor genes (Requena & Garcia-Buitrago, 2020). While CIN and MSI pathways are mutually exclusive in CRC, CIMP-high tumours are frequently associated with MSI-H status, due to hypermethylation of the *MLH1* promoter region, and with *BRAF*^{V600E} mutation (Requena & Garcia-Buitrago, 2020; Sawicki et al., 2021). Epigenetic instability accounts for almost 20% of sporadic CRCs and has been associated with a favourable response to

chemotherapy (Q. Li et al., 2024). Clinically, CIMP-positive tumours tend to arise in the proximal colon, occur at an older age and show a prevalence in females (Harada & Morlote, 2020).

1.2.4 Consensus molecular subtypes of colorectal cancer

CRC Subtyping Consortium integrated the molecular diversity within CRC into four Consensus Molecular Subtypes of CRC (Agrawal et al., 2025; Müller et al., 2016):

- CMS1 or MSI-immune subtype (14% of CRCs). It is characterised by MSI and consequent hypermutation, CIMP phenotype, immune activation, frequent *BRAF* mutations, low levels of SCNAs, and poor prognosis.

- CMS2 or canonical subtype (37% of CRCs). It is defined by CIN pathway with prominent activation of Wnt and MYC signalling pathways. It is MSS, exhibits high levels of SCNAs, increased epidermal growth factor receptor (EGFR) signalling and *TP53* mutations.

- CMS3 or metabolic subtype (13% of CRCs). It displays features of the CIN pathway with mild Wnt and MYC signalling activation, a low number of SCNAs and moderate to low levels of hypermutation/MSI with frequent *KRAS* and *PIK3CA* mutations. It is associated with CIMP-low phenotype.

- CMS4 or mesenchymal subtype (23% of CRCs). These tumours are characterised by CIN pathway, activation of TGF-β signalling and increased expression of genes related to epithelial-mesenchymal transition, matrix remodelling, stromal infiltration and angiogenesis. It exhibits high levels of SCNAs and is associated with the worst relapse-free and overall survival among all CMS subtypes.

1.2.5 Etiologic classification of colorectal cancer

1.2.5.1 Sporadic CRC

About 70% of CRCs derived from somatic point mutations with no genetic burden. The molecular pathogenesis is heterogeneous, but there is often a specific succession of mutational events starting with *APC* mutation (70% of cases), followed by mutations in *KRAS*, *TP53* and *DCC*, that leads to the formation of an adenoma that evolves in carcinoma within a period of approximately ten years, (Mármol et al., 2017). As mentioned in sections 1.2.2, up to 30% of sporadic CRCs have their origin in serrated polyps and have a significant malignant potential or are caused by mutations or epigenetic changes of mismatch repair genes.

1.2.5.2 Inherited CRC

About 10% of CRCs develop in presence of hereditary syndromes: the two main diseases are familial adenomatous polyposis (FAP) and hereditary non-polyposis colorectal cancer (HNPCC).

FAP is an autosomal dominant disease that accounts for about 1% of CRC cases. It is characterised by the formation of malignant polyps in the colon caused by a former germline mutation in the *APC* gene, followed by additional mutations, such as *KRAS* and *TP53*. Individuals with FAP often develop hundreds to thousands of unrecognised and untreated polyps during their teens, 90% of which evolve into colon cancer - without a proper colectomy - frequently diagnosed at the age of 40 (Goosenberg et al., 2025; Menon & Kasi, 2025; Sawicki et al., 2021). An important and less aggressive variant is attenuated FAP (AFAP) that is caused by specific mutations in *APC* gene - different from the ones in FAP - and is characterised by fewer polyps, later age of adenoma appearance (generally

55-58), earlier diagnosis and a lower cancer risk (Goosenberg et al., 2025; Menon & Kasi, 2025).

HNPCC is a non- polyposis autosomal dominant form of inherited CRC, also known as Lynch Syndrome. This condition is related to germline mutations of mismatch repair genes, such as *PMS2, MLH1, MSH6* and *MSH2,* 3' deletions in the *EPCAM* gene or hypermethylation of one promoter allele of *MLH1* gene. Lynch syndrome can be found in approximately 3% of all CRCs. The MSI pathway is characteristic of HNPCC patients: *PMS2* and *MSH6* variants are the most prevalent, but with a lower risk to develop CRC, while *MLH1* and *MSH2* are less common but associate with an higher risk (Eroglu et al., 2025; Goosenberg et al., 2025). Mismatch repair deficiency and Lynch syndrome are easy to detect thanks to microsatellite instability testing. Patients with Lynch Syndrome have about 20% and 80% risk of developing CRC by the age of 50 and 85, respectively and an increased risk of multiple cancers (Sawicki et al., 2021).

A subset of people with attenuated polyposis syndrome, has biallelic mutations in *MUTYH* gene (MUTYH- associated polyposis, MAP) that encodes a DNA glycosylase enzyme involved in base-excision repair of oxidative DNA damage. MAP causes a recessively inherited polyposis condition characterised by a slightly increased risk of developing CRC and polyps/adenomas; is generally characterised by the development of an average of 50 polyps, including serrated adenomas, hyperplastic or sessile serrated polyps, and mixed hyperplastic-adenomatous polyps (Goosenberg et al., 2025; Menon & Kasi, 2025)

Other inherited syndromes (Goosenberg et al., 2025) responsible of the increasing risk of developing CRC are:

- Hereditary mixed polyposis syndrome (*GREM1* gene mutation). It is characterised by the development of numerous polyps at young age, increasing the risk of developing CRC up to 25%.
- Sessile serrated polyposis syndrome, already described in section 2.2
- The hamartomatous polyposis syndromes (autosomal dominant disorders): Peutz-Jeghers (germline mutations of the *STK11*, a tumour suppressor gene) Juvenile polyposis (*SMAD4* mutation), PTEN hamartoma tumour syndrome. A hamartoma consists of disorganised growth of normal appearing cells in native tissue and is generally considered benign with very rare progression to cancer.

1.2.5.3 Familial CRC

Familial CRCs account for about 3% of cases and cannot be classified as inherited because they cannot be included in the inherited cancer variants, despite familial clustering. These forms are likely driven by common genetic polymorphisms in genes involved in metabolic pathways or in genes whose expression is influenced by environmental or genetic factors which increase the susceptibility to CRC. Familial Colorectal Cancer Type X (FCCTX) is an autosomal-dominant disorder closely resembling Lynch syndrome, but characterised by being microsatellite stable (MSI-L/MSS) and by the absence of MMR deficiency (Giglia & Chu, 2016; Jasperson et al., 2010). Compared to Lynch syndrome, these patients have a lower risk to develop CRC and no additional risk to develop other cancer. Putative mutations in type X families include *RSP20*, *SEMA4A*, *HNRNPA0*, and *WIF1* genes. A family history of CRC increases the risk of developing CRC that depends on both inherited genetic predisposition and lifestyle. Crucial information is the generational distance of the relatives, the age at which the first-degree relatives developed colorectal cancer, the

number of family members diagnosed with CRC, family co-occurrence of other tumours and personal history of cancer (Sawicki et al., 2021). Individuals having a first-degree relative > 50 years with CRC, increases the risk of developing CRC by 2-3-fold. Individuals with a first-degree relative with CRC diagnosed under 45 years of age or two first-degree relatives affected by CRC, have a 3-6-fold CRC risk compared to the general population. The CRC risk is conferred by 10 to 170 common SNPs: each variant alone is not highly penetrant individually, but has additive risk when found together with others (Giglia & Chu, 2016).

1.2.6 Colorectal cancer symptoms, diagnosis and prognosis

The most common presenting features of colorectal cancer include rectal bleeding, abdominal pain, abdominal or rectal masses, changes in bowel habit (diarrhoea or constipation), anaemia, unexplained weight loss and thrombocytosis (Hamilton & Bailey, 2023). CRC may develop either on the right or left side of the colon, with differences in clinical presentation, progression and overall survival. Right sided tumours more commonly present loss weight, abdominal pain or mass, and anaemia. In contrast, left-sided CRCs are frequently associated with rectal bleeding or mucus discharge and altered bowel habits, including intestinal obstruction and diarrhoea (Benedix et al., 2010). Some studies suggest that the presence or absence of individual symptoms does not significantly alter the likelihood of CRC detection. However, other evidence indicates that the co-occurrence of multiple symptoms may improve diagnostic sensitivity and specificity. In the context of CRC management, patients diagnosed before the onset of clinical manifestations or at the earliest appearance of symptoms generally have a substantially better prognosis (Sawicki et al., 2021)

CRC screening modalities include stool-based tests, such as the faecal immunochemical test (FIT), the high-sensitivity guaiac faecal occult blood test (gFOBT), and multitarget stool DNA assays; direct visualization tests (endoscopy-based procedures such as colonoscopy and sigmoidoscopy); and indirect visualization tests, such as computed tomographic colonography (Lopes et al., 2024). According to the World Gastroenterology Organisation, these tests must be integrated with the assessment of family medical history of cancer in first-, second- and third-degree relatives, taking into account the age of diagnosis. For example, in individuals with hereditary syndromes (e.g., Lynch Syndrome), surveillance should begin at the age of 20-25 or 10 years earlier than the youngest age of CRC diagnosis in the family, with colonoscopy performed every 1-2 years.

Annual FIT has been shown to be a non-invasive, cost-effective method for CRC screening. It involves the use of antibodies against the human haemoglobin to evaluate the presence of occult blood in just one sample of the stool. It is a more sensitive method compared to gFOBT. The threshold (μg of haemoglobin/gram of feces) for a positive test varies worldwide, based on the follow-up programmes of different countries. Multitarget stool DNA (mts DNA) combines FIT with DNA-based markers, including mutations in *KRAS*, methylation in bone morphogenetic protein 3 (BMP3) and N-Myc downstream-regulated gene 4 protein (NDRG4) (McCabe et al., 2025).

Colonoscopy has the highest sensitivity and specificity for the diagnosis of early-stage CRC, allows the evaluation of the entire large intestine and the terminal part of the small intestine and can also be used to perform a biopsy for histopathologic examination. Flexible sigmoidoscopy enables the visualization of the left colon and the polyps' removal. However, if adenomas are identified, a subsequent colonoscopy is mandatory.

While endoscopy is ideal for detecting cancer at an early stage and removing adenomas, it is an invasive method that can be partially replaced by colon capsule test (CC). This is a minimally invasive and painless imaging method that does not allow for biopsy. It consists of a wireless, pill-sized camera that is ingested to enable visualisation of the colon. This approach may be considered for patients in whom colonoscopy is contraindicated or declined; however, it is not recommended as a standard method for colorectal cancer screening (Lopes et al., 2024).

Computed tomographic colonography (CTC) is also a non-invasive method enabling the visualization of the entire colon and rectum, but the sensitivity is significantly lower than that of colonoscopy for the detection of polyps < 8 mm and sessile serrated lesions (Lopes et al., 2024; Sawicki et al., 2021).

Declining adherence to stool-based screening tests has prompted the development of blood-based assays using biomarkers such as circulating microRNAs, plasma proteins, cytokines and epigenetic alterations. “Epi proColon,” which detects *SEPTIN9* methylation in circulating tumour DNA, was approved by the FDA in 2016 for average-risk individuals who decline other screening options. In 2024, the FDA approved another cell-free DNA blood-based test, “Shield,” which detects aberrant methylation, genomic alterations, and DNA fragmentations (Symonds et al., 2025).

The European Commission Initiative on Colorectal Cancer working group (ECICC WG) has provided guidelines on colorectal cancer screening and diagnosis. It suggests participation in organised population-based screening programmes for asymptomatic adults at average risk aged 50-69 years old. The recommended approach consists in the faecal immunochemical test every two years up to the age of 74. In some cases,

endoscopy-based screening until 69 years of age, with colonoscopy every 15 years or sigmoidoscopy every 10 years may be considered.

After diagnosis, it is important to determine the spreading of cancer and the survival statistics in a process called “staging”. The pathological staging system most often used for colorectal cancer is the “American Joint Committee on Cancer (AJCC) TNM system”. In 2016 was published the 8th - and current - edition of AJCC Cancer Staging Manual. The earliest stage of colorectal cancer is called stage 0 and it is followed by stages I, IIA/B/C, IIIA/B/C and IVA/B/C, indicating a progressively increased diffusion of the tumour. The TNM classification is assigned by the combination (stage grouping) of three different information: the extent of the tumour (T) through the layers of colon wall or rectum, the dissemination to nearby lymph node (N) and the presence of metastasis (M). The numbers or letters after T, N and M provide more details (Table 1). In the updated edition AJCC, new M stage (M1c) and TNM stage were added (IVC, any T, any N, M1c) and the prognostic staging of CRC was implemented (Tong et al., 2018).

TNM system (8th edition)		Description
T	**TX**	The primary tumour cannot be evaluated.
	T0 (T plus zero)	No evidence of cancer in the colon or rectum.
	Tis	Carcinoma *in situ*.
	T1	Spread into the *submucosa*.
	T2	Spread into the *muscularis propria*.
	T3	Spread through the *muscularis propria* and into the fat tissue.
	T4a	Spread into the surface of the visceral peritoneum.
	T4b	Spread to other organs or structures.
N	**NX**	The regional lymph nodes cannot be evaluated.
	N0 (N plus zero)	No spread to regional lymph nodes.
	N1a	1 regional lymph node involved
	N1b	2 or 3 regional lymph nodes involved.
	N1c	Submucosal, mesangial or peritoneum-covered tumour deposits.
	N2a	4 to 6 regional lymph nodes metastases.
	N2b	7 or more regional lymph nodes metastases.
M	**M0(M plus zero)**	No metastasis.
	M1a	Metastasis limited to one organ site.
	M1b	Metastasis to more the one organ site.
	M1c	The cancer has spread to the peritoneal surface with or without metastasis of other organs.

Table 1. The table shows the 8th edition of AJCC TNM staging system. Adapted from Tong et al. 2018.

SEER database provides survival statistics for different types of cancer. The 5-year survival rate (2015–2021) for individuals diagnosed with localised colorectal cancer is 91%. For cancers that have spread to surrounding tissues, organs, and/or regional lymph

nodes, the 5-year survival rate is 74.3%. When the disease has metastasised to distant sites, the 5-year survival rate decreases to 15%. These estimates are based on the stage at diagnosis and do not account for other factors that may influence prognosis, such as age, overall health status, response to treatment, surgical resection, tumour location (left- vs. right-side), and other clinical features (SEER explorer).

1.2.7 Current therapeutic approaches for CRC

There is no universal therapeutic regimen for all patients with colorectal cancer, owing to its marked genetic heterogeneity and the complex interplay of multiple molecular pathways involved in tumour initiation, progression, and treatment response.

Surgical resection of resectable tumours represents the first-line therapeutic option for CRC. However, approximately 1/4 of CRC cases are diagnosed at an advanced stage, precluding curative surgical intervention. In patients with unresectable disease or those who are unfit for surgery, radiotherapy and chemotherapy constitute the main strategies to achieve tumour debulking and to limit tumour growth and invasiveness. In selected cases, radiotherapy and/or chemotherapy may be administered either before or after surgery as neoadjuvant or adjuvant treatments, respectively. Typically, neoadjuvant therapy is a preoperative treatment aimed at reducing the risk of recurrence and increasing survival rates. Routine approaches include radiation, chemotherapy, or combined chemoradiation. Reaching a complete tumour remission has always been the main goal of neoadjuvant therapy. Current chemotherapeutic regimens include fluorouracil (5-FU), oxaliplatin, irinotecan, trifluridine-tipiracil, fluoropyrimidines, and capecitabine, with combination therapies representing the standard first-line approach (Kumar et al., 2023; Xie et al., 2020).

Targeted therapy has revolutionised the neoadjuvant efficacy into therapy for CRC, selectively acting on cancer cells by inhibiting key pathways involved in cell proliferation, migration, and survival. It can also modulate the tumour microenvironment to enhance the immune response and suppress tumour growth. Target agents consist in small molecules - typically with a molecular weight < 900 Da - that can penetrate cells and act on intracellular targets, as well as monoclonal antibodies, which exert their effects extracellularly by binding to cell-surface receptors or molecules (Xie et al., 2020). Multiple pathways involved in CRC can be considered potential targets. The first agents approved in 2004 by the Food and Drug Administration (FDA) for CRC treatment were Cetuximab and Bevacizumab.

Cetuximab is a chimeric monoclonal antibody that target EGFR related pathways (MAPK, PI3K/AKT and JAK/STAT3), inducing the internalization and degradation of the receptor that is overexpressed in 25-77% of CRC cases (Manzi et al., 2023). Cetuximab triggers antibody-dependent T-cell-mediated cytotoxicity and shows the risk of skin toxicity and anaemia. Panitumumab is a fully humanised antibody developed to bypass immunogenic reactions. Both Cetuximab and Panitumumab are FDA-approved for the first-line treatment of CRC. Alterations or downregulation of EGFR pathway decrease anti-EGFR effectiveness. In particular, Cetuximab is ineffective in patients with *KRAS* mutations and is less used in right-sided tumours because they express lower levels of EGFR (Manzi et al., 2023; Xie et al., 2020).

Bevacizumab is a humanised monoclonal antibody targeting Vascular Endothelial Growth Factor-A (VEGF-A), a pivotal molecule involved in neovascularization. As an antiangiogenic agent, it is FDA-approved for the first-line treatment of metastatic CRC, an angiogenesis-dependent cancer. Bevacizumab is more commonly combined with fluoropyrimidine-based chemotherapy, however emerging personalised combinations

have been explored, particularly for those patients who develop resistance to conventional chemotherapy (H. Chen et al., 2025). Its efficacy has been demonstrated also for those patients with *KRAS* mutations and for both sided tumours (Xie et al., 2020).

Other anti-VEGF/VEGFR (Vascular Endothelial Growth Factor Receptor) agents approved by FDA for the second-line treatment of CRC, include aflibercept, ramucirumab and regorafenib. Aflibercept is a recombinant fusion protein composed by VEGFR-1 and VEGFR-2 extracellular domain that prevents the binding of VEGFR ligands to their receptors. By inhibiting angiogenic signalling, aflibercept reduces tumour vascular density, suppresses neovascular growth and promotes vascular remodelling. These effects enhance tumour sensitivity to chemotherapy and radiotherapy. Ramucirumab is a fully humanised monoclonal antibody that targets VEGFR-2, the main mediator of VEGF-A (Colombo & Porretto, 2023). Regorafenib is the only multikinase inhibitor currently approved for the treatment of metastatic colorectal cancer (mCRC). It targets multiple kinases involved in multiple pathways, including neovascularisation. Clinical studies have demonstrated that regorafenib prolongs overall survival in patients who have previously received first- and second-line standard therapies. However, further studies are needed to better define its therapeutic benefit (Matsumoto et al., 2023; H. Yan et al., 2024).

Other FDA-approved drugs for the CRC treatment targeting TME are the immune checkpoint inhibitors (ICIs) pembrolizumab, nivolumab and ipilimumab. Immune escape is one of the ten hallmarks of cancer described by Hanahan and Weinberg (Hanahan & Weinberg, 2011) that is mediated by secretion of immunosuppressive factors (e.g., Interleukin-6, IL-6), recruitment of immunosuppressive cells, downregulation of the major histocompatibility complex (MHC) and T-cell inactivation through the activation of immune checkpoint receptors on T-cell surface. These receptors include Programmed

cell death protein 1 (PD-1) and Cytotoxic T lymphocyte antigen 4 (CTLA-4). Conventionally, Programmed cell death 1 ligand 1 or ligand 2 (PD-L1 or PD-L2), expressed on the surface of antigen presenting cells or tumour cells, engage with PD-1 expressed on the surface of T-cells to induce inhibitory signalling to the downstream pathways such as the PI3K/AKT pathway. Otherwise, CTLA-4 competitively binds to CD80/86 with higher affinity than CD28, a molecule involved in T-cell activation, inhibiting co-stimulation (He & Xu, 2020). Metastatic CRCs express high levels of PD-L1 and present a great amount of PD-1-expressing CD4+ T regulatory (T_{reg}) cells which suppress the activity of other immune cells. Immune checkpoint inhibitors aim to enhance immune surveillance by blocking CTLA-4 or the PD-L1/PD-1 interaction (Xie et al., 2020).

Pembrolizumab and nivolumab are humanised anti-PD-1 antibodies approved by FDA in 2017 for the treatment of MSI-H or MMR-deficient (dMMR) metastatic CRC. Ipilimumab is a CTL-4 inhibitor and evidence suggests that a combination of nivolumab and ipilimumab is ideal for chemotherapy-refractory MSI-H or dMMR metastatic CRC (He & Xu, 2020). Unfortunately, the response rate to ICIs is not uniform across the different CRC subtypes. MSI-H/dMMR tumours represent only a small proportion of metastatic CRC cases and many patients either fail to respond or eventually develop resistance or adverse events. (S. Yan et al., 2024)

1.2.8 Key CRC models in research

1.2.8.1 *In vitro* models

There are more than 150 human cell lines currently collected in different worldwide banks and commonly used as *in vitro* models for basic research or preclinical studies on colorectal cancer (Kranjec et al., 2026; Sveen et al., 2018). Despite the development of

increasingly complex *in vitro* models that are more pathophysiologically representative of the organ of interest, their unlimited availability in monolayer culture and the maintenance of similarities to the tissue of origin at the time of biopsy, make cell lines culture a model that is still functional and convenient (Kranjec et al., 2026; Masters, 2000). Over time, i*n vitro* models diverge from the original tumour due to serial passages, clones' selection, artificial culture conditions and lack of crosstalk with microenvironment. Although it is known that few of these models accurately recapitulate the heterogeneity of the molecular subtypes of CRC, the classification of primary tumours into the four CMSs has made it possible to categorise the different cell lines, according to their expression profile, in order to optimise specific preclinical studies, especially those regarding the drug sensitivity (G. Rizzo et al., 2021; Sveen et al., 2018). The most commonly used CRC cell lines include HCT116, HT29, SW480, LoVo, DLD-1, Caco-2 and LS174T, which collectively comprise the different molecular subtypes and stages of clinical progression (Al-Kabani et al., 2025).

An evolution of 2D culture is represented by three-dimensional CRC cell-line derived-spheroid models, which more closely mimic the architecture of a tumour niche. These models exhibit a multi-layered structure with a hypoxic, nutrient-deprived and necrotic core, enabling more accurate investigation of drug penetration and therapeutic response. This system also offers increased complexity through the generation of multicellular spheroids incorporating TME cells. Although spheroids more closely resemble the *in vivo* system and are easy to generate, they share the same limitations with monolayer cultures, particularly in terms of molecular and clonal heterogeneity. In addition, they show a shorter culture lifespan in their 3D structure and difficulties in standardising their size - and therefore the extent of the necrotic fraction - as well as in distinguishing the responses

of the different cell populations within multicellular spheroids, unless the employment of fluorescent tagging or single-cell analysis. Furthermore, although spheroids are subject to a gradient of oxygen, nutrients and potentially therapeutic agents, they are avascular and protocols for their integration into “organ-on-a-chip” microfluidic systems are not yet widely standardised (Al-Kabani et al., 2025).

The ongoing search for preclinical models that reflect and preserve tumour heterogeneity, while maintaining the advantage of a long-term and biobanking culture system typical of cell lines, has led to the generation of patient-derived organoids (PDOs). These are developed from pluripotent stem cells (PSCs), induced pluripotent stem cells (iPSCs) or adult stem cells (ASCs) and, thanks to the organ specificity of the derived cells that self-organise into a three-dimensional structure, preserve the mutational and phenotypic scenario of the original tumour (G. Rizzo et al., 2021; E. Wang et al., 2022). This enables the application of this model not only in basic and translational research to investigate tumour dynamics, clonal evolution and tumour microenvironment interactions, but also in clinical research, particularly in the context of personalized and precision medicine (Al-Kabani et al., 2025). In the context of CRC, improvements were made after the identification of Lgr5 as a marker of intestinal stem cells. Hans Clevers' group pioneered the generation of mouse intestinal organoids derived from adult stem cells, demonstrating the ability of single Lgr5+ multipotent stem cells, residing at the intestinal crypts, to generate a self-organised, continuously expanding epithelial structure with self-renewing stem cells and multi-lineage differentiation in enterocytes, goblet, Paneth and enteroendocrine cells mimicking the *in vivo* small intestine epithelium, definable as a mini-gut (Sato et al., 2009). This was achieved by isolating the crypts, resuspending them in laminin-rich Matrigel to support growth and prevent anoikis, and growing them in a

medium (called ENR medium) containing R-spondin 1 (a Wnt agonist and a ligand for Lgr5), Epidermal Growth Factor (to support intestinal proliferation) and Noggin, all of which are essential factors for maintaining stem cells in long-term culture (Sato et al., 2009; Sato & Clevers, 2013). Subsequently, the group succeeded in adapting the above-mentioned culture protocol to establish a long-term culture for murine and human colon epithelium, even starting from adenomas and carcinomas (Sato et al., 2011). Specifically, mouse colon organoids are generated by mild digestion of colonic crypts to physically separate the basal compartment, which contains stem and proliferative cells, from the upper compartment, composed of mature and differentiated cells that could interfere with normal organoid growth. Since colonic organoids do not produce sufficient amounts of Wnt ligands - essential for the maintenance of stem cells and mainly produced by Paneth cells - the culture medium was optimized by adding recombinant Wnt-3A or Wnt-3A–conditioned medium (referred to as WENR medium). In contrast, the growth of human colonic crypts is supported by supplementing the WENR with gastrin, nicotinamide, A83-01 (an Alk5 inhibitor) and SB202190 (a p38 inhibitor), thereby improving the culture period and efficiency, promoting the maintenance of budding structures characteristic of proliferative organoids. In both mouse and human organoids, the presence of Wnt and/or inhibitors prevents complete differentiation into enterocytes and goblet/enteroendocrine cells, respectively. (Sato et al., 2011). Given that the earliest mutations triggering polyp formation occur in the Wnt signalling pathway - most notably in the tumour suppressor gene *APC* - the generation of *APC*-deficient $Lgr5^{+}$ stem cells at the crypt base has been used to initiate intestinal adenomas in mice (Barker et al., 2009). This approach enabled the isolation of intestinal adenomas for the establishment of cystic organoids as a model to study the malignancy. In adenoma-derived organoids, both R-spondin 1 and Noggin were shown to be dispensable for growth due to the constitutive activation of the Wnt

signalling pathway (Sato et al., 2011). These advances, together with the need arising from the inability of existing cell lines to fully recapitulate human colon cancer, prompted the optimisation of *in vitro* culture conditions developed for mouse intestinal adenomas for application to human colorectal cancer biopsies. These adjustments, included modulation of EGF supplementation and, once again, the omission of R-spondin 1 and Noggin, resulted in the generation of highly proliferative, irregular structures displaying limited differentiation towards goblet and enteroendocrine cells (Sato et al., 2011). The ability to introduce defined mutations into colon organoids (*APC, TP53, KRAS*^{G12D} and *SMAD4)* and to modulate culture conditions to mimic the intestinal niche enabled, for the first time, the *in vitro* recapitulation of the *in vivo* multi-hit model of colorectal carcinogenesis in terms of both histological features and *in vivo* tumorigenicity following transplantation (Drost et al., 2015; X. Li et al., 2014; Matano et al., 2015). Although PDOs are proving to be a versatile and promising model, several limitations must be considered. One of their main strengths, patient specificity, also represents a disadvantage, as findings obtained from a PDO line cannot be extended to others without further validation. In addition, close coordination with surgeons is required to obtain fresh biopsy material, which is essential to ensure a high success rate of organoid establishment. PDO generation is also time-consuming and expensive, largely due to the need for multiple media supplements and extracellular matrix support, and because many assays still require optimisation and standardisation. Moreover, organoids are non-vascularised structures and typically lack stromal and infiltrating immune components, as intestinal organoids recapitulate the epithelial compartment. Consequently, as also observed for spheroid models, PDOs do not fully reproduce mechanical signals (exogenous basement membrane do not fully recapitulate the complexity of the native ECM) nor the complex cross-talk with the surrounding tumour microenvironment, except when combined with

microfluidic platforms, co-cultured with patient-matched stromal cells, or integrated into air-liquid interface systems incorporating tumour-infiltrating lymphocytes or into *ex vivo* patient derived immuno-organoids (PD-IOs) interaction platforms (Al-Kabani et al., 2025; Esposito et al., 2024).

1.2.8.2 *In vivo* mouse models

To investigate CRC tumour-microenvironment-host interactions under less artificial conditions, murine models are widely employed, due to their well-characterised genetic and immunological features. Multiple models have been developed, reflecting the different factors that contribute to disease development (Al-Kabani et al., 2025). One of the earliest phenotypic events observed during colon carcinogenesis, identifiable through histological analysis of the colon *mucosa*, is the presence of single or multiple aberrant crypts. These are recognized as early neoplastic lesions characterised by a thickened layer of epithelial cells, a slit-shape lumen and an enlarged pericryptal space. They were first described by Bird in methylene-blue stained colon preparations of rodents treated with azoxymethane (AOM) (Bird, 1987, 1995; Figueiredo et al., 2009; McLellan & Bird, 1988). Carcinogen/irritant-induced colon cancer in rodents can cause sporadic CRC or inflammation-driven cancer in humans and it represents a very useful model to study tumorigenesis, microbiome influences and anti-inflammatory therapeutic approaches. The reactive metabolite MAM, resulting from the hydroxylation of AOM, an intermediate metabolite of dimethylhydrazine, causes DNA alkylation and point mutations and, after approximately 3 months of weekly intraperitoneal injections in immunocompetent mice, causes multiple colon tumours. It is often combined with dextran sulphate sodium (DSS), an irritant that induces repeated injuries and an inflammatory state, promoting the development of colitis-associated cancer (Al-Kabani et al., 2025). In addition to the

limited reproducibility in tumour yield and the mortality observed in mice undergoing testing, the main limitation of this model is that AOM/DSS-induced tumours are triggered by random mutations - particularly in KRAS or β-catenin pathways - and tend to remain microsatellite stable. As a result, this model does not fully recapitulate the adenoma-carcinoma sequence and the features of advanced CRC (Al-Kabani et al., 2025).

On the other hand, the ability to genetically modify mice has enabled the development of models that mirror the molecular events underlying the multi-hit theory of CRC development, allowing for controlled experimental studies. These genetically engineered mouse models (GEMMs) typically rely on tissue-specific Cre-lox or Cre^{ERT2} systems to induce gene deletion or mutation selectively and/or at specific times in the colonic epithelium of immunocompetent mice (Betzler et al., 2021). This approach allows for the generation of $APC^{Min/+}$ mice, which spontaneously develop adenomatous polyps that may progress to carcinoma, as well as triple-mutant (AKP) models through the combination of additional mutations that recapitulate the Fearon and Vogelstein sequence, such as alterations in *APC*, *KRAS*, and *TP53* (Al-Kabani et al., 2025; Bürtin et al., 2020). However, despite their precision, these highly targeted models do not fully capture the complexity of human tumours and the ability to metastasise. Studies have revealed that adding the *SMAD4* mutation *in vivo* (AKPS model) leads to the formation of metastases in distant organs and to a dysregulation of the gut microbiome that can promote the process (Gates et al., 2025). Germline allele manipulation and the crossbreeding of transgenic animals are time-consuming and expensive processes, subject to ethical and regulatory limitations. Even somatic genome editing approaches using CRISPR/Cas9 are associated with ethical concerns, particularly due to potential off-target effects and animal pain (Al-Kabani et al. 2025).

The search for preclinical models that accurately reproduces, in an *in vivo* context, the human tumour architecture and interactions with the stromal and immune microenvironment, ensuring unaltered CMS classification compared to the matched primary tumours, has led to the creation of cell line-derived (CDX) and patient-derived xenograft (PDX) models. They involved the utilization of human-derived material, particularly cell lines and patient tumour tissue respectively, in immunodeficient mice - particularly NOD/SCID and NOD/SCID/IL2γ-receptor null - to prevent rejection (Al-Kabani et al., 2025; G. Rizzo et al., 2021; E. Wang et al., 2022). Cell lines can be injected subcutaneously, orthotopically, intrasplenic or into the tail vein, depending on whether the experimental aim is to model primary tumour in the colon or metastatic dissemination (Al-Kabani et al., 2025). PDX are made through subcutaneous or orthotopic implantation of a minced tissue (25-30 mm^3) or single cell suspensions in a recipient immunodeficient mouse (F0 generation) and a subsequent reimplantation of the successfully obtained xenograft in additional generations. This system preserve an high molecular and histopathological fidelity of the original CRC tumour - PDX retains the positivity for cytokeratin 20 (CK20) and carcinoembryonic antigen (CEA) and negativity for CK7 - and the interaction between cancer and TME cells, allowing studies on the CMS subtypes and personalised medicine (Al-Kabani et al., 2025; G. Rizzo et al., 2021). The engraftment rate from CRC biopsies is around 60-80% and takes from 2-4 months (G. Rizzo et al., 2021; E. Wang et al., 2022). It was shown that engraftment time can be decreased thanks to patient-derived organoid xenografts (PDOX) and the possibility to do an *in vitro* pre-selection of the organoids to be implanted (E. Wang et al., 2022).

Strategies to overcome the lack of an adaptive immune response, preserving *in vivo* tumour-immune system interactions, include the use of humanised mouse models, in

which a functional human immune system is reconstituted with hematopoietic cells in the immunodeficient mice, as well as the use of syngeneic models. The latter involve the transplantation of murine cell lines, organoids, or mouse-derived CRC tumours either subcutaneously or orthotopically into immunocompetent mice. Among the most widely used syngeneic CRC models are CT26 and MC38, which are derived from carcinogen-induced tumours and partially recapitulate MSS and MSI CRC, respectively. However, neither model has *APC* mutations, which are present in the majority of human CRCs. Consequently, while these models are valuable tools for immunotherapy studies, they do not fully reflect the genetic and biological complexity of human colorectal cancer (Thomas et al., 2023).

1.3. The role of the tumour microenvironment in tumour progression: a focus on colorectal cancer

Tumour microenvironment (TME) is an ecosystem surrounding the tumours, implicated in tumorigenesis and in all the stages of cancer development, stimulating and facilitating cell proliferation, survival and invasiveness. On the other hand, cancer cells influence the TME through paracrine signals, modulating and recruiting various cell types to escape epithelial compartment, invade other spaces and promote immune suppression and tolerance (Arneth, 2019). In normal condition, stroma has anticancer activities, but tumour cells educate the stromal components to co-evolve and synthetise growth factors, cytokines, chemokines, proteases to accelerate the cancer progression and limit the delivery of anticancer drugs (F. Chen et al., 2015). The TME can promote the development of *de novo* resistance by promoting the dysregulation of oncogenes and

tumour suppressor genes, enhancing the expression of ATP-binding cassettes, sustaining cancer stemness, and conditioning tumour cells to adapt to extreme microenvironmental stresses (Fatima, 2025). In addition, stromal cells through the so-called “reverse Warburg effect”, increase aerobic glycolysis in the TME to generate products (e.g., lactate), which are taken by cancer cells and used for oxidative phosphorylation to increase ATP production and for biosynthetic pathways (Sabol et al., 2019). The TME consists of a complex and dynamic network of cellular and non-cellular components. It includes various cellular elements - such as immune cells, endothelial cells, fibroblasts, neuroendocrine cells, adipocytes, bone marrow-derived inflammatory cells, mesenchymal stem cells, and lymphocytes - as well as non-cellular components, including the blood and lymphatic vascular networks, the extracellular matrix (ECM), and a wide range of signalling molecules, like TGF-β, that interact with or infiltrate the tumour mass (Arneth, 2019; F. Chen et al., 2015).

The most representative immune cell type in the TME is the macrophage, in this context known as tumour-associated macrophage (TAM). Macrophages can adopt a M1 or M2 phenotype, considered anti- and pro-cancer phenotypes, respectively. The infiltration of M2-like macrophages suppresses antitumor immune responses, facilitates angiogenesis and the ECM remodelling (Fatima, 2025). Moreover, within the TME, the antitumor activity of lymphocytes is suppressed by cancer cells through multiple mechanisms, including the upregulations of immune checkpoints molecules PD-L1/PD-1. ICs are highly expressed on dysfunctional and exhausted cytotoxic T lymphocytes, significantly accumulated in the TME (Toor et al., 2020). Tumour cells express PD-L1 which binds PD-1 on the lymphocyte surface, inhibiting the immune reaction of immune cells. In addition, the TME can impair immune surveillance by recruiting immunosuppressive

populations, such as T_{reg} cells and myeloid-derived suppressor cells (MDSCs), and by compromising dendritic and natural killer cells, thereby reducing their ability to eliminate tumour cells (Fatima, 2025).

The endothelial cells - in this context known as tumour-associated endothelial cells - not only play a key role in promoting tumour angiogenesis, necessary for nutritional support and metastatic dissemination, but also exert immunoregulatory functions. They can selectively modulate immune cell trafficking, preferentially facilitating the recruitment of immunosuppressive cells over immune effector cells, thereby contributing to tumour immune evasion (Nagl et al., 2020).

Cancer-associated fibroblasts (CAFs), are a source of secreted factors, collectively called secretome, that promote tumour growth, angiogenesis, migration, invasiveness and especially immune escape. The main effect is the reduction of T-cells response through the secretion of IL-6, CXC-chemokine ligand 9 (CXCL9) and TGFβ. CAFs are the most effective cells in the ECM deposition and remodelling. ECM is a network of glycosaminoglycans and structural proteins and its rearrangement can increase tumour stiffness and activate pro-survival and proliferative signalling pathways, while also promoting hypoxia as a result of vascular compression and collapse. This hypoxic and mechanically altered microenvironment promotes tumour aggressiveness and drug resistance. In addition, ECM remodelling permits cancer cells migration and subsequent invasion, facilitating the development of metastases via multiple mechanisms, including the matrix production. ECM reorganisation also affects the trafficking of infiltrating leukocytes, further impairing anti-tumour immune responses (Sahai et al., 2020).

Bone marrow derived cells (BMDCs) recruited by the tumour through chemokines such as Stromal Cell-Derived Factor 1 (SDF-1), are implicated in tumour expansion via homing to the primary site. BMD macrophages, together with CAFs and hematopoietic progenitors, can be attracted by macrovesicles or molecules, secreted by tumour cells, to distant organs, contributing to the development of pre-metastatic niches. Approximately 20% of CAFs originate from bone marrow derived mesenchymal stem cells (F. Chen et al., 2015).

Tumour-resident or recruited mesenchymal stem cells (MSCs) can dynamically shift between anti-tumorigenic (MSC-1) and pro-tumorigenic (MSC-2) phenotypes, thereby exerting a dual role in cancer progression. MSCs-2 promote immunomodulation, tumour growth, angiogenesis, survival, neoplastic invasion and drug resistance. MSCs are highly plastic and exhibit the ability to differentiate in multiple cell lineages such as endothelial cells, fibroblasts and adipocytes, potentially contributing to the generation of cancer-associated stromal cells. Owing to their intrinsic capacity to home to and infiltrate the tumour stroma, MSCs are increasingly being explored as therapeutic delivery vectors in emerging anticancer strategies (Slama et al., 2023).

As discussed in this section, the non-cellular components of TME (ECM and blood vessels) play a pivotal role in cancer progression through a wide range of mechanisms.
In particular, the ECM is enriched with bioactive factors that regulate cell-cell and cell-matrix communication, adhesion, and proliferation. Through these biochemical and biomechanical interactions, it can influence cancer cell behaviour by modifying their physical properties and molecular composition.
Abnormalities in the blood vascular network are involved in multiple processes, such as angiogenesis, migration and metastasis. High metabolic demands of the tumour cells and

the disorganised structure of angiogenic vessels in the TME, cause the accumulation of H+ - in a process called acidosis - leading to the formation of hypoxic regions and a shift towards a glycolytic metabolism. The decrease of pH characterising acidosis stimulates cancer cells motility, drives the pro-tumorigenic activity of macrophages and fibroblasts and activates protease secretion, which facilitates tumour cell migration. Moreover, the formation of hypoxic areas, together with the poor organisation of blood vessels, compromises drug delivery and effectiveness (Arneth, 2019; Fatima, 2025).

The classification of colorectal cancer in the four consensus molecular subtypes (CMS1-4) mentioned before, depends not only on the differences in the cancer molecular expression, but also on the tumour microenvironment properties reflecting the site of development along the colorectum. Several genes used to classify the tumour subtypes are expressed by TME cells.

CMS1 tumours are characterised by a greater infiltration of immune cells and by the enrichment of gene expression signatures associated with immune response pathways, such as JAK-STAT, TNFα and NF-kβ, thus suggesting the relevance of immune component role in characterising the TME. Spatial transcriptomic studies also demonstrate a myofibroblasts prevalence in CMS1 subtype (Chowdhury et al., 2021; Valdeolivas et al., 2024).

CMS2 tumours are associated with an epithelial-cell lineage population, particularly TA cells and goblet cells. They usually develop in the descending colon and rectum and are characterised by the activation of classical oncogenic signalling pathways such as MYC and Wnt pathways. The former inhibits antitumor T-cell activation and enhances the production of interleukin 17 (IL-17) linked to CRC progression, the latter promotes the

expression of the immunosuppressive molecules CD47 and PD-L1 (Birbrair, 2020; Chowdhury et al., 2021).

CMS3 tumours are characterised by a metabolic signature and prevalent epithelial-cell cluster, mostly composed by enterocytes (Chowdhury et al., 2021). Spatial transcriptomics studies show that CMS3 signatures are restricted to the non-neoplastic mucosa, presenting normal-like expression patterns (Valdeolivas et al., 2024). *KRAS* mutated cells are more prevalent among CMS3 tumours and show enhanced glucose uptake and upregulation of the glucose transporter GLUT-1 which sustains the survival of cancer cells in a TME characterised by a low glucose condition (Birbrair, 2020).

CMS4 tumours display a mesenchymal signature, characterised by a prevalence of stromal cells - particularly CAFs - and immune cell clusters rather than a tumour epithelial-like phenotype. This subtype is associated with multiple features of an active TME, including matrix remodelling, TGF-β pathway activation, angiogenesis and a pro-inflammatory microenvironment with tumour-promoting immune cell populations (Chowdhury et al., 2021; Thanki et al., 2017).

In summary, CMS2 and CMS3 CRC subtypes are primarily characterised by intrinsic tumour epithelial transcriptomic signatures, whereas CMS1 and CMS4 display gene expression profiles largely shaped by tumour microenvironment components, particularly immune and stromal cell populations.

1.3.1 The adipose microenvironment and its role in CRC

Among the components of the TME, this thesis specifically focuses on adipose cells, with particular emphasis on their role in supporting colorectal cancer progression. The adipose tissue is composed of adipocytes, pericytes, endothelial cells, preadipocytes, fibroblasts, immune cells and adipose stem cells. It is a complex endocrine tissue, producing and

secreting hormones, growth factors and small cytokines called adipokines. In the last decade, adipocytes and their precursors have gained considerable attention as active contributors in the TME. Once regarded as passive energy store depots, adipocytes are now recognised as mediators of both local and systemic effects, influencing tumour initiation, growth, local invasion and metastasis through the release of more than 400 molecules, including adipokines, cytokines and extracellular vesicles (Duong et al., 2017).

Adipose tissue is classified in white adipose tissue (WAT), and brown adipose tissue (BAT). The former, which is the most predominant form in adults, can be localised subcutaneously (subcutaneous adipose tissue, SAT), surrounding visceral organs (visceral adipose tissue, VAT) or in the female breast (mammary adipose tissue, MAT). It constitutes the main energy reservoir - storing fatty acids in the adipocytes as neutral triglycerides - and plays a pivotal endocrine role in controlling metabolic homeostasis through adipokine secretion (Duong et al., 2017). Conversely, BAT, which is predominantly found in new-borns and, in adults, localised mainly in the paracervical and supraclavicular regions (Virtanen et al., 2009), acts as a thermodynamic organ. It mainly regulates thermogenesis by oxidizing fatty acids through mitochondrial respiration and dissipating energy as heat rather than ATP, a process mediated by the expression of uncoupling protein 1 (UCP-1) (A. Park et al., 2014). Recently it has been demonstrated that both adipocytes and the stromal vascular cells in adipose tissue can set up a strict crosstalk with the infiltrating cancer cells. This interaction reciprocally regulates and reprograms each cell type: adipose cells support tumour development and progression, while cancer cells influence adipose cells by reprogramming adipocytes into cancer-associated adipocytes (CAAs). CAAs offer an easily accessible reservoir of free fatty

acids as an energy source, facilitating tumour growth and survival. Under the influence of cancer cells, CAAs undergo delipidation, size reduction (due to an increase of lipolytic activity to satisfy the energy demand of proliferating tumour), dedifferentiation-like changes losing adipocyte terminal differentiation markers - acquiring a fibroblast-like phenotype - and increase of secretion of proteases, angiogenic factors and proinflammatory cytokines, such as IL-6, facilitating cancer invasiveness and aggressiveness (Figure 5) (J. Park et al., 2014). IL-6 binds to glycoprotein 130 (GP130) leading to the activation of JAK-STAT1/3, PI3K/AKT and MAPK pathways. Activation of STAT3 by CAAs, for example, promotes EMT. The PI3K/AKT pathway is involved in cell survival, cell cycle progression, cellular growth and is responsible for the development of a resistant phenotype (Vara et al., 2004); activation of MAPK pathway is involved in uncontrolled cell proliferation, resistance to apoptosis, inflammation and migration (Dhillon et al., 2007).

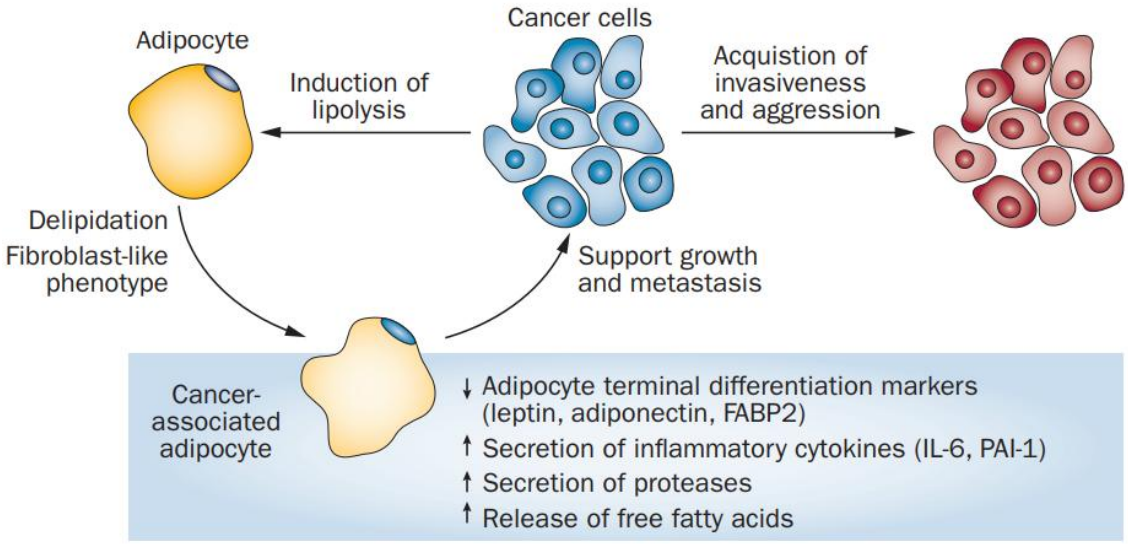

Figure 5. Reciprocal influence between cancer-associated adipocytes and cancer cells. Adapted from Park et al., 2014.

CAAs contribute to tumour progression also through the dysregulated secretion of adipokines within the tumour microenvironment (TME). In particular, leptin, upon binding to its receptor (ObR), activates several downstream signalling pathways—including JAK2, STAT3, MAPK, and PI3K—that regulate key oncogenic processes such as cell cycle progression, survival, invasion, migration, angiogenesis, and inflammation (Booth et al., 2015). Leptin can also upregulate stemness markers, favouring therapeutic resistance. Conversely, downregulation of adiponectin levels favour anabolic signals (Kim et al., 2026). Tumour cells become a sort of "metabolic parasites" of the normal adipocytes in the TME, inducing them to metabolic reprogramming into CAAs. This phenotypic shift is promoted by exposure of mature adipocytes to tumour cells or their paracrine pro-inflammatory and hypoxia-associated factors, such as tumour necrosis factor-α (TNF-α), interleukin-1β (IL-1β), IL-6, prostaglandin E_2 (PGE_2) and hypoxia-inducible factor 1α (HIF-1α). Moreover, cancer cells can exchange metabolites such as free fatty acids (FFAs), lactate, pyruvate, ketone bodies with adipocytes, affecting their metabolism and activity (Kim et al., 2026; Wu et al., 2019). Studies demonstrate that there is a reciprocal exchange: adipocytes in the TME undergo a constant lipolysis activation through the upregulation of genes involved in triglycerides hydrolysis, realising FFAs rapidly oxidised by tumour cells, accelerating cancer progression. In addition, FFAs are particularly enriched in oleate which can promote EMT, through the activation of TGF-β and Wnt pathway, and so metastatic dissemination. This lipid-enriched microenvironment reshapes the immune-metabolic programming of infiltrating effector T-cells, shifting their metabolism from glycolysis toward fatty acid oxidation (FAO). FAO is insufficient to meet the high energetic demand required for optimal effector function, thereby compromising their anti-tumour activity. Moreover, saturated FFAs can induce mitochondrial dysfunction and promote the accumulation of reactive

oxygen species (ROS) in effector T-cells, impairing oxidative phosphorylation and further weakening their function. In contrast, T_{reg} cells - characterised by high expression of the lipid-sensing nuclear receptor PPARγ - benefit from lipid-mediated signalling and preferentially rely on FAO, which supports their expansion and suppressive capacity. Collectively, these metabolic alterations contribute to the establishment of an immunosuppressive tumour microenvironment (Kim et al., 2026).

Colon is enveloped in the mesentery, which is constituted by connective and adipose tissue, thus it is in close contact with the visceral adipose tissue depots. Inflammatory bowel disease and obesity are characterised by an increase in submucosal fat deposition and both are associated with CRC incidence and mortality (Tabuso et al., 2017).

CRC is considered one of the obesity-related cancers by the World Cancer Research Fund (WCRF). According to GLOBOCAN 2022 estimates, CRC ranks fifth among obesity-related cancer cases worldwide, considering both sexes and all age groups and its geographical distribution mirrors the global incidence pattern of CRC (Cancer (IARC), s.d.).

As expected, *in vitro* studies using colon cancer cell lines have demonstrated that co-culture with adipocyte cell lines promotes their transdifferentiation to CAAs, while enhancing pro-survival, pro-migratory, pro-inflammatory, angiogenic, mitogenic, and anti-apoptotic effects (Olszańska et al., 2023; Tabuso et al., 2017). Moreover, it has been shown that human adipocytes within TME, isolated from colon cancer patients, release high concentrations of fatty acids that are subsequently taken up by colon cancer cells or organoids. This lipid transfer induces a metabolic switch that supports tumour cell survival under energy stress conditions. Specifically, cancer cells enhance autophagy and

mitochondrial FAO through AMPK activation, while simultaneously reducing lipogenesis and glucose-dependent respiration (Wen et al., 2017).

Adipose tissue also represents a major source of adult stem cells (ASCs). In colorectal cancer, the pro-malignant activity of ASCs is largely mediated through IL-6-dependent pathways. Indeed, the interaction between ASCs and cancer cells enhances IL-6 secretion by ASCs, thereby promoting tumour cell proliferation, upregulation of cancer stemness-related genes, angiogenesis, EMT and chronic inflammation. These effects are primarily driven by activation of the JAK2/STAT3 signalling pathway and the subsequent upregulation of VEGF, matrix metalloproteinases, and other pro-tumorigenic factors (Y.-X. Wang et al., 2019; Wei et al., 2015).

1.3.2 Tumour intestinal microbiota

The intestinal microbiota comprises approximately 100 trillion microorganisms that play a crucial role in maintaining overall health. It contributes to host homeostasis through multiple functions, including fermentation of dietary components, nutrient extraction and metabolism, modulation of the immune response, protection against external pathogens via the production of antimicrobial compounds and the biosynthesis of bioactive molecules. As discussed in section 1.2.1, the gut microbiota plays a pivotal role in the onset and progression of colorectal cancer. Alterations in its composition and function (dysbiosis) can promote a pro-tumorigenic environment by inducing local inflammation, generating genotoxic metabolites, disrupting epithelial barrier integrity and triggering dysregulated immune responses that collectively contribute to carcinogenesis (Hou et al., 2022). Meta-analyses have shown different microbial profiles in patients with CRC. Three distinct oncomicrobial community subtypes (OCSs) have been identified, each associated with specific tumour locations and molecular subtypes, further underscoring

the biological heterogeneity of the disease. For example, *Fusobacterium nucleatum*, which predominates in OCS1, has been strongly associated with CMS1 tumours. In CRC-associated microbiota, a dysbiotic shift is observed not only in microbial composition but also in metabolic output. This shift is characterised by increased amino acid fermentation and polyamine biosynthesis, alongside a reduced capacity for carbohydrate degradation and a decreased production of beneficial metabolites such as secondary bile acids and short-chain fatty acids (SCFAs) (C. Chen et al., 2025).

1.3.2.1 Short chain fatty acids and their role in normal mucosa and CRC

It is known that a balanced diet rich in fibres can stimulate microbial saccharolytic fermentation and the production of SFCAs, namely acetate, butyrate and propionate. SCFAs are quantitatively and metabolically the most important microbial end-products of the human colon fermentation process and have anti-inflammatory and antiproliferative properties. Bacteria with an almost exclusive saccharolytic metabolism, are generally considered to be beneficial (Yoon & Kim, 2018). Patients with CRC show low SCFAs production and, in particular, diminished levels of faecal butyrate and butyrate-producing bacteria (C. H. Park et al., 2018).

Butyrate represents the primary energy source for colonocytes and supports colonic epithelial homeostasis through mitochondrial β-oxidation. It also acts as a ligand for metabolite-sensing G protein-coupled receptors, including Free Fatty Acid Receptors 2 and 3, known also as GPR43 and GPR41, and GPR109A. Upon receptor binding, butyrate triggers downstream signalling cascades such as the MAPK pathway, thereby contributing to the regulation of inflammatory responses and the gut health (McNabney & Henagan, 2017a). In addition, butyrate contributes to the regulation of cell differentiation and apoptosis, while reducing tumour cell invasiveness and proliferation.

These effects are largely mediated by its function as a histone deacetylase inhibitor (HDACi), which leads to epigenetic reprogramming and the consequent suppression of multiple oncogenic signalling pathways (Yoon & Kim, 2018). It has been demonstrated that, through HDAC inhibition, butyrate can excessively activate the canonical oncogenic Wnt signalling pathway to levels that are incompatible with cell proliferation, instead triggering apoptosis (Bordonaro, 2025).While normal colonocytes rely on butyrate as a primary energy source, colorectal tumour cells undergo a metabolic reprogramming known as the Warburg effect, characterised by a shift from mitochondrial oxidative phosphorylation (OXPHOS) to glucose-dependent aerobic glycolysis. Consequently, mitochondrial fatty acid oxidation is progressively reduced, leading to the accumulation of short-chain fatty acids in the cytoplasm and nucleus. In this compartment, butyrate functions as a HDACi, promoting apoptosis in cancerous colonocytes and attenuating macrophage-driven inflammation by downregulating the production and secretion of pro-inflammatory cytokines in the gut. Moreover, butyrate may cause tumours cell apoptosis also through the binding to GPR109A receptor, leading to IL-18 expression, important for the differentiation of anti-inflammatory IL-10 producing T- cells and T_{reg} cells and for the inhibition of the NF-kβ signalling pathways (McNabney & Henagan, 2017a).

As mentioned in section 1.3.1, obesity and IBD are two conditions that increase the risk of CRC. In the context of obesity, the HDAC-inhibitory activity of butyrate has been linked to multiple beneficial effects on adipose tissue. These include the suppression of inflammation (also via GPR43/GPR41 receptor binding), upregulation of leptin synthesis, promotion of adipose tissue browning, and enhancement of adipocyte differentiation, contributing to improved insulin sensitivity (Ma et al., 2024; McNabney & Henagan, 2017a).

In patients with IBD, butyrate uptake and oxidation are impaired, compromising its protective functions. Chronic inflammation disrupts the integrity of the intestinal epithelial barrier, exposing the mucosa to pathogens and triggering immune responses. SCFAs help to preserve barrier function by maintaining tight junctions, enhancing mucus production, and promoting epithelial cell proliferation and differentiation to facilitate barrier repair. Additionally, SCFAs modulate immune responses by regulating IL-8 - a cytokine often elevated in IBD - and by influencing the immunomodulatory activity of T_{reg} cells (McNabney & Henagan, 2017a; Shin et al., 2023).

1.3.2.2 Current application of butyrate for the intestinal health

The tumour microenvironment has emerged as a central focus in cancer research, as it plays a crucial role in tumour initiation, progression, and therapeutic response. Promising TME-targeted strategies include modulation of acidosis, regulation of microbiota composition, interference with ECM-integrin signalling and control of inflammation (Arneth, 2019). Given the well-established role of intestinal microbiota dysbiosis in the onset and progression of colorectal cancer, it is reasonable to hypothesise that probiotics, next generation probiotics (NGP) and postbiotics used as adjuvant therapies, may contribute to the establishment and maintenance of a “non-carcinogenic” microbiome. Among the probiotics investigated in CRC management, lactic acid bacteria are the most extensively studied, particularly species belonging to the genera *Streptococcus*, *Enterococcus*, *Lactobacillus*, *Lactococcus* and *Bifidobacterium* (Kvakova et al., 2022). Several clinical trials have shown that preoperative oral administration of probiotics, combined with postoperative treatment, improves bowel function recovery after colorectal cancer surgery. This approach has been associated with an increased abundance of SCFA-producing bacteria, reduced postoperative infection rates, attenuation of

inflammatory responses, and, overall, faster recovery following tumour resection. NGPs are live, strain-specific microorganisms identified through comparative analyses of the microbiota in healthy individuals and patients with disease. Among these, SCFA-producing bacteria have emerged as promising NGP candidates in CRC management, both in preventive and therapeutic settings. *In vivo* animal studies using butyrate-producing bacteria have demonstrated reduced tumour progression through multiple mechanisms. These include activation of the GPR43 receptor, induction of apoptosis via modulation of the Wnt signalling pathway or inhibition of the NF-kβ pathway, and the modulation of inflammatory responses. Additionally, these bacteria have been shown to enhance the efficacy of chemotherapeutic agents and to contribute to the prevention of AOM/DSS-induced tumorigenesis by regulating DNA damage, apoptosis, and cell proliferation, further supporting their potential role in colorectal cancer management. Postbiotics include inanimate microorganisms, cell wall components, cell surface proteins or microbial metabolites, such as vitamins, enzymes, amino acids and lipids, in particular SCFAs (Kvakova et al., 2022). Restoration of butyrate levels is currently being explored as a potential strategy for the prevention and treatment of CRC. Both *in vitro* and *in vivo* animal studies have demonstrated the antitumour potential of butyrate. Its effects are mediated through multiple mechanisms, including immunomodulatory activity - such as inhibition of M2-like macrophage polarization, reduction of tumour PD-L1 expression, and enhancement of effector T-cell responses - as well as direct actions on cancer cells, including inhibition of proliferation and induction of apoptosis (Han et al., 2025; Qin et al., 2025). Despite these promising preclinical findings, clinical evidence remains limited and inconsistent. Only a few clinical trials have investigated butyrate supplementation in CRC, and their results have been heterogeneous, partly due to the lack of standardization in terms of timing, dosage and SCFA source (Sun et al., 2024).

1.4. Biochar and activated carbons

Biochar is a carbon-rich material produced through slow pyrolysis, also known as carbonisation, a thermochemical process that converts biomass. Biomass, a renewable organic material derived from plant and animal sources, is subjected to high temperatures (around 400 °C) in the absence of oxygen, resulting in the formation of biochar (Panwar et al., 2019). The process removes volatile, non-carbon species such as nitrogen, oxygen, and hydrogen, intensifying the carbon content. Biochar is used for soil improvement, waste management and climate change mitigation as well as an eco-friendly renewable source of energy. The property that makes biochar particularly versatile is its highly porous structure, which confers a remarkable adsorption capacity, the property of a compound to link molecules at its surface. To further enhance this adsorption potential, biochar can undergo chemical or physical activation processes, originating activated carbon (AC) with a well-developed porous structure, large specific surface area and exceptional chemical stability (Jha et al., 2021). Activated carbon and other porous carbon materials can exhibit surface areas up to fifty times greater than their original precursors, making them highly attractive for a wide range of applications, including contaminated air purification, water treatment, biomedicine and several other commercial appliances (Nanda et al., 2016). The adsorptive capacity of ACs is also influenced by the heterogeneous chemical composition of their surface, which is typically characterised by the presence of functional groups, such as oxygen, nitrogen, halogen and other elements linked to the carbon layers' edges. These surface heteroatoms also affect the hydrophilicity and hydrophobicity of the ACs. The biochar adsorption capacity can be further enhanced through surface modifications via multiple treatments, such as the introduction of functional groups, enabling the material to be tailored for specific

applications, such as energy storage, catalytic reactions and adsorptions (Jha et al., 2021)

1.4.1 Emerging applications of biochar in drug delivery research

There is clear evidence from animal models supporting the beneficial effects of biochar on gut health. Biochar used as a feed additive has been shown to improve digestion, reduce antibiotic use, help maintain gastrointestinal homeostasis in dairy cows and adsorb pathogenic clostridial toxins, including those produced by *Clostridium botulinum* and *Clostridium tetani* (Nair et al., 2023). Furthermore, biochar supplementation in poultry has been reported to selectively reduce the abundance of major zoonotic pathogens associated with lesions and infections, without negatively affecting microbiota diversity or causing significant shifts in microbial community (Prasai et al., 2016).

Currently, biochar and activated carbons also have established pharmaceutical applications. Owing to their chemical and biological stability, as well as their strong adsorption capacity, activated carbons are widely used for the treatment of diarrhoea, gas, and bloating, and for gastrointestinal decontamination. In emergency medicine, activated charcoal is suggested as an antidote in cases of toxin ingestion and drug overdose (Nanda et al., 2016; Ogunwa et al., 2026).

Over the last decade, nanomaterials, definable in this context as nanocarriers, have gained increasing attention in drug delivery applications due to their ability to adsorb and release pharmaceutical compounds in a controlled manner, thereby enhancing therapeutic efficiency and bioavailability. Considering their large surface area, abundant functional groups, eco-friendliness, tailorability and cost-effectiveness, biochar and biochar-derived specialty materials, such as carbon nanosheets, carbon nanotubes, carbon nanofibers,

templated porous carbon and others, have been investigated (Nanda et al., 2016; Zhuo et al., 2023). Oral bioavailability remains a critical challenge for small-molecule drugs, representing about 90% of approved therapeutics. Unfortunately, only a limited number of studies have explored the application of biochar as nanocarrier in the biomedical field. A study conducted by Wang et al. suggested a new delivery system consisting of hydrogel balls incorporating zinc oxide-modified biochar, designed to achieve slow, stable, long-term and light-controlled drug release for glaucoma treatment (F. Wang et al., 2021). Another *in vitro* study demonstrated that paracetamol and ibuprofen can be effectively loaded onto activated carbon, forming a complex able to stabilise and release the drugs with a fast release kinetic (about 10 minutes). Moreover, the same research reported very low toxicity of activated carbon at concentrations of 10-800 μg/mL in human colon carcinoma cells (Caco-2), supporting its potential as a safe carrier for drug delivery (Miriyala et al., 2017). Additional studies supported the potential use of carbon nanotubes for a pH-controlled delivery and release of anticancer drugs, such as topoisomerase inhibitors, irinotecan, doxorubicin, methotrexate, purine/pyrimidine antagonists and others, exploiting acidic microenvironment of tumour tissues (Panczyk et al., 2016).

The present study demonstrates that biochar derived from alder wood chips is capable of adsorbing and releasing butyrate-glycerides with anti-tumour activity in *in vitro* and other preclinical models of CRC (Fei, Propato et al., 2025).

2. Aim of the thesis

Colorectal cancer (CRC) is an increasing global health concern, particularly considering the rising incidence of early-onset CRC, which shows a growing mortality rate in young adults. Given the well-established role of intestinal microbiota dysbiosis in CRC onset and progression, strategies aimed at restoring short-chain fatty acid (SCFA)-producing bacteria and butyrate levels have emerged as promising approaches for both prevention and therapy. However, clinical studies investigating butyrate supplementation in CRC remain limited and have yielded heterogeneous results, partly due to the lack of standardization in terms of formulation, dosage, and administration timing of SCFAs.

Within this context, the present thesis is part of a broader research project aimed at evaluating an innovative, bio-based delivery system for butyrate. In particular, this study focused on the use of tailor-made biochar derived from alder wood, compared to a commercially available activated carbon (Norit-B), as carriers for butyrate in the form of a complex of mono- and di-glycerides (BMDG), a formulation already employed in animal feed to enhance butyrate availability to the lower intestinal tract and promote eubiosis. Furthermore, evidence from animal models supports the beneficial effects of biochar itself on gastrointestinal homeostasis, further highlighting the rationale for investigating its potential as a functional carrier for colon-targeted delivery strategy.

The first objective of the study was to characterise and compare the chemical, physical, and adsorption/release properties of the two carbon-based materials, and to determine how these differences influence the bioavailability of BMDG and contribute to its biological activity. For this purpose, these effects were assessed in a healthy colon epithelial cell line (HCEC-1CT) for safety evaluation and in a panel of *in vitro* colorectal

cancer models - HCT116 and HT29 cell lines and AKPS organoids - characterised by distinct genetic backgrounds, metabolic phenotypes, and increasing levels of complexity and *in vivo* mimicry.

Considering the critical role of the tumour microenvironment (TME) in cancer initiation, progression, and therapeutic response, and the growing interest in targeting tumour-microenvironment bidirectional crosstalk, the second objective of the thesis was to explore the impact of CRC on the transcriptome of the surrounding adipose tissue and its potential modulation following *in vivo* administration of BMDG compounds. Specifically, this study aimed to evaluate the transcriptional changes occurring in tumour tissue, adjacent non-tumoral mucosa, and peritumoral adipose tissue derived from AOM/DSS-induced murine model of colorectal carcinogenesis - thus recapitulating a carcinogen and inflammation-driven aetiology of the disease - and to assess the effects of free BMDG and BMDG-carbons on these compartments in both preventive and therapeutic settings. Particular attention was given to the adipose microenvironment, hypothesising that modulation of tumour-adipose tissue crosstalk may impair its tumour-supporting functions.

Ultimately, this work aimed to determine whether this tailor-made biochar can represent an effective carrier for the delivery of a novel butyrate formulation, with potential application as a preventive strategy or therapeutic adjuvant, targeting CRC and its adipose microenvironment, and to elucidate the molecular and metabolic mechanisms underlying the potential anti-tumour activity of the combined molecule across multiple experimental models of CRC.

3. Material and Methods

3.1 BMDG compounds production and characterisation

3.1.1 BMDG, Biochar and AC production

BMDG: The liquid used for the Biochar absorption tests, Butyrate of Mono- and Diacyl-Glycerols (BMDG), was provided by SILO spa (S. Bartolo a Cintoia, Florence, Italy), now produced by Glyco srl (Campomorone Genova, Italy). The production process is based on an esterification reaction of glycerol and butyric acid and, at the end of the process, it is obtained a mixture formed by free glycerol (25% approx.), monoglycerides of butyric acid (50% approx.), diglycerides of butyric acid (22% approx.) and in small part by triglycerides of butyric acid (2% approx.).

Biochar was produced from alder wood chips in a continuous oxidative biomass carbonization pilot reactor based on fixed bed, open top, downdraft design, operating in autothermal pyrolysis in the temperature range of 450–700°C and equivalence ratio (ER) in the range 0.1-0.3 (Casini et al., 2021; A. M. Rizzo et al., 2019). The carbonization process has been carried out at a temperature of about 550°C with a residence time of approx. 3 hours in the reactor.

Norit-B is a pharmaceutical grade powdered heated-activated carbon fully compliant with the European Pharmacopoeia (Charcoal, Activated) produced by steam activation and shows an extremely well-developed micro and mesoporosity. It is commercially available and was provided by COMELT spa (Milan, Italy).

3.1.2 pH measurements

The pH was measured according to EN ISO 10390 through an 827 pHmeter (Metrohm, Herisau, Switzerland) after mixing for 60 minutes using a mechanical shaker in 0.1 M of $CaCl_2$ (1:5 v/v).

3.1.3 Porosity characterisation of Biochar and Norit-B

Both Biochar and activated carbon porosity were investigated according to the Brunauer-Emmett-Teller method (BET), and mercury porosimetry. The BET specific surface area was measured by N_2 adsorption isotherms, in a NOVA 2200E (Quantachrome, Boynton Beach, Florida, USA) instrument after degassing at 200°C for 48 hours and then degassed under vacuum (200°C for 24 hours) and focus mostly in the range of micro and meso pores. Meso and macroporosity, in terms of specific surface area and pore volume, were investigated using a AutoPore V 9600 (Micromeritics, Norcross, Georgia, USA) mercury porosimeter widening the results obtained by BET.

3.1.4 Fourier-transform infrared spectroscopy (FT IR)

FT-IR spectra were recorded from 4000 to 600 cm^{-1}, with a 4 cm^{-1} resolution, using a IRTracer-100 (Shimadzu, Kyoto, Japan) equipped with QATR™ 10 Single-Reflection ATR (Shimadzu, Kyoto, Japan) and a diamond crystal.

3.1.5 Scan Electron Microscopy (SEM)

SEM analysis of Biochar and Norit-B was conducted using a Phenom XL G2 (Thermo Scientific, Waltham, Massachusetts, USA). Measurements were conducted on uncoated samples.

3.1.6 BMDG absorption tests

The following steps describe the methodology employed for the absorption of BMDG solution by the AC Norit-B and alder Biochar. Each product was grinded through a mill and sieved through a 200 µm mesh. The under-sieve fraction was collected, then a specific amount (5 or 10 g) of each Biochar and AC Norit-B were weighted and placed in a metal mortar. BMDG solution was heated through a heating plate equipped with a thermal sensor and maintained in agitation by a magnetic stirrer. The solution was kept between 55° and 60°C to decrease the viscosity and to improve the absorption. The warm BMDG solution was added to Biochar or Norit-B with an eyedropper, limiting heat loss during withdrawal. About 0.5 mL of solution was added at a time, mixing with a pestle and a spatula to promote and homogenise the absorption within the char particles. After each addition, the mortar was weighed to determine the amount of oil absorbed. To determine the saturation point, above which Biochar or Norit-B is no more able to absorb the solution, different criteria were considered: the product must remain in a powder-like consistency, without forming lumps; it must not grease the walls of the container where it was placed and it must feel powdery to the touch. Moreover, when the oil charged sample was placed on a white paper sheet, it should not release oil and therefore should not leave any halo or stain on the sheet. When halos appear, the product was considered over-saturated, so the weight obtained at the previous step was considered the maximum level of saturation of Biochar or Norit-B.

3.1.7 BMDG release tests

BMDG release tests on BMDG loaded Biochar and Norit-B were performed in water. About 1 g of sample was weighted and placed in a 250 mL glass flask, then 200 mL of distilled water were added and the solution was warmed under agitation at 37°C in a

heating plate for different timing (30 minutes-3 hours). The samples were then filtered under vacuum at 2.7 µm by glass fibre filter Whatman GF/D 1823-070, previously weighted. The filters were then put in an oven at 105°C overnight and then weighted (dry filtered solids gross weight.) The recovered filter solids were calculated as follow:

Recovered solids (g) = (dry filtered solids gross weight (g) - filter weight(g))

The initial loaded BMDG was calculated as follow:

Initial BMDG (g) = (Initial loaded Biochar weight dry basis (g) × loaded BMDG % w/w)/100

The released BMDG was calculated as follow:

Released BMDG (g) = Recovered solids (g) - Initial loaded Biochar weight dry basis (g)

BMDG release (%w/w) = Released BMDG (g) / Initial BMDG (g) ×100

The release tests were also performed on an unloaded Biochar, in particular on the AC Norit-B and on alder Biochar, evaluating the test performance as solids recovery as follow:

Solids recovery efficiency (%w/w) *= 100 - (Initial Biochar weight dry basis (g) - Recovered solids (g)) / Initial Biochar weight dry basis (g)) × 100*

3.1.8 Glucose absorption by carbons

Glucose absorption in water.

A 10 g/L glucose solution prepared in 20 mL was added with 2 g of Biochar or with Norit-B under stirring. After 2.5 hours incubation in an orbital oscillator, the solution was

filtered and analysed in a High-performance liquid chromatography (HPLC) Prominence UFLC LC20-AT (Shimadzu, Kyoto, Japan) equipped with a refractive index detector RID 10 A (Shimadzu, Kyoto, Japan), a Hi-Plex H column 300×7.7 mm (Agilent, Santa Clara, CA, USA) and a guard column PL Hi-Plex H 50 × 7.7 mm (Agilent, Santa Clara, CA, USA), operating at 40°C with a flow of 0.6 mL/min (sulfuric acid 0.05M) previously calibrated with glucose in a 5 point calibration. The glucose absorption yield was calculated as follow:

Glucose absorption yield (%w/w) = *(Initial glucose in solution (g) - Final glucose in solution (g)) / Initial Biochar weight dry basis (g)) × 100.*

Glucose absorption in cell medium

Biochar or Norit-B (4.5 mg) were resuspended in 1 mL of culture medium enriched with glucose 4.5 g/l (25 mM). Glucose concentration in the medium was assessed by a 24-hour real time measurement with Live Cell Metabolic Analyzer (PHC Europe, The Netherlands), following the manufacturer's instruction, and expressed as percentage of depletion.

3.2 *In vitro* experiments

3.2.1 Cell treatment: stimuli preparation

The density of BMDG, 1.136 g/mL, was calculated and used to determine a range of doses of free BMDG used in the cell counting experiment, cell viability test, ^{3}H-thymidine incorporation experiment and Seahorse analysis.

The half-maximal inhibitory concentration (IC_{50}) curve was calculated for HCT116 and HT29 cells and the 500 µg/mL dose (mean IC_{50} derived from thymidine incorporation

experiments in HCT116 and HT29 cells at 24 hours) was chosen for the subsequent experiments carried on the cell lines. For the AKPS organoids, a dose of 1000 µg/mL was selected, based on the maximum cytotoxic effect detected by the cell viability assay and the maximum reduction in the area of organoids treated with increasing doses of BMDG.

Consequently, the absorbed carbons (BMDG-Biochar or BMDG-Norit) and the free carbons (Biochar or Norit-B) were weighed with an analytical balance considering the different percentages of absorption of BMDG described previously. Specifically, the BMDG weight content in the absorbed compounds was 67.1% and 61.5% in BMDG-Biochar or BMDG-Norit, respectively. Therefore 0.75 mg/mL BMDG-Biochar, 0.8 mg/mL BMDG-Norit, 0.25 mg/mL Biochar and 0.32 mg/mL Norit-B were weighed depending on the experimental setting including HCT116, HT29 and HCEC-1CT. Regarding organoids, 1.5 mg/mL BMDG-Biochar, 1.6 mg/mL BMDG-Norit, 0.5 mg/mL Biochar and 0.64 mg/mL Norit-B were weighed depending on the experiment design. Free BMDG and all carbons were diluted in cell culture medium (depending on the experiment and cell type).

3.2.2 *In vitro* models

The colorectal carcinoma cell line HCT116 and the colorectal adenocarcinoma cell line HT29 were obtained from the American Type Culture Collection (Manassas, VA, USA). Both cell lines were cultured in McCoy's 5A medium (Sigma-Aldrich, Milan, Italy) supplemented with 10% of Fetal Bovine Serum (FBS), 2mM L- glutamine, 100 U/mL penicillin and 100 µg/mL streptomycin.

AKPS (*Apc* $^{fl/fl}$; *Kras*$^{G12D/+}$; *Trp53*^{KO}; *Smad4*^{KO}) organoids, obtained electroporating Apc$^{fl/fl}$;Kras$^{G12D/+}$ organoids with sgRNAs targeting Trp53 and Smad4 (Fujii et al., 2015),

were a gift from Dr Kevin Myant and his group (MRC Human Genetics Unit MRC Institute of Genetics & Molecular Medicine, The University of Edinburgh). AKPS were plated in droplets of Cultrex Reduced Growth Factor Basement Membrane Extract, type 2 (BME) (Bio-Techne, Minneapolis, United States) and incubated for 15 min at 37°C to allow BME solidification. Organoids were then cultured in growth medium - EN medium - consisting of Advanced DMEM/F-12 (Gibco, ThermoFisher Scientific, Milan, Italy) supplemented with 100 µg/mL Primocin (Invivogen, San Diego, United States), 2mM L-glutamine, 10uM HEPES, B-27 Supplement (50X) (Gibco), N-2 Supplement (100X) (Gibco), Noggin conditioned medium (provided by Dr Kevin Myant) and 50 ng/mL Mouse EGF Recombinant Protein (PeproTech, ThermoFisher Scientific, Milan, Italy).

The human colon epithelial cell line HCEC-1CT was cultured in ColoUp medium consisting in DMEM high glucose Glutamax Supplement/ Medium 199 (4+1) (ThermoFisher Scientific) supplemented with 2% Cosmic Calf Serum (Hyclone, Cytiva, United States), 20ng/mL EGF, 10 µg/mL Insulin, 2 µg/mL Apo-Transferrin, 5 nM Sodium-Selenite and 1 µg/mL Hydrocortisone.

All reagents were purchased from Sigma-Aldrich (Milan, Italy), unless otherwise specified. All cell lines and AKPS organoids were grown at 37°C in a humidified 5% CO_2 atmosphere.

3.2.3 Cell population doubling (PD) evaluation

HCT116 and HT29 cells were seeded in triplicate in a 6-well plate in complete medium. After 7 days, cells were trypsinised with trypsin-EDTA and trypsin-EDTA 2X, respectively, and were counted using haemocytometer. Then, cells were re-plated at the same initial density and under the same conditions to be recounted after the same period

(7 days). The experiment was repeated for 11 weeks. Following the protocol of Baglioni S. et al. (Baglioni et al., 2012), the number of PD was calculated according to the formula:

$PD = log_2 (N_i/N_0)$ (N_i = number of cells obtained, N_0 = the number of cells plated). Results were plotted according to the following equation: $PD_{(n)} = PD_{(n-1)} + PD_{(n)}$ (n= PD at a certain time point, n-1= PD at the previous time point).

3.2.4 Cell cycle Analysis

HCT116 and HT29 cells were seeded in 12-well plates at a density of 10^5 cells/well. Once 70-80 % of confluence was reached, cells were trypsinised and analysed with a Muse™ automated cell analyser (Merck Millipore, Billerica, MA, USA) using the Muse™ Cell Cycle kit (#MCH1001006, Merck Millipore), according to the manufacturer's instructions. Briefly, 10^6 HT29 and 1.5 x 10^6 HCT116 were washed once with Dulbecco's Phosphate Buffered Saline (DPBS), then resuspended in DPBS and added drop by drop to a tube containing 70% ice cold methanol, stirring with a vortex mixer at 15 Hz. The cells were left to fix for 3 hours at a -20°C and, after centrifugation and washing with DPBS, were incubated for 30 minutes at room temperature (RT) in the dark with Muse™ reagent and then readings were taken on the previously set up instrument.

3.2.5 Cell cytotoxicity by cell count

Cell cytotoxicity effects of the different treatments (BMDG alone, BMDG-Biochar, BMDG-Norit, as well as free carbons Biochar and Norit-B) were evaluated by direct viable cell counts. HCT116 and HT29 were seeded in 12-well plates (7500 cells/well) and treated with BMDG in a dose range from 5 to 40000 µg/mL for 24, 48 and 72 hours to calculate the relative IC_{50}. In another set of experiments, cells were treated for the same time intervals directly with BMDG-Biochar and BMDG-Norit or with 24 hour-

conditioned media depleted by carbons. After treatments, cells were trypsinised and counted in the haemocytometer. Mean cell number was obtained by counting triplicates in four different experiments.

3.2.6 Thymidine incorporation

The CRC cell lines, HCT116 and HT29, as well as HCEC-1CT cells, used as non-tumoral controls, were seeded in 12-well plates at a density of 2 x 10^5 cells/well in McCoy's 5A complete medium and of 5 x 10^4 cells/well in ColoUp medium, respectively. After reaching ideal confluence, HCT116 and HT29 cells were starved for 4 hours with their respective serum-free media and then treated with BMDG at different doses (50-100-250-500-1000-5000 µg/ml) or with free BMDG, BMDG absorbed on chars and free chars (as described in "Cell treatment: stimuli preparation" section), depending on the experimental setting. Thymidine incorporation assay in HCEC-1CT was performed exclusively with 500 µg/mL of free BMDG, BMDG-Biochar and BMDG-Norit.

AKPS were plated in three 15 µl droplets/well of 12-well plates in EN medium. After 48 hours, organoids were treated with 1000 µg/mL of free BMDG, BMDG-Biochar and BMDG-Norit (as described in "Cell treatment: stimuli preparation" section).

For each *in vitro* model, cells were treated for 24 hours, followed by a 4-hour pulse with 0,5 µCi/well of ^{3}H-thymidine (Cantini et al., 2019). Then cells were washed twice with cold DPBS and the proliferation was stopped with ice-cold 10% trichloroacetic acid (TCA) for 30 minutes at 4°C. After washing in 5% TCA, cells were solubilised in 0.25 N NaOH for 15 minutes at 37°C and DNA synthesis was evaluated according to the amount of ^{3}H-thymidine incorporated into TCA-precipitated materials, measuring the

radioactivity in the scintillation counter. Experiments were performed in triplicate and were repeated at least three times.

3.2.7 Resazurin-based viability assay

HCEC-1CT cells, as well as AKPS organoids were seeded in 12-well plates at a density of 5 x 10^4 cells/well in ColoUp medium and of three 15 µl droplets/well in EN medium, respectively. After 24 (HCEC-1CT) and 48 (AKPS) hours, both *in vitro* models were treated with 500 and 1000 µg/mL of free BMDG, BMDG-Biochar and BMDG-Norit, respectively. In another experimental setting, AKPS were treated with increasing doses of BMDG (100-250-500-1000-5000 µg/ml). Cells and organoids were treated for 24 hours, followed by washes with DPBS and by a 4-hour pulse with 10% of culture volume of Resazurin (R&D systems) add in their respective complete media. Absorbance was read using Victor Nivo multimode plate reader (Revvity) set at 570 nm and 600 nm, measuring the maximum absorbance for reduced and oxidized dye.To evaluate the cytotoxic effects of the BMDG compounds, percentage difference between treated and untreated control cells/organoids was calculated in accordance with Bio-rad's protocol "Measuring Cytotoxicity or Proliferation Using alamarBlue". The formula is:

$$[(O2 \times A1) - (O1 \times A2) / (O2 \times P1) - (O1 \times P2)] \times 100$$

O1 = molar extinction coefficient (E) of oxidized Resazurin (blue) at 570 nm = 80586

O2 = E of oxidized Resazurin at 600 nm = 117216

A1 = absorbance of treated wells at 570 nm

A2 = absorbance of treated wells at 600 nm

P1 = absorbance of untreated control well at 570 nm

P2 = absorbance of untreated control well at 600 nm

3.2.8 Measurement of organoids area

AKPS organoids were seeded in 12-well plates at a density of three 15 µl droplets/well in EN medium and, after 48 hours, were treated with increasing doses of BMDG (100-250-500-1000-5000 µg/ml) or with 1000 µg/mL of free BMDG, BMDG-Biochar and BMDG-Norit, depending on the experimental setting. Experiments were conducted in triplicate, with at least three images per well captured. Area measurements were obtained using Fiji (ImageJ 1.54p).

3.2.9 Transmission Electron Microscopy (TEM)

TEM analysis was performed essentially as reported by Martinelli S. et al. (Martinelli et al., 2024) on both HCT116 and HT29 cells and AKPS organoids. Cells treated with the different stimuli for 24 hours, were washed with DPBS and directly fixed in Karnovsky fixative overnight at 4°C. AKPS, after 24 hours of treatment with BMDG compounds, were collected and gently resuspended in cold DPBS using a P1000 pipette to disrupt BME domes. The suspension was centrifuged at 300g for 5 minutes, and the pellet was fixed in fixation buffer - consisting of 2% paraformaldehyde (EM grade) and 0.2% glutaraldehyde in 0.1 M Sorensen's buffer - for 2 hours in a cold room. Following fixation, samples were centrifuged again at 300g, and the pellet was left in fixation buffer overnight. All samples were then post fixed in 1% osmium tetroxide in 0.1 M phosphate buffer (pH 7.4) for 1 hour at room temperature. Once dehydrated in graded acetone and passed through propylene oxide, samples were embedded in epoxy resin. Semithin sections were stained in aqueous 0.1% toluidine blue and analysed under optical microscopy, while serial ultrathin ones were processed with gadolinium acetate and alkaline bismuth subnitrate and examined under a JEM 1010 electron microscope (Jeol,

Tokyo, Japan) at 80 kV. Photomicrographs were taken with a MegaView III (Soft Imaging System, Muenster, Germany) digital camera connected with a dedicated software (AnalySIS, Soft Imaging Software, Muenster, Germany).

3.2.10 Seahorse analysis: adenosine triphosphate (ATP) production and mitochondrial respiration

Real-time ATP rate assay

Metabolic status was investigated on a Seahorse XF96 Analyzer (Agilent Technologies, Santa Clara, CA, USA). Real-time ATP rate assay was performed through the Seahorse XF Real-Time ATP Rate Assay kit (Agilent Technologies, #103592), according to the manufacturer's instructions.

Briefly, 1 x 10^4 HCT116 and HT29 cells and 2.5 x 10^3 HCEC-1CT were plated in the Agilent Seahorse XF Cell Culture Microplate (96 wells) in McCoy's 5A complete medium and ColoUp medium, respectively, and let to grow for 24 hours. AKPS were plated by adapting Ludikhuize et al. protocol (Ludikhuize et al., 2021). In summary, organoids were expanded in standard 12-well culture plates and after 72 hours, four 15 µl drops were collected and organoids were re-plated in 50 µl of BME in Seahorse cell culture microplates which had been pre-warmed in the incubator. After BME solidification, 60 ul of EN medium were added.

The day before the assay, the sensor cartridge was hydrated in Seahorse XF Calibrant at 37°C in a non-CO_2 incubator overnight. The day of the assay, after 24 hours in growth medium or with 500 µg/mL (cell lines)/1000 µg/mL (AKPS) of free BMDG and BMDG absorbed on Biochar/Norit-B, the assay medium was prepared by supplementing the Seahorse XF DMEM medium pH 7.4 (Agilent Technologies, Santa Clara, CA, USA) with 1 mM pyruvate, 2 mM glutamine, and 10 mM glucose. The medium was removed from

the Seahorse microplate, and cells were washed with warmed assay medium using a multichannel pipette and were incubated with assay medium at 37 °C in a non-CO_2 incubator for 60 minutes prior to the assay. Then the assay medium was removed again and replaced with 180 µl of fresh medium. In the meanwhile, Oligomycin (150 µM) and Rotenone/Antimycin A (Rot/AA, 50 µM) were resuspended with 420 µL and 540 µL of assay medium, respectively. Then the Oligomycin and Rot/AA were diluted to reach the concentration of 15 and 5 µM (10X), respectively. The hydrated sensor cartridge was loaded with Oligomycin 1.5 µM and Rot/AA 0.5 µM into ports A and B, respectively. The starting well volume was 180 µl, so to obtain the final concentration (10X) the injection volumes were 20 µl in port A and consequently 22 µl in port B. Then the loaded sensor cartridge with the calibrant plate was placed into the Seahorse XFe Analyzer, and after the calibration, the XF Real-Time ATP Rate Assay was performed according to the manufacturer's default protocol for cell lines. Regarding AKPS, due to their three-dimensional structures, it was necessary to adjust the measurement protocol. Specifically, 3, 6, and 5 cycles, each consisting of 3 minutes of mixing and 4 minutes of measurement, were identified as optimal for measuring parameters at baseline, after oligomycin A and after Rot/AA injection, respectively. The Seahorse Report Generator automatically calculates the test parameters from Wave data, in particular the oxygen consumption rate (OCR) and the extracellular acidification rate (ECAR). For AKPS analysis, only wells containing well-formed organoids positioned in the centre were selected and data were normalised on protein content (Bradford assay). Data were analysed with Wave software (version 2.4.0, Seahorse Bioscience, Agilent Technologies, Santa Clara, CA, USA).

Mito Stress assay

A Mito Stress Test Kit (Agilent Technologies, #103015) was used to assess the mitochondrial function by directly measuring OCR and ECAR of HCT116, HT29 and HCEC-1CT cells and AKPS organoids plated and treated in the Agilent Seahorse XF Cell Culture Microplate as described above. After 24 hours of treatment with 500 µg/mL or 1000 µg/mL of free BMDG and BMDG absorbed on Biochar/Norit-B, the medium was removed from the Seahorse microplate, and cells were washed with assay medium - supplemented with 1 mM pyruvate, 2 mM glutamine, and 10 mM glucose - using a multichannel pipette and were incubated with the assay medium at 37 °C in a non-CO_2 incubator for 60 minutes to allow for temperature and pH equilibration before being loaded into the XF96 Analyzer. In the meanwhile, Oligomycin (150 µM), carbonyl cyanide m-chlorophenylhydrazone (FCCP, 100 µM) and Rot/AA (50 µM) were resuspended with 630 µL, 720 µL and 540 µL of assay medium, respectively. Then Oligomycin, FCCP and Rot/AA were diluted to reach the concentration of 15 µM, 10 µM and 5 µM, respectively. The injection sequence in was programmed as follows: 1st (port A), oligomycin (1.5 µM final concentration); 2nd (port B), FCCP (1 µM final concentration); 3rd (port C), Rot/AA (0.5 µM final concentrations, respectively). Regarding AKPS the measurement protocol consisted in 3, 6, 4 and 5 cycles, each consisting of 3 minutes of mixing and 4 minutes of measurement, for parameters measurement at baseline, after oligomycin A, after FCCP and after Rot/AA injection, respectively. For AKPS analysis, only wells containing well-formed organoids positioned in the centre were selected and data were normalised on protein content (Bradford assay). Data were analysed with Wave software (version 2.4.0, Seahorse Bioscience, Agilent Technologies, Santa Clara, CA, USA).

Energy map

The ability of Seahorse technology to simultaneously measure OCR and ECAR allowed to investigate the cell energy profile. In particular, both the real-time ATP assay and the Mito Stress test evaluate cell energy phenotypes; phenotypes can be defined as aerobic (the cell predominantly uses mitochondrial respiration), glycolytic (the cell predominantly uses glycolysis), quiescent (the cell is not very energetic), energetic (the cell uses both aerobic and glycolytic pathways to a similar extent).

3.2.11 Statistical Analysis

Statistical analysis was performed using SPSS software 27.0 (Statistical Package for the Social Sciences, Chicago, US) for Windows. The Kolmogorov–Smirnov's test was used to assess normal distribution of data. Results are expressed as mean ± SE, unless otherwise stated. All experiments have been performed at least as triplicates, unless otherwise stated. Student's t test was used for comparison of two classes of data and two-ways ANOVA followed by Bonferroni's *post hoc* test for comparison of multiple classes of data. A p-value < 0.05 was considered as statistically significant. Sigmoidal curves and inhibitory concentration (IC) for dose response to the different compounds were analysed by Origin 4.0 software.

3.3 mRNA sequencing and gene expression analysis

3.3.1 *In vivo* treatment of animal model and tissues collection

C57BL/6 mice were purchased, treated and tissues were collected by Professor Andrea Galli's group (University of Florence). Briefly, promotion of chronic inflammation and

formation of colorectal tumours was carried out by treatment with a single dose of AOM (10 mg/kg) followed by three treatments with 2.5% DSS (De Robertis et al., 2011). Mice subjected to AOM/DSS treatment only (n=12), were used as reference group for two experimental arms representing two treatment models with BMDG compounds. The preventive model (where mice were treated one week before AOM administration and throughout the entire experimental phase lasted 80 days) included 11, 10 and 11 mice treated with BMDG, BMDG-Biochar and BMDG-Norit, respectively. The therapeutic model (where mice were treated starting one week after tumour formation) comprised 12, 11 and 11 mice treated with BMDG, BMDG-Biochar and BMDG-Norit, respectively. The dose was selected considering free butyrate as the bioactive molecule present in BMDG and in accordance with the butyrate dose reported in the literature (1 g/kg) (Y. Du et al., 2020). 80 days after treatment with AOM, all the experimental arms, including the reference group, were sacrificed by cervical dislocation and intestinal non-tumoral mucosa, tumour tissues, abdominal adipose tissues, peritumoral adipose tissues and other organs were collected, snap frozen and stored at -80°C.

3.3.2 RNA extraction

RNA was extracted from non-tumoral mucosa, tumour, peritumoral adipose tissue and abdominal adipose tissue (located distally from the tumour) samples, all collected from the same individual mouse to ensure matched analyses across tissue types. For each treatment group within each experimental model, a minimum of three biological replicates (mice) was included.

For mechanical tissue disruption, 5 mm stainless steel beads (Qiagen, Milan, Italy) were pre-cooled in 2 mL tubes. Adipose tissues were sectioned, weighed to ensure an optimal

mass of < 100 mg, and placed into the pre-cooled tubes containing beads on dry ice. RNA extraction from adipose tissue was performed using QIAzol Lysis Reagent according to the manufacturer's instructions, adding 1 mL of QIAzol per 100 mg of tissue.

Non-tumoral mucosa and tumour tissues were processed following the "RNeasy Mini Kit" (Qiagen) protocol. Briefly, samples were homogenized in 600 µL of Buffer RLT supplemented with 10 µL/mL β-mercaptoethanol in pre-cooled tubes containing beads. Both adipose and intestinal tissues, in QIAzol Lysis Reagent and Buffer RLT respectively, were homogenised using a TissueLyser III Bead Mill Homogenizer (Qiagen). Adipose tissues were homogenised with two 1-minute cycles at 30 Hz, whereas intestinal tissues underwent two 1.5-minute cycles followed by two 1-minute cycles at 30 Hz.

Adipose tissue homogenates were centrifuged at 12,000 g for 10 minutes at 4°C, and the supernatants were collected. Total RNA was extracted using the chloroform/isopropanol method included in the "QIAzol Lysis Reagent" protocol. Briefly, chloroform was added at a volume of 200 µl per mL of QIAzol used. After centrifugation to separate the aqueous phase containing RNA, isopropanol (500 µl per mL of QIAzol used) was added, followed by an additional centrifugation step to precipitate RNA. The supernatant was discarded and the RNA pellet was washed with 75% ethanol (1:1 with the volume of QIAzol used) and centrifuged again. RNA pellet was resuspended in 50 µl of RNAse-free water.
RNA from intestinal tissue homogenates was instead isolated using RNeasy Mini spin column, according the manufacturer's instructions, and eluted in 30 µl of RNAse-free water.

RNA concentration was determined by measuring absorbance at 260 nm using a spectrophotometer (Nanodrop, Thermo Fisher Scientific). RNA purity was evaluated based on the 260 nm/ 280 nm and 260 nm/ 230 nm absorbance ratios.

3.3.3 mRNA-seq and data analysis

mRNA-seq libraries were prepared and sequenced by the Genomic Unit at Cogentech Srl (IFOM, Milan, Italy). Briefly, RNA quality was assessed using Agilent RNA ScreenTape. Poly(A)-captured mRNA libraries were prepared, and library quality was checked using Agilent D1000 ScreenTape. 60M paired-end sequencing was performed using Illumina NovaSeq 6000 DX platform.

RNA-seq data were analysed by the Genomic Unit service using nf-core/rnaseq bioinformatics pipeline (Ewels et al., 2020), with gene annotation based on Ensembl release 115 (Mus_musculus.GRCm39). Raw counts were normalized using upper-quartile normalization scaled to 1000 for quality controls check and distance matrix generation.

3.3.4 Differential gene expression analysis

Raw counts and metadata (where sample ID were linked to tissue type, treatment condition and treatment model) were used for differential gene expression analysis performed with DESeq2 package (Love et al., 2014) using R (version 4.5.2) within the Rstudio Integrated Development Environment (version 2025.9.1.401, Posit team, 2025). Genes with low expression were filtered out by retaining only those with a count ≥ 10 in at least three samples. Differential expressed genes were filtered based on statistical significance (adjusted $p < 0.05$) and fold change (absolute log2 Fold Change > 2 or 0.5 depending on the groups comparison). Principal Component Analysis (PCA) of RNA-seq

sample was obtained by applying variance stabilizing transformation (vst) to raw counts using the DESeq2 package. Volcano plots were generated using the *ggplot2* package, with the x-axis representing $\log_2$ fold change and the y-axis showing $-\log_{10}$ of the adjusted *p*-value.

Gene Set Enrichment Analysis (GSEA) was performed in R within Rstudio Integrated Development Environment, using the Reactome pathway database on a ranked gene list, ordered in decreasing $\log_2$ fold change values derived from differential gene expression analysis (Korotkevich et al., 2019). The top 20 significantly enriched pathways (adjusted $p < 0.001$) were considered.

4. Results

4.1 Chemical and physical properties of Biochar and activate carbon Norit-B

BMDG was produced with the following ratio: 50.3% monoacyl butyrate, 21.9% diacyl butyrate, 2.3% triacyl butyrate (tributyrin), 25.3% free glycerol and absorbed on Biochar obtained from alder wood (BMDG-Biochar) or on commercially available activated carbon Norit-B (BMDG-Norit). Chemical and physical characteristics of the two types of carbons were evaluated and reported in Table 2.

Biochar/AC	Particle size (µm)	pH	BET (m^2/g)	Pore Volume [DFT] (cm^3/g)	Pore Volume [Hg Poros.] (ml/g)	Avg.pore diameter [Hg Poros.] (µm)	Porosity [Hg Poros.] (%)
Biochar	≤200	8.34	248	0.118	3.029	0.913	81.58
Norit-B	≤200	6.90	1264	0.619	1.667	0.047	70.85

Table 2. Comparison of the main chemical and physical characteristics of Biochar and Norit-B. The Biochar and activated carbon (Norit-B) porosity was obtained through the Brunauer–Emmett–Teller method (BET) and mercury porosimetry [Hg poros.]. The specific surface area was determined by BET (m2/g) while the average pore volume was estimated using the DFT (Density Functional Theory) approach on BET data (cm3/g) and directly measured by mercury porosimetry (ml/g). The average pore diameter (µm) and porosity (%) derived also from mercury porosimetry. The pH from both samples were also measured after 1:5 (v/v) extraction in CaCl2.

Both powders consisted of particles with diameters ≤ 200 nm, but structurally different especially in terms of porosity, being Biochar characterised mainly by meso-/macro-porosity while Norit-B resulted as significantly micro-porous. The different three-dimensional structure of Biochar and Norit-B can be appreciated by SEM analysis (Figure 6A, B, respectively). Biochar particles clearly showed how the morphological structure

of the woody feedstock was maintained in the carbonised product (Fig.6A) while Norit-B presented a more amorphous structure with no evidence of meso- and macro- porosity (Figure 6B), conversely appreciable in the Biochar particles. A preliminary screening of the presence of functional surface groups conducted by Fourier-transform infrared spectroscopy (FT IR) revealed no signals in the FT IR spectrum and consequently no presence of specific functional groups (Figure 6D); also Biochar spectrum (Figure 6C) could be considered almost clear with very few signals in the aromatic region 1600-1350 cm^{-1} (Breton et al., 2021; Elnour et al., 2019; Mujtaba et al., 2021) and no particular evidence of surface functional groups.

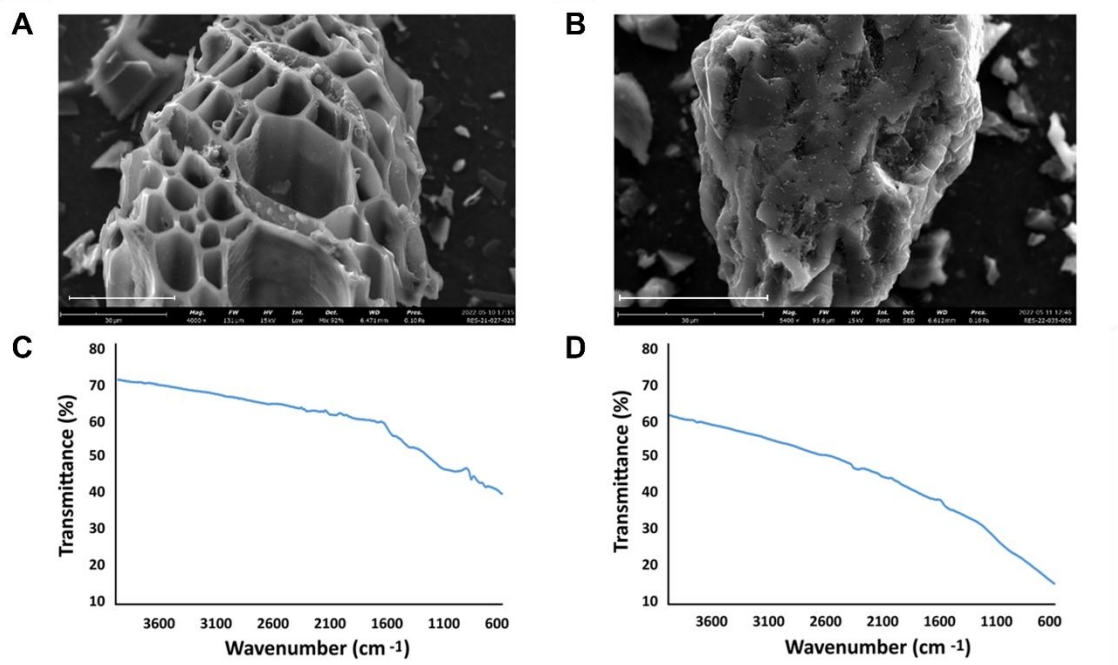

Figure 6. Properties of BMDG-absorbed and unabsorbed carbons. (A-B) Representative Scan Electron Microscopy (SEM) images of Biochar and Norit-B particles showing the differences in the porosity; scale bars are indicated at the left bottom (30 μm). (C-D) Representative Fourier-transform infrared (FT-IR) spectra are shown for Biochar and Norit-B, which enable investigation of the presence of functional groups: data are expressed as % of Transmittance.

To evaluate if the different structural characteristics of the pores of the two types of carbons may affect their efficiency in acting as molecular carriers for BMDG, BMDG loading and release properties of Biochar and Norit-B were evaluated under the same conditions. The two samples presented a pH of 8.3 and 6.9 for Biochar and Norit-B, respectively. Table 3 shows the superiority of Biochar in the combined uptake and release of BMDG compared to Norit-B, resulting in a 100% of Butyrate release in water.

Carrier	Particle size (µm)	Carrier amount (%w/w)	BMDG amount (%w/w)	BMDG specific sorption ($g_{BMDG}/g_{CARRIER}$)	BMDG release (%w/w)	BMDG release ($g_{BMDG}/g_{CARRIER}$)
Biochar	≤200	32.9	67.1	2.04	100	2.03
Norit-B	≤200	38.5	61.5	1.60	81	1.30

Table 3. Comparison of BMDG absorption and release properties of Biochar and Norit-B. BMDG was absorbed on both Biochar or Norit-B (gBMDG/gcarrier) and the proportion of solid carrier and BMDG in each absorption experiment are expressed as weight percentages (w/w%). The BMDG release from the BMDG-Biochar and BMDG-Norit is expressed both as weight percentage (w/w%) and as (gBMDG/gcarrier).

Conversely, Biochar was not able to capture glucose compared to the ability of Norit-B to absorb the glucose dissolved in water or present in the medium used for cell culture (Table 4).

Carrier	Biochar (g/l)	Media	Glucose input (g/l)	T0 Glucose absorbtion (%)	T24 Glucose absorbtion (%)
Norit-B §	100	water	9,9	70,2	-
Biochar §	100	water	9,9	BDL	-
Norit-B #	45	Cell medium	4,5	52	48
Biochar #	45	Cell medium	4,5	1	0

Table 4. Glucose absorption test. Glucose absorption ability of Biochar or active carbon (Norit-B) has been

evaluated in different conditions through two different methods (see Method section), maintaining the same CHAR:Glucose (10:1) ratio for both Biochar and Norit-B. §HPLC analysis, # real-time measurement by Live Cell Metabolic Analyzer. BDL: below detection limit; T0=immediately after char addition, T24= after 24 hours of incubation.

4.2 Biological properties of the BMDG, alone or absorbed on Biochar or Norit-B and their effects on *in vitro* cell models of CRC

Biological properties of free BMDG or absorbed on the two char vehicles, BMDG-Biochar or BMDG-Norit, were assessed *in vitro* on two human cell line models of CRC, namely HT29 and HCT116, and on AKPS, APC-deficient mouse organoids of colon cancer.

HT29 and HCT116 derived from a more differentiated colorectal adenocarcinoma and from a less differentiated carcinoma, respectively (Ahmed et al., 2013). HCT116 cells displayed a higher *in vitro* proliferation rate compared to HT29 cells (Figure 7A) associated with a higher fraction of cells in G2/M and G0/G1 phases (Figure 7B). The more aggressive behaviour of HCT116 cells was further supported by the analysis of cell metabolism performed in both cell lines by Seahorse technology. The analysis of the relative ratio of ATP production (Figure 7C) revealed that HCT116 are characterised by a significantly higher glycolytic and lower mitochondrial ATP production compared to HT29 cells. This metabolic condition characterised by a glycolytic shift defined as the Warburg effect, is typical of aggressive and highly proliferative cancer cells. The simultaneous measurement of indicators of the two energy producing pathways (OCR and ECAR, mainly referred to mitochondrial respiration and to glycolysis, respectively),

stressed the differences in the energetic profile of the two cell lines, further supporting a more aggressive metabolic phenotype of HCT116 cells (Figure 7D).

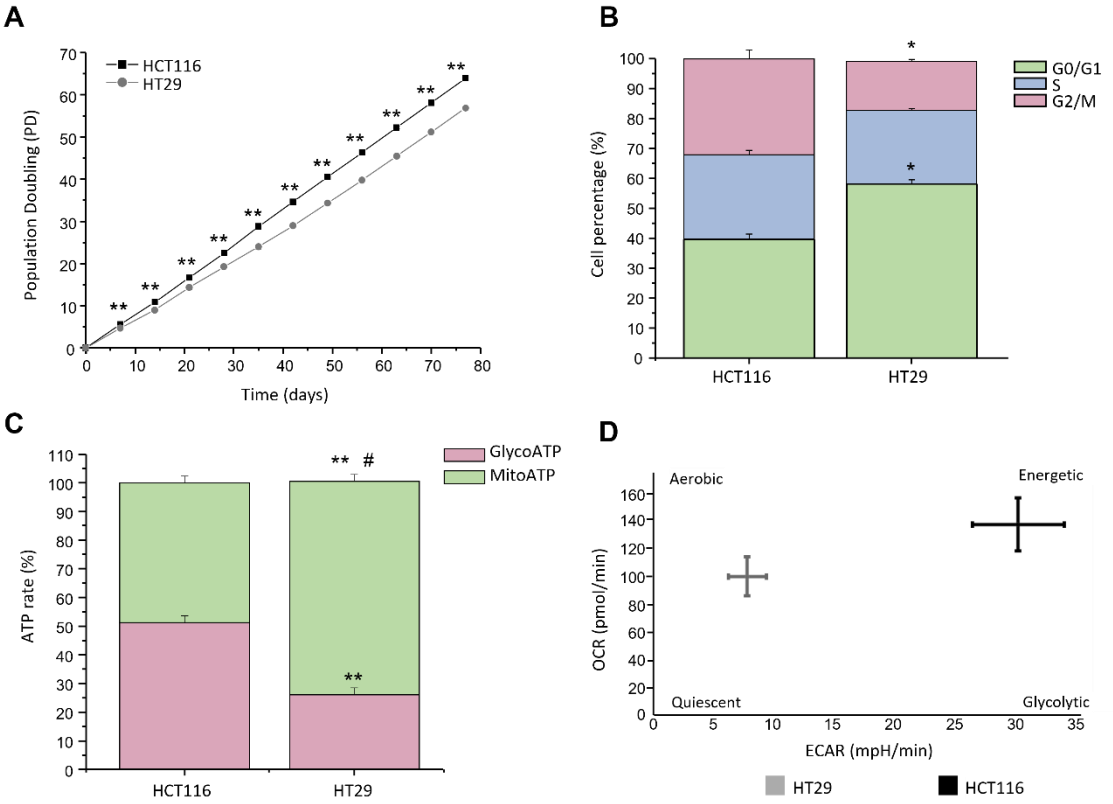

Figure 7. HCT116 cells display a phenotype more aggressive than HT29: CRC cell line properties compared. (A) Population doubling (PD) curves were obtained by cell counting at different passages of HCT116 and HT29 cultures expanded for 11 weeks. Results are expressed as mean ± SE PD numbers obtained by cell counting in triplicate; statistical analysis was performed with Student's t-test $^{**}p<0.001$ HCT116 vs HT29. (B) Data obtained from cell cycle analysis are shown as mean ± SE of the percentage of HCT116 and HT29 cells grown in triplicate for 24 hours in their complete growth medium; statistical analysis was performed with Student's t-test $^{*}p<0.05$ HCT116 vs. HT29. (C) Analysis of basal ATP production rate (%) performed through Seahorse XF Real-Time ATP rate assay is represented as the sum of ATP production associated with mitochondrial oxidative phosphorylation (mitoATP) during OXPHOS process and that associated with glucose to lactate conversion (glycoATP) during the glycolytic process. Results are expressed as the mean ± SE of n=3 independent experiments obtained by culturing HCT116 and HT29 cells for 24 hours in their complete growth medium; statistical analysis was performed with Student's t-test $^{**}p$ <0.001 HCT116 vs. HT29; $^{\#}p$ <0.001 glicoATP vs. mitoATP. (D) Energy map of HCT116 and HT29 cells showing the relative metabolic profiles based on oxygen consumption rate (OCR, pmol/min) and extracellular acidification rate (ECAR, mpH/min).

To assess the direct effect of BMDG on CRC cells *in vitro*, the two cell lines were treated with increasing concentrations of the mixed compound for 24, 48 and 72 hours. The treatment resulted in a dose-response and time-dependent reduction in the cell number, displaying a lower IC_{50} for HCT116 (IC_{50} = 1413 µg/ml at 24 hours) compared to HT29 (IC_{50} = 2319 µg/ml at 24 hours) cells (Figure 8A). The effects of BMDG when absorbed on chars on cell viability was then assessed in the aggressive HCT116 line, as this seemed to be the most sensitive between the two cell lines. HCT116 cells were treated for 24, 48 and 72 hours with the direct addition of BMDG-Biochar and BMDG-Norit or with the respective conditioned medium (see Methods) by incubation with absorbed chars and after depletion of the carbon particles (Figure 8B). BMDG-Biochar and BMDG-Norit direct addition significantly reduced the cell number already starting from 24 hours, with an increasing effect at longer incubation times. The reduction in the cell number obtained by time course incubation with char-depleted conditioned media, not containing carbon particles, was slightly reduced compared with the direct addition of the combined molecules, in particular for BMDG-Norit treatment.

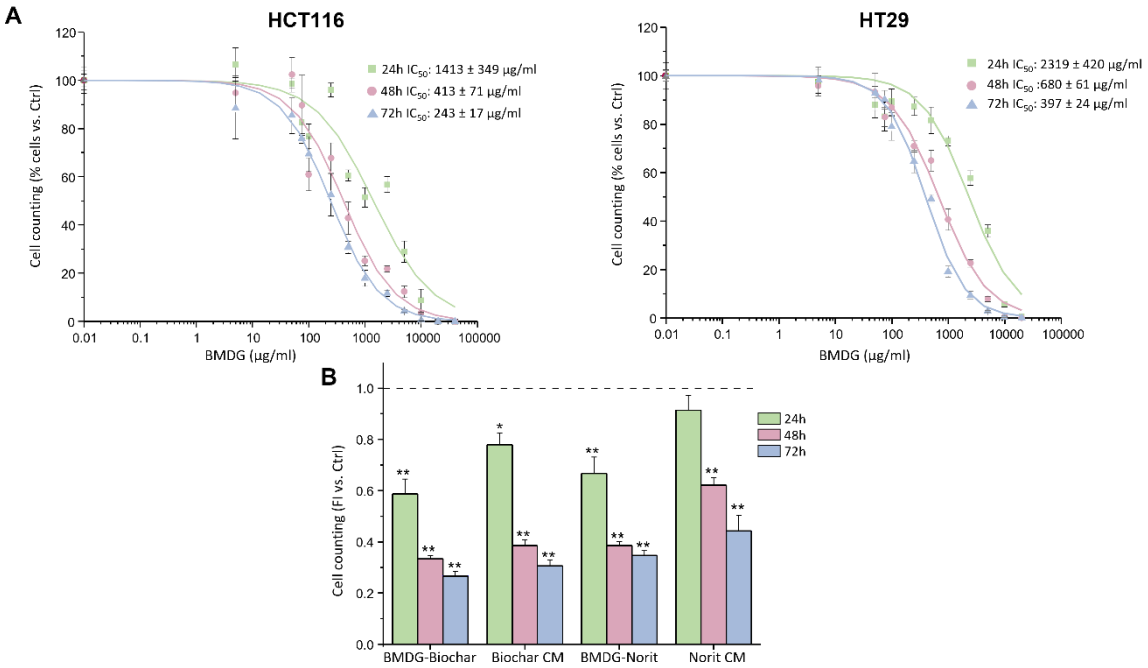

Figure 8. Inhibitory effect of BMDG alone and absorbed on Biochar or Norit-B on cell number. (A) Cell number was expressed as mean percentage ± SE in n=4 replicates for each BMDG dose at the indicated time points (24, 48, 72 hours) over controls (untreated cells) taken as 100% in HCT116 or HT29 cells. Sigmoid models have been fitted and IC_{50} of BMDG for each time point in each cell type as indicated. (B) HCT116 cells were treated for the indicated time intervals directly with BMDG-Biochar and BMDG-Norit (with BMDG concentration obtained from thymidine experiments at 24 hours) or with the conditioned media depleted from carbon powders obtained after 24-hour incubation with BMDG-Biochar or BMDG-Norit, respectively (Biochar CM and Norit CM). Cell number was expressed as the mean ± SE of fold decrease over controls taken as 1 (Ctrl, dotted line) in n=3 independent experiments with each point performed in triplicate; statistical analysis was performed with ANOVA followed by Bonferroni's *post hoc* test *p <0.05, ** p <0.001 vs. control.

The higher sensitivity of HCT116 cells compared to HT29 was further confirmed by the ability of the compounds to directly interfere with DNA duplication, as evaluated by ^{3}H-thymidine incorporation. To calculate BMDG IC_{50} for DNA replication, HCT116 and HT29 were treated with increasing concentrations of BMDG for 24 and 48 hours, resulting in a significantly lower IC_{50} for HCT116 at 48 hours (111 μg/ ml vs 313 μg/ml) (Figure 9A). For the rest of the experiments, BMDG and the combined compounds were used at the dose corresponding to the mean IC_{50} at 24 hours derived from thymidine incorporation in HCT116 and HT29 cells (corresponding to the presence of 32.9% of Biochar and 38.5% of Norit-B, respectively). When the effect on cell proliferation was compared among the different compounds, BMDG alone and absorbed on Biochar exerted a similar inhibitory effect on DNA duplication, with no effect when absorbed on Norit-B (Figure 9B). No inhibitory effect was associated with the treatment with free carbons. Of note, BMDG-Biochar's interference with cell proliferation was significantly higher in HCT116 compared to HT29 cells (Figure 9B). Treatment with BMDG-Norit was associated with an apparent increase in tumour cell proliferation. However, this observation may be explained by the capacity of the microporous structure of activated

carbon to adsorb small molecules, likely including tritiated thymidine. Indeed, despite the multiple washing steps performed prior to radioactivity measurement, small amounts of Norit-B may remain and contaminate the liquid scintillator. Therefore, it cannot be excluded that part of the detected radioactivity derives not from thymidine incorporated into cellular DNA, but from unincorporated thymidine absorbed on residual Norit-B particles remaining in the treatment wells (Figure 9B).

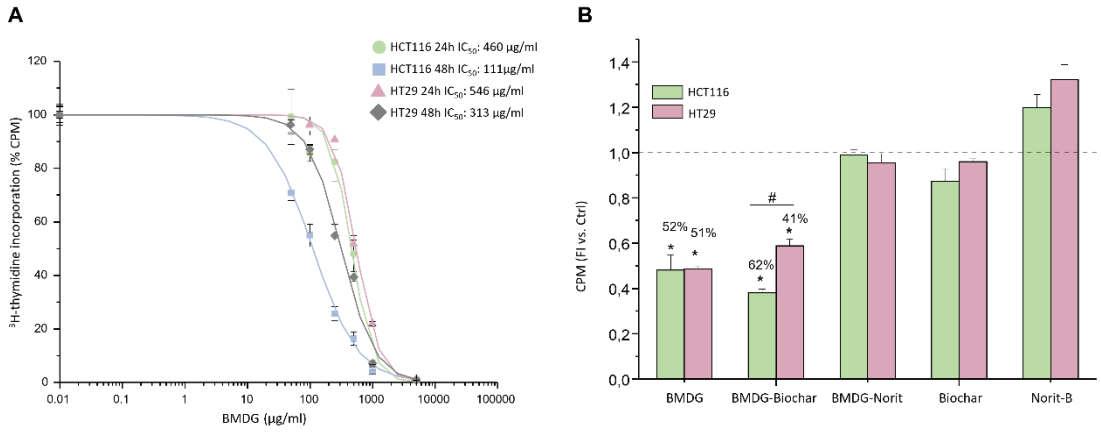

Figure 9. The inhibitory effects exerted by the different compounds on cell proliferation. (A) Cell proliferation was assessed in HCT116 and HT29 cells treated for 24 and 48 hours with increasing concentration of BMDG through ^{3}H-thymidine incorporation into replicating DNA. Cell number was expressed as the mean percentage ± SE of CPM over controls (untreated cells) taken as 100%. Sigmoid models have been fitted and IC_{50} of BMDG for each time point in each cell type, as indicated. (B) Cell proliferation was evaluated by ^{3}H-thymidine incorporation into duplicating DNA in HCT116 and HT29 cells treated for 24 hours with the different compounds and indicated as mean ± SE of CPM expressed as fold increase over untreated controls taken as 1 (Ctrl, dotted line) in n=3 independent experiments with each point performed in triplicate. The BMDG dose used (500 µg/ml) was calculated by averaging the 24 hour-IC_{50} obtained from thymidine incorporation experiments in HCT116 and HT29 cells. Statistical analysis was performed with ANOVA followed by Bonferroni's *post hoc* test **p* <0.001 vs. controls or with Student's t-test $^{\#}p$ <0.001 HCT116 vs. HT29 cells.

The absence of any significant effect on cell proliferation in non-tumoral human colon epithelial cell line (HCEC-1CT), treated under the same conditions with BMDG alone or

absorbed on Biochar or Norit-B and used as a negative control, confirms that the inhibition of DNA replication is specific for CRC cells (Figure 10, left panel). The viability assay further corroborated the safety of the selected dose in the normal colon cell line (Figure 10, right panel). Due to the well-known absorption capacity of Norit-B, it was not possible to perform the resazurin-based viability assay on cells treated with BMDG–Norit.

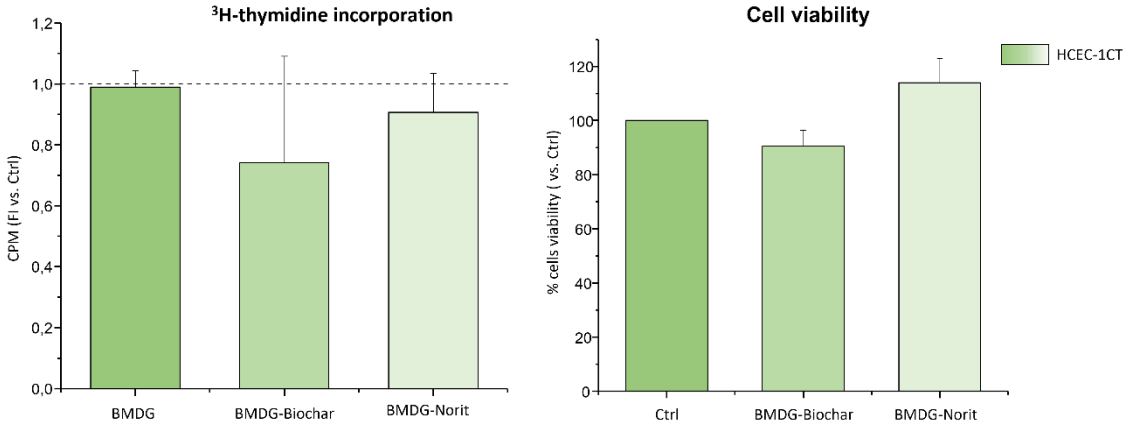

Figure 10. The effects exerted by the different compounds on HCEC-1CT proliferation and viability. Cell proliferation (left panel) was evaluated by ^{3}H-thymidine incorporation into duplicating DNA in HCEC-1CT cells treated for 24 hours with 500 µg/mL of free and absorbed BMDG and indicated as mean ± SE of CPM expressed as fold increase over untreated controls taken as 1 (Ctrl, dotted line) in n=3 independent experiments with each point performed in triplicate. Cell viability (right panel) was evaluated by Resazurin assay in HCEC-1CT cells treated for 24 hours with 500 µg/mL of free BMDG and BMDG-Biochar and expressed as mean ± SE of the percent difference in resazurin reduction between treated and control cells in n=4 independent experiments with each point performed in triplicate. Statistical analysis was performed with ANOVA followed by Bonferroni's *post hoc* test. No significant differences were observed across treatment groups.

To investigate the effects of the combined molecules in a model more closely recapitulating the *in vivo* CRC, their activity was evaluated in the mouse intestinal organoid cultures carrying the AKPS genotype (*Apc* $^{fl/fl}$; *Kras*$^{G12D/+}$; *Trp53*^{KO}; *Smad4*^{KO})

associated with the development of CRC (Drost et al., 2015; Fearon & Vogelstein, 1990; X. Li et al., 2014; Matano et al., 2015). To calculate BMDG IC_{50} for cell viability, AKPS organoids were treated with increasing concentrations of BMDG for 24 hours (Figure 11). A sigmoidal dose-response model could not be fitted and the IC_{50} could not be determined, as the tested concentrations did not reduce cell viability to sufficiently low levels, reaching a maximum cytotoxic effect of approximately 25% even at the highest dose tested (Figure 11B). The experimental dose range was also found to significantly affect organoid area, with a reduction observed starting at 250 µg/mL and reaching a maximal decrease of 31% in organoids treated with 1000 µg/mL of BMDG (Figure 10B).

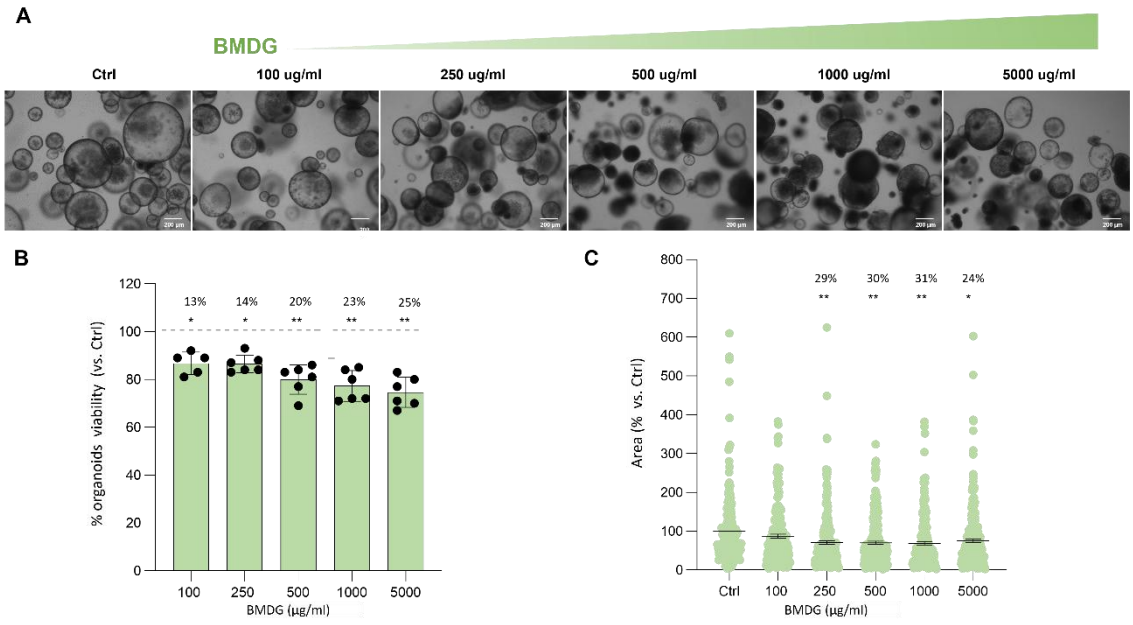

Figure 11. The effects exerted by BMDG on AKPS viability and area of the organoids. (A) Representative optical microscope images of AKPS organoids from the different experimental groups. (B) Cell viability was evaluated by Resazurin assay in AKPS organoids treated for 24 hours with increasing doses of free BMDG and expressed as mean ± SD of the percent difference in resazurin reduction between treated and control organoids (dotted line) in n=3 independent experiments with each point performed in triplicate. (C) Area was measured using Fiji (ImageJ 1.54p) and expressed as the mean ± SE of the relative reduction (%) to the control. Statistical analysis was performed with ANOVA followed by Bonferroni's *post hoc* test *p <0,05; ** p <0,001 vs control (Ctrl).

For the rest of the experiments on AKPS organoids, BMDG and the combined compounds were used at the dose of 1000 µg/mL (considering again the presence of 32.9% of Biochar and 38.5% of Norit-B in the combined molecules, respectively). As expected, a comparative analysis of the effects of the different compounds on organoid viability revealed that BMDG alone and BMDG absorbed on Biochar exerted a similar significant cytotoxic effect, with a reduction in cell viability of 14% and 17%, respectively. No cytotoxic effect was associated with treatment with Biochar alone (Figure 12B). While BMDG-Norit interfered with cell proliferation by 32%, a stronger effect on DNA duplication was observed in the presence of BMDG alone and BMDG-Biochar, with reductions of 92% and 90% respectively (Figure 12C). Regarding organoid area (Figure 12D), only BMDG-Biochar induced a significant decrease (28%).

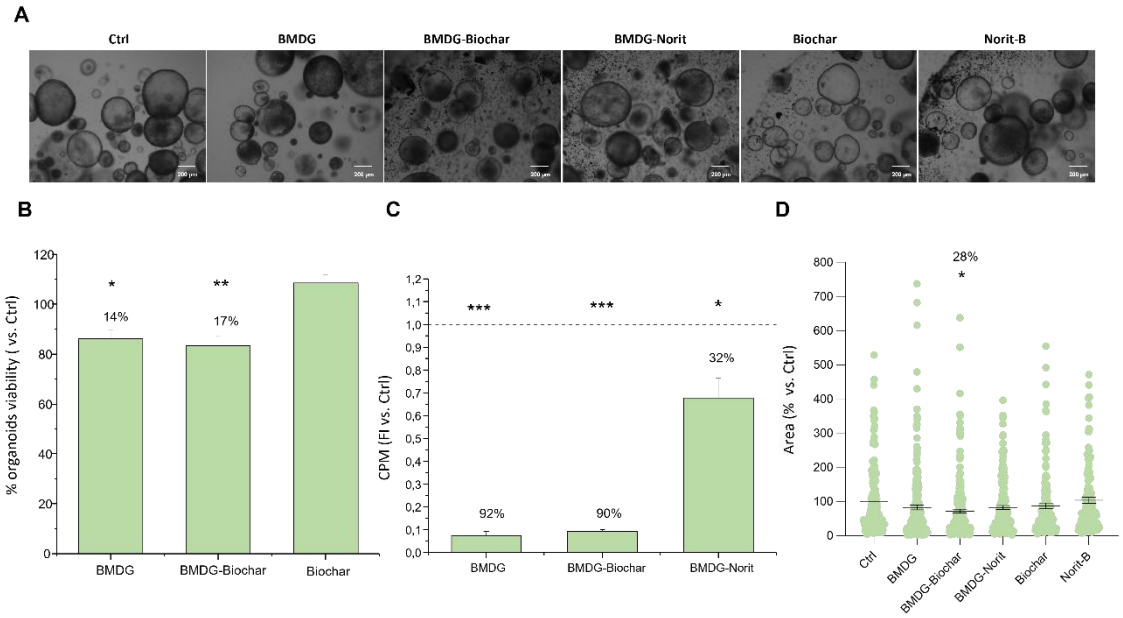

Figure 12. The effects exerted by combined molecules on AKPS vitality, proliferation and area. (A) Representative optical microscope images of AKPS organoids from the different experimental groups. (B) Cell viability was evaluated by Resazurin assay in AKPS organoids treated for 24 hours with 1000 µg/mL of free BMDG, absorbed BMDG and Biochar alone and expressed as mean ± SE of the percent difference in resazurin reduction between treated and control organoids (dotted line) in n=6 independent experiments with each point performed in triplicate. (C) Cell proliferation was evaluated by ^{3}H-thymidine incorporation into duplicating DNA in AKPS organoids treated for 24 hours with 1000 µg/mL of free and absorbed

BMDG and indicated as mean ± SE of CPM expressed as fold increase over untreated controls taken as 1 (Ctrl, dotted line) in n=3 independent experiments with each point performed in triplicate. (D) Area was measured using Fiji (ImageJ 1.54p) and expressed as the mean ± SE of the relative reduction (%) to the control. Statistical analysis was performed with ANOVA followed by Bonferroni's *post hoc* test * p <0,05; ** p <0,01; *** p <0,001 vs controls (Ctrl).

In order to investigate at cellular level, the interaction between carbon particles and CRC models during the *in vitro* treatment, an ultrastructure analysis of the treated cells was performed. HCT116, HT29 cells and AKPS organoids were left untreated or treated for 24 hours with 500 or 1000 µg/mL BMDG alone or absorbed on Biochar or Norit-B, respectively.

TEM analysis of HCT116 (Figure 13 panels A-F) and HT29 (Figure 13 panels G-L) cells clearly showed that the treatment with BMDG-Biochar (panels D, E and J, K) and BMDG-Norit (panels F and L) induced some cells to internalise carbon particles into large lysosomes and to undergo deformation of their shape. BMDG (alone or absorbed on carbons) treatment was associated with moderate signs of cell differentiation, namely expansion of rough endoplasmic reticulum (RER) cisternae, increased number of rod-shaped mitochondria with darker matrix and surface microvilli, all features resembling those of the normal colonic surface epithelium. These features were more evident in undifferentiated HCT116 (Figure 13A vs B, C and D-F) as compared with the more differentiated HT29 (Figure 13G vs H, I and J-L) cells. These latter ones also showed diffuse surface microvilli in untreated controls (Figure 13G vs A). Furthermore, in the presence of BMDG, autophagy was more evident.

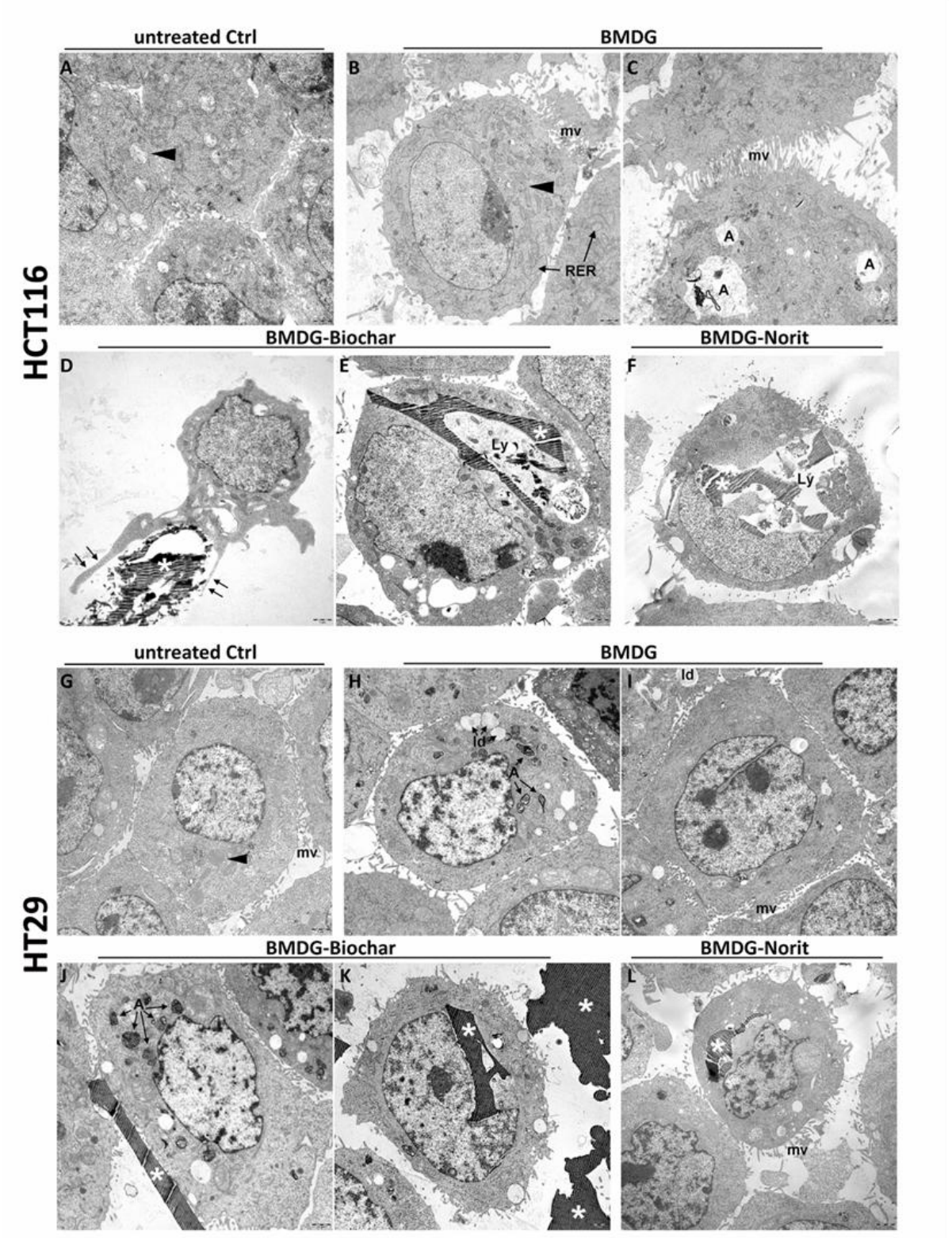

Figure 13. Representative TEM images of HCT116 and HT29 cells from the different experimental groups. HCT116 cells (A-F). (A) The untreated control shows features of undifferentiated cells, with few organelles and roundish mitochondria with clear matrix (arrowhead). (B, C) Treatment with BMDG induced moderate signs of cell differentiation, namely an increase in RER cisternae, rod-shaped mitochondria with darker matrix (arrowhead), and surface microvilli (mv) reminiscent of those of the normal colonic surface

epithelium. Autophagosomes (A), an index of the occurrence of increased autophagy, can also be seen. (D-E) Treatment with BMDG-Biochar also induced similar signs of cell differentiation. Moreover, the cells tended to attach to the carbon surface and to phagocytize carbon particles (asterisks), which are internalised by lamellipodia (double arrows) into large lysosomes (Ly). (F) Treatment with BMDG-Norit induced similar effects as BMDG-Biochar. Magnification: x10.000. Scale bars are indicated at the bottom in black: scale bars = 1 µm. HT29 cells (G-L). (G) The untreated control grew as epithelial clusters and showed a regular organellular complement, with several roundish mitochondria with numerous cristae (arrowhead), and surface microvilli (mv). (H, I) Treatment with BMDG induced an increase in autophagosomes (A), an index of the occurrence of increased autophagy, and the appearance of scattered lipid droplets (ld), not appreciable in HCT116 cells, further confirming the higher basal level of differentiation characterising HT29 compared to HCT116 cells. Surface microvilli also increased in some cell clusters. (J, K) Treatment with BMDG-Biochar induced similar changes as BMDG alone, particularly autophagosomes (A). The cells tended to attach to the carbon surface and to phagocytise carbon particles (asterisks), which are internalised into large lysosomes. (L) Treatment with BMDG-Norit induced similar effects as BMDG-Biochar; mv, microvilli. Magnification: x10.000. Scale bars are indicated at the bottom in black: scale bars = 1 µm.

TEM analysis of AKPS organoids (Figure 14) revealed notable differences compared to cell lines. AKPS are characterised by the presence of swollen mitochondria with a reduction in cristae extent. In addition, treatment with BMDG-Biochar (panels G-I) and BMDG-Norit (panels J-L) did not induce internalization of carbon particles. Treatment with BMDG, either alone or absorbed on chars, was associated with moderate features of cellular differentiation. However, most cells lacked clear polarization, displaying microvilli on both apical and basolateral surfaces. When BMDG was absorbed on Biochar, mitochondria appeared less swollen and retained more preserved cristae morphology. In contrast, in the presence of BMDG-Norit, ultrastructural observations suggest a possible activation of mitochondrial fission processes, potentially reflecting an adaptive response to stress. Images suggest that mitochondrial impairment may be linked to enhanced lipogenesis, as indicated by the accumulation of lipid droplets. This effect was particularly evident in BMDG and BMDG-Norit treatments, which also showed more pronounced mitochondrial alterations.

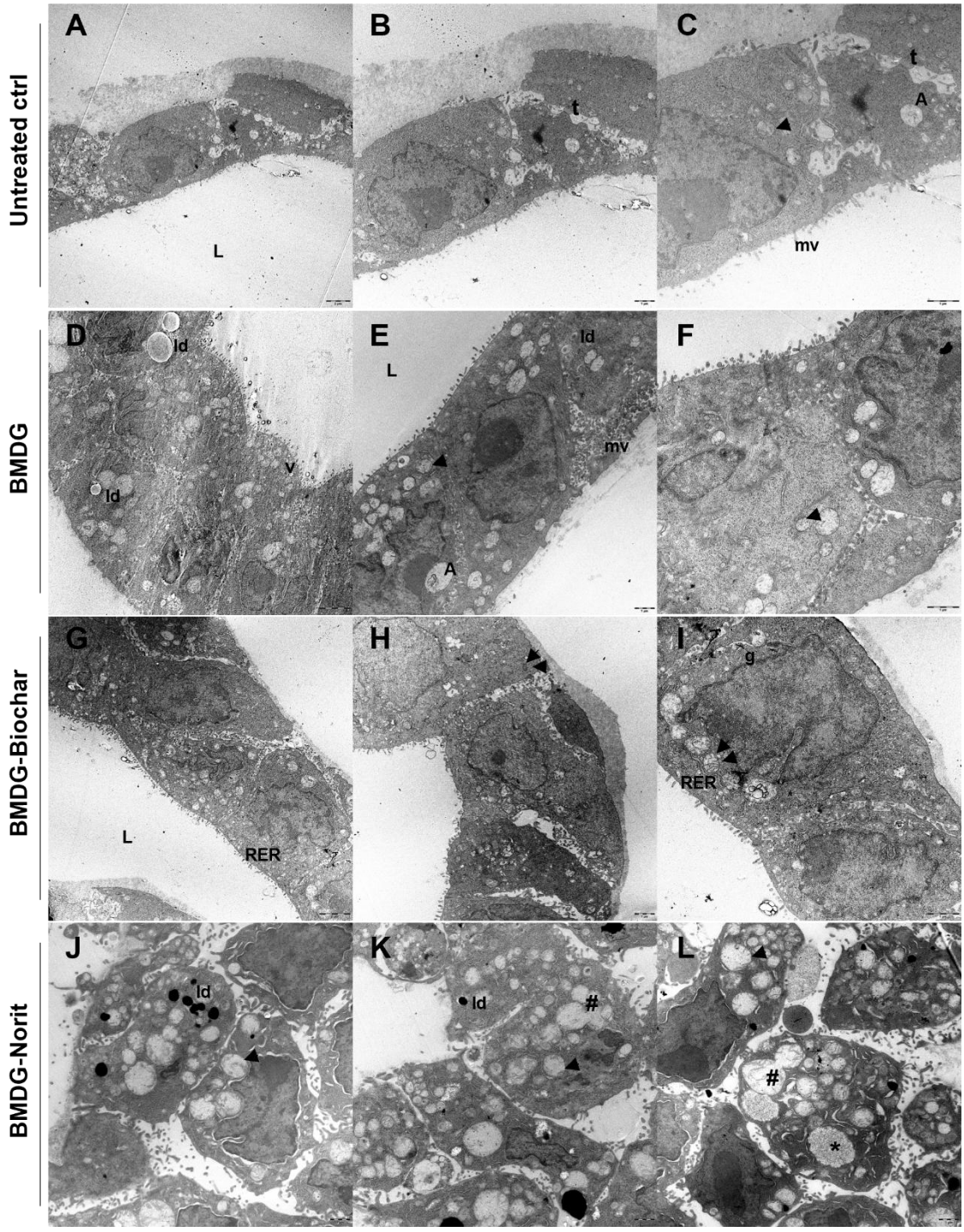

Figure 14. Representative TEM images of AKPS organoids from the different experimental groups. (A-C) The untreated control shows an epithelial layer with a polarized absorptive surface and microvilli (mv), and a differentiation toward a classic intestinal phenotype with tight junctions (t) typical of enterocytes. Autophagosomes (A), an index of the occurrence of increased autophagy, can also be seen. Mitochondria (arrowheads) appear swollen, with a reduction in cristae extent, consistent with altered cellular metabolism Magnification: x6,000, x10,000 and x15,000 respectively. (D-F) Treatment with BMDG induced extensive vacuolization (v). Mitochondria (arrowheads) appear swollen. Moderate signs of cell differentiation are observed, characterised by a loss of clear topographical organization and slight depolarization, with

microvilli (mv) also present on the basolateral surface. Limited autophagy (A) is detectable, together with the appearance of few lipid droplets (ld), likely resulting from mitochondrial dysfunction that may stimulate lipogenesis and triglyceride storage. Magnification: x8,000, x10,000 and x15,000 respectively. (G-I) Treatment with BMDG-Biochar induced signs of cell differentiation. Mitochondria appear slightly swollen, but with normally appearing cristae (double arrows), whereas swollen mitochondria are less frequent compared to treatment with free BMDG. The rough endoplasmic reticulum (RER) is clearly visible, and the Golgi cisternae (g) are also well defined. Magnification: x8,000, x10,000 and x15,000 respectively. (J-L) In this experimental group, the lumen (L) can't be identified. Treatment with BMDG–Norit induced effects similar to those observed with BMDG in terms of lipid droplet (ld) formation. Mitochondria (arrowheads) appear swollen, and images suggesting mitochondrial fission (#) can be observed, possibly representing an attempt to increase the chondriome in response to oxidative mitochondrial dysfunction. Numerous large vacuoles are clearly visible; some of them may contain glycogen accumulations (*), likely associated with impaired glucose metabolism. Magnification: x10.000. Scale bars are indicated at the bottom in black: scale bars = 1 µm.

To explore if the different sensitivity of HCT116, HT29, AKPS and normal HCEC-1CT to free and absorbed BMDG could be justified by the difference in the metabolic profiles, cell metabolic behaviour was investigated after 24-hour treatment with BMDG-compounds using the Seahorse technology.

Starting from the cell lines, when dissecting the mitochondrial function at different levels by measuring OCR during the sequential addition of mitochondrial inhibitors, the respiration time course curves showed the higher basal mitochondrial activity and responsiveness to mitochondrial stress (higher maximal respiration levels after FCCP injection) of HCT116 compared to HT29 and HCEC-1CT, indicating a greater energetic demand in the carcinoma cell line compared to the adenocarcinoma and non-tumoral ones (Figure 15A). Interestingly, when BMDG is absorbed on Biochar, total OCR levels of HCEC-1CT appear to be increased compared to the untreated control, indicating an enhancement of mitochondrial respiration (Figure 15A). In HCT116 cells, BMDG absorbed on Biochar or Norit-B significantly inhibited both basal and maximal

mitochondrial respiration (Figure 15B), while BMDG alone affected the basal respiration only. In contrast, in HT29 cells, BMDG resulted in a dramatic reduction of both respiratory parameters, and only when absorbed on Norit-B interfered with maximal respiration but not with basal respiration (Figure 15B). Conversely, BMDG-Biochar was ineffective on mitochondrial respiration in HT29 cells. As expected, BMDG does not affect mitochondrial activity in HCEC-1CT cells (Figure 15B). On the contrary, consistent with what was observed in the respiration curves (Figure 15A), there is evidence of increased basal mitochondrial respiration and a significant ability of the cells to respond to elevated energy demand (maximal respiration) when treated with BMDG-Biochar (Figure 15B). As observed in the other cellular models, when BMDG is absorbed on Norit-B, it significantly affects maximal respiration (Figure 15B). Since glucose represents a key substrate for mitochondrial respiration, and as shown in Table 4 Norit-B exhibits a strong capacity to absorb glucose, it is reasonable to hypothesize that the reduced glucose availability may limit the metabolic flexibility of the cells, particularly under conditions of increased energy demand following FCCP injection. These different effects of the compounds resulted in a different impact on total ATP production, derived from both glycolysis and mitochondrial respiration (Figure 15B, right panel). In HCEC-1CT cells, total ATP production is not affected, likely due to a concurrent increase in glycolytic activity. HCT116 cells only were sensitive to ATP production inhibition exerted by BMDG when absorbed on Biochar or Norit-B, while free BMDG was effective in both tumoral cell types (Figure 15B). HCT116 relied to a higher extent on the glycolytic production of ATP, compared to HT29 where the Warburg effect is very limited and ATP mostly derived from mitochondrial oxidative phosphorylation (OXPHOS) (see Figure 7C, D).

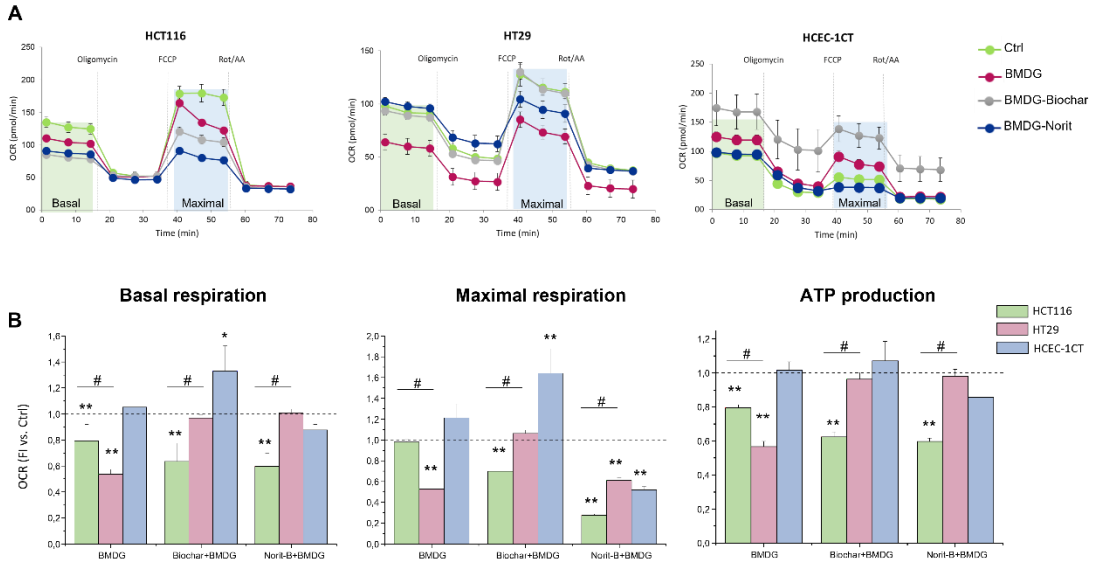

Figure 15. Effects of BMDG compounds on mitochondrial functionality in HCT116, HT29 and HCEC-1CT cells. (A) Representative oxygen consumption rate (OCR) curves as obtained through Seahorse analysis (Mito Stress test) in HCT116 (left panel), HT29 (middle panel) and HCEC-1CT (right panel) cell lines following 24 hour-treatment with 500 µg/mL of BMDG, BMDG-Biochar and BMDG-Norit or in untreated cells used as control (Ctrl). Sequential addition of drugs used for Seahorse measurements is indicated. (B) OCR levels, expressed in pmol/min for basal, maximal respiration and ATP production, were measured in HCT116, HT29 and HCEC-1CT cells after 24-hour treatment with the already mentioned compounds. Results were indicated as mean ± SE of fold increase over untreated controls taken as 1 (Ctrl, dotted line) in at least n=3 independent experiments. Statistical analysis was performed with ANOVA followed by Bonferroni's and Dunnett's *post hoc* test * $p < 0,05$; ** $p < 0.001$ vs controls or with Student's t-test $^{\#}p < 0.001$ HCT116 vs HT29 cells.

When conducting the analysis on organoids, ensuring adequate penetration of test drugs through a three-dimensional structure - characterised by gradients in oxygen, nutrients, and treatment exposure - required modifications to the protocol, including an increase in the number of cycles and the duration of measurements (Figure 16B). In this model, only treatment with 1000 µg/ml BMDG absorbed on Norit-B had a significant negative effect on both basal and maximal respiration (Figure 16B). In this context as well, the glucose-absorbing capacity of Norit-B cannot be excluded, which may exert an even more

pronounced effect in a complex system such as organoids. Though not statistically significant, also BMDG adsorbed on Biochar display an inhibitory trend.

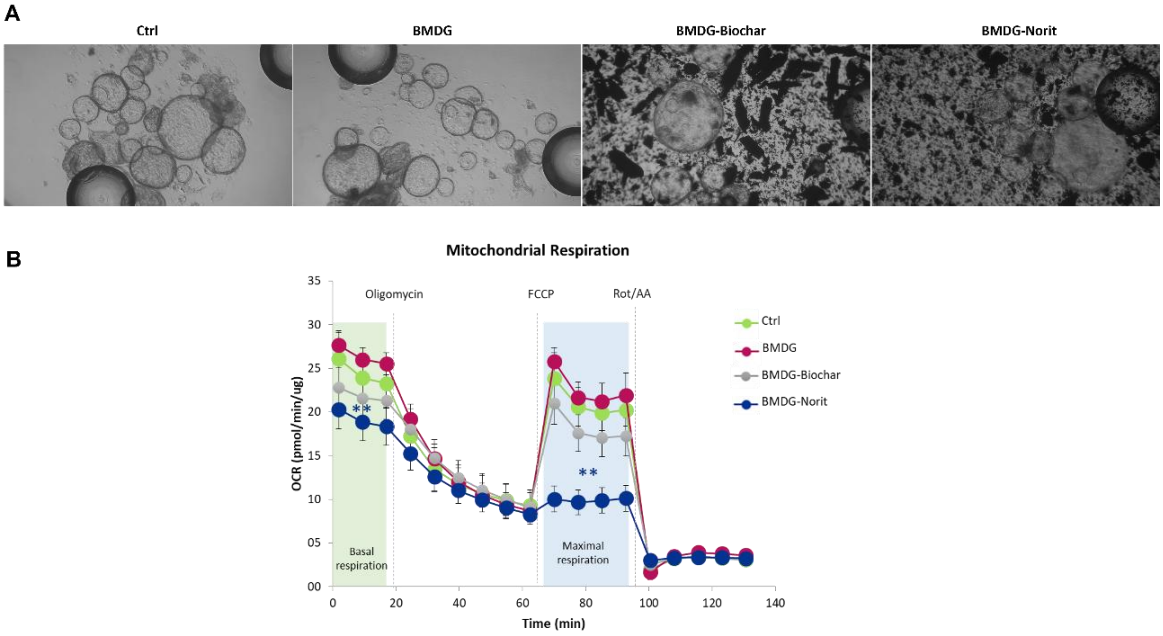

Figure 16. Mito stress test performed on AKPS organoids. (A) Representative images on AKPS organoids plated in Seahorse cell culture microplates. For the analysis, only wells containing well-formed organoids positioned in the centre were selected. (B) Representative oxygen consumption rate (OCR) curves as obtained through Seahorse analysis (Mito Stress test) in AKPS organoids following 24 hour-treatment with 1000 µg/mL of BMDG, BMDG-Biochar and BMDG-Norit or in untreated organoids used as control (Ctrl). Sequential addition of drugs used for Seahorse measurements is indicated. OCR levels are expressed in pmol/min/ug. Results derived from the mean ± SE of fold increase over untreated controls in n=3 independent experiments. Statistical analysis was performed with ANOVA followed by Bonferroni's and Dunnett's *post hoc* test ** p <0.001 vs controls.

Therefore, the effects of BMDG compounds on the relative contributions of glycolytic and OXPHOS ATP production pathways were further investigated in both tumoral cell lines (Figure 17) and AKPS organoids (Figure 18).

Seahorse ATP rate analysis in HT29 cells showed that all three BMDG compounds significantly increased ATP production via glycolysis, accompanied by a reduction in

mitochondrial ATP production compared to the untreated control (Figure 17A, left panel). In contrast, HCT116 cells displayed the opposite response, with a significant decrease in glycolytic activity (BMDG-Biochar: 22%, BMDG: 13%, BMDG-Norit: 12%). Notably, the inhibitory effect on glycolysis exerted by BMDG-Biochar was significantly greater than that of free BMDG or BMDG-Norit ($p < 0.05$), despite the glucose-adsorbing properties of the latter (Figure 17A, right panel).

Focusing on HCT116 cells - since glycolysis represents a preferred metabolic pathway supporting anabolic processes in cancer cells - the energetic map highlights that BMDG-Biochar was the most effective treatment in inducing a metabolic shift from a highly energetic phenotype toward a more OXPHOS-dependent and quiescent state (Figure 17B, right panel). This shift was primarily driven by inhibition of glycolytic activity, as evidenced by the reduction in Proton Efflux Rate (PER), a quantitative measure of extracellular acidification largely resulting from proton production and export during glycolysis (Figure 17B, left panel).

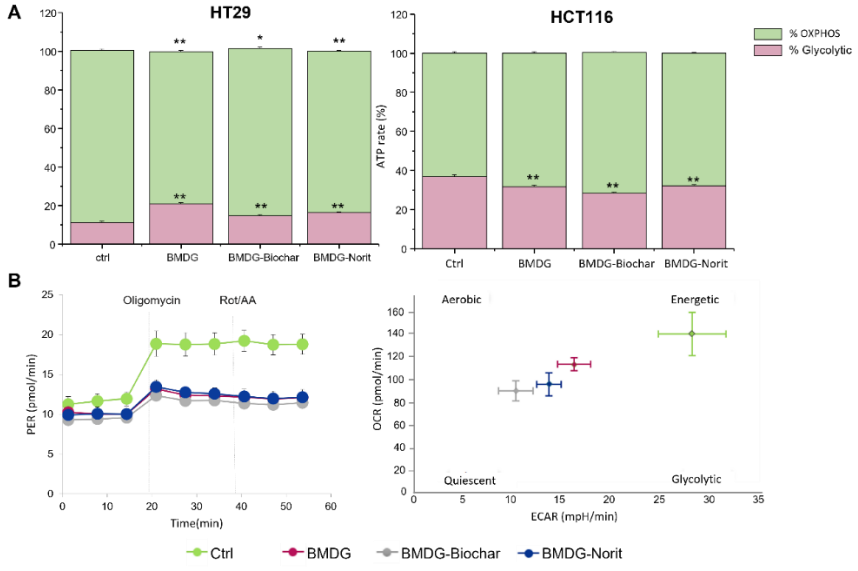

Figure 17. Effects of BMDG compounds on ATP production and energetic metabolism in HT29 and HCT116 cells. (A) Analysis of basal ATP production rate (%) performed through Seahorse analysis (Real-

Time ATP rate test). Results are expressed as the mean ± SE of ATP production rate (OXPHOS and glycolytic %) obtained by treating HT29 and HCT116 cells for 24 hours with 500 µg/mL of BMDG, BMDG-Biochar and BMDG-Norit. Statistical analysis was performed with ANOVA followed by Bonferroni's *post hoc test* * p <0,05: ** p <0.001 vs. untreated cells (Ctrl). (B) Left panel: the proton efflux rate (PER, pmol/min) was measured through Seahorse analysis (Real-Time ATP rate test) in HCT116 cell line following 24-hour treatment with 500 µg/mL of BMDG, BMDG-Biochar and BMDG-Norit or in untreated cells used as control (Ctrl). Right Panel: the energy map shows the change in the metabolic profile of HCT116 cells treated with 500 µg/mL of BMDG, BMDG-Biochar and BMDG-Norit compared to that of the untreated control (Ctrl).

Moving on to AKPS organoids, total ATP production was significantly reduced upon treatment with 1000 µg/mL BMDG absorbed on both Biochar and Norit-B (Figure 18A), although no significant changes were observed in the relative contributions of OXPHOS and glycolysis (Figure 14B). Notably, BMDG absorbed on Biochar showed a tendency to reduce the contribution of the glycolytic pathway, a trend not evident with free BMDG or BMDG-Norit, for which a slight increase was instead observed. As illustrated in Figure 18C, the reduction in total ATP production was driven by a significant decrease in glycolytic ATP production rate in organoids treated with BMDG-Biochar and BMDG-Norit (left panel). While mitochondrial ATP production was not significantly affected by free BMDG or BMDG-Biochar, it was significantly impaired in organoids treated with BMDG-Norit (right panel), in agreement with the findings reported in Figure 16 and with the hypothesis that Norit-B absorption capacity limits the availability of glucose, which is essential for both metabolic processes. The decreasing trend observed with BMDG-Biochar and the significant reduction induced by BMDG-Norit in mitochondrial ATP production (Figure 18C, right panel) likely contribute to the absence of significant changes in the relative balance between metabolic pathways shown in panel B.

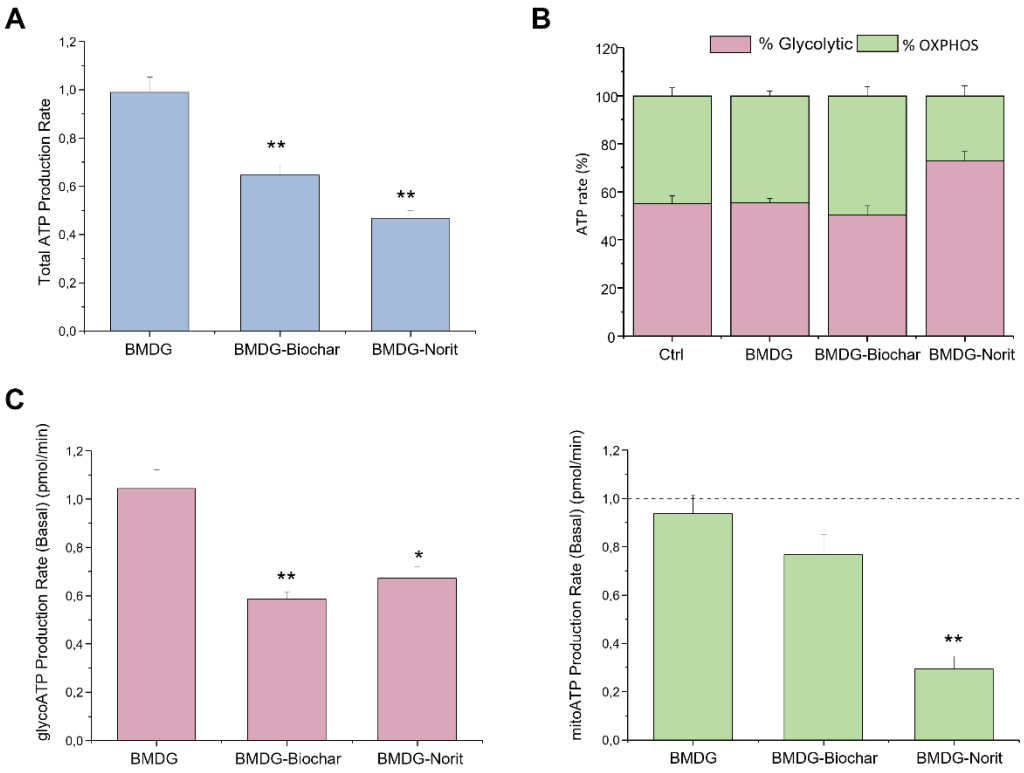

Figure 18. Effects of BMDG compounds on ATP production and energetic metabolism in AKPS organoids. (A) Analysis of Total ATP production rate performed through Seahorse analysis (Real-Time ATP rate test) after 24-hour treatment with 1000 µg/mL of BMDG, BMDG-Biochar, BMDG-Norit. Results are indicated as mean ± SE of fold increase over untreated controls taken as 1 (Ctrl, dotted line). (B) Analysis of basal ATP production rate (%). Results are expressed as the mean ± SE of ATP production rate (OXPHOS and glycolytic %) obtained by treating AKPS for 24 hours with the already mentioned compounds. (C) Analysis of glycolytic (left panel) and mitochondrial (right panel) ATP production rate obtained by 24-hour treatment of AKPS organoids. Results are indicated as mean ± SE of fold increase over untreated controls taken as 1 (Ctrl, dotted line). Statistical analysis was performed with ANOVA followed by Bonferroni's *post hoc test* * p <0,05: ** p <0.001 vs. untreated cells (Ctrl).

4.3 Effects of *in vivo* administration of BMDG compounds on tumour and adipose microenvironment transcriptome

This thesis work is part of a larger project that included animal experimentation on C57BL/6 mice treated with AOM/DSS to promote chronic inflammation and induce the formation of colorectal tumours. These mice were subjected to two treatment models of BMDG, both in free form and absorbed on Biochar and Norit-B: a preventive model (where mice were treated prior to AOM/DSS administration and throughout the entire experimental phase) and a therapeutic model (where mice were treated after tumour formation had already occurred). The dose was selected considering free butyrate as the bioactive molecule present in BMDG and in accordance with the butyrate dose reported in the literature (1 g/kg) (Y. Du et al., 2020). Mice treated with AOM/DSS but not subjected to either of the two treatment models were used as untreated controls.

In this context, another purpose of this thesis was to observe how the treatment affected gene expression at the transcriptional level in tumour nodules, intestinal mucosa distant from the tumour, and peritumoral adipose tissue, in order to investigate any potential effects on the adipose microenvironment. Also visceral adipose tissue distant from the tumour was analysed.

Based on the global transcriptional profiles obtained by mRNA-seq analysis (Figure 19A), tissue identity emerged as the primary variable driving samples clustering. The treatments did not appear to create distinct, separated subclusters, suggesting that they did not substantially influence the overall transcriptional profiles of any tissue, but rather introduce more subtle transcriptional variations. These observations were further supported by Principal Component Analysis (PCA) (Figure 19B-C). For both

experimental models, preventive (Figure 19B) and therapeutic (Figure 19C), the first principal component (PC1), which explained 77% and 81% of the total variance respectively, clearly separated samples according to tissue type. Non-tumoral mucosa and tumour samples formed distinct and relatively compact clusters in both models, while peritumoral adipose tissue displayed an intermediate, but separated cluster with some outliers - especially in the preventive model - probably reflecting biological heterogeneity of the tissue as well as the influence of the tumour microenvironment. Tumour samples were distinctly separated from both normal mucosa and peritumoral adipose tissue in both PCA, though closer to non-tumoral mucosa, highlighting the same enteric origin, respect with the adipose component. The second principal component (PC2), accounting for 13% and 10% of the variance, respectively, further contributed to separation among tissues, capturing additional minor variations. In both analysis, samples distribution, again, did not reveal any clustering based on the experimental treatment conditions.

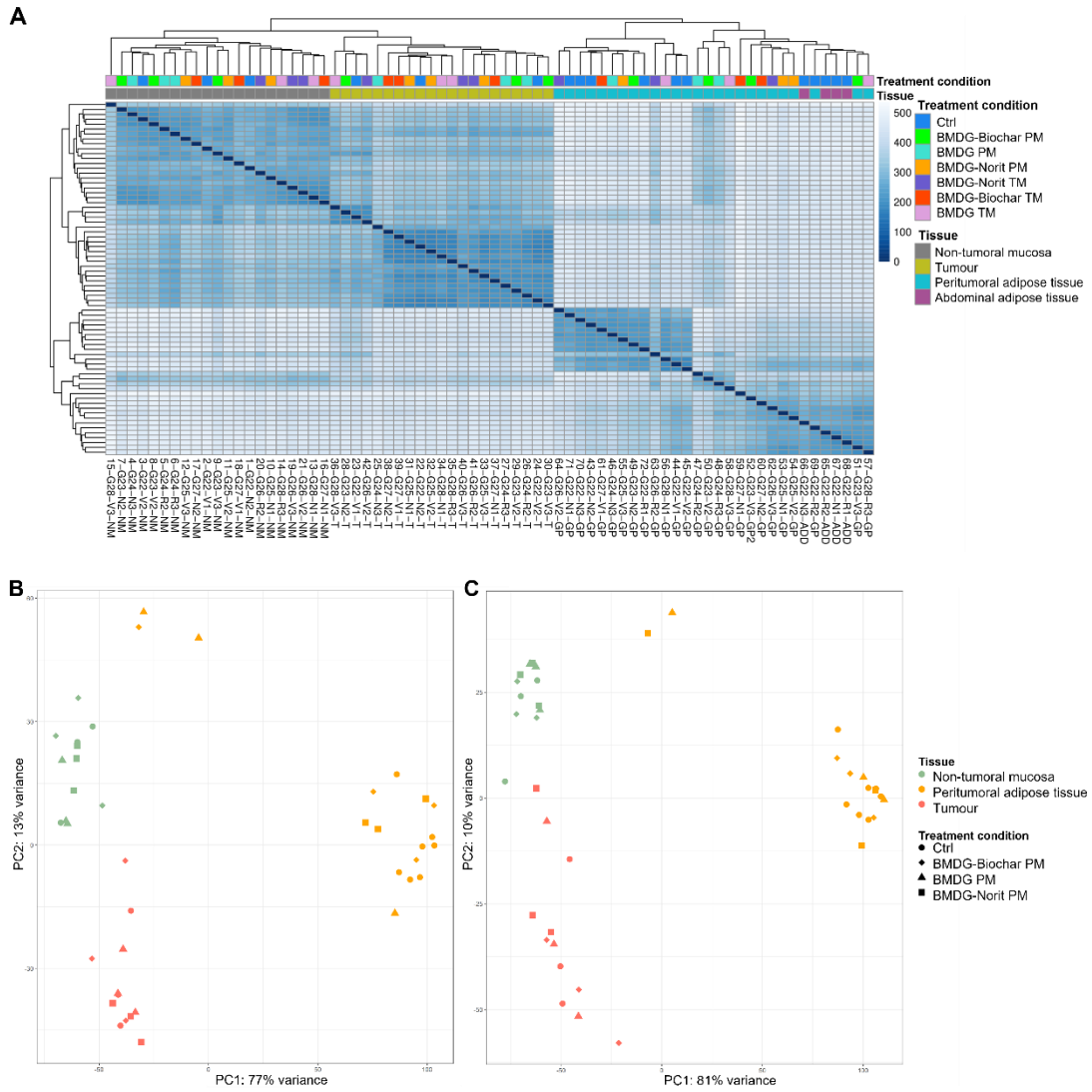

Figure 19. (A) Heatmap for the distance matrix. Columns are labelled with the information "tissue" (non-tumoral mucosa, tumour, peritumoral adipose tissue, abdominal adipose tissue) and "treatment condition" in both preventive (PM) and therapeutic (TP) models (untreated controls Ctrl, BMDG, BMDG-Biochar, BMDG-Norit). (B) Principal Component Analysis (PCA) of RNA-seq preventive model (PM) samples, based on data obtained by applying variance stabilizing transformation (vst) to raw counts using the DESeq2 package. Samples are coloured by tissue type and shaped by experimental treatment condition. PC1 and PC2 explain 77% and 13% of the total variance, respectively. Samples cluster primarily according to tissue type. (C) PCA of RNA-seq therapeutic model (TM), based on data obtained by applying vst to raw counts using the DESeq2. Samples are coloured by tissue type and shaped by experimental treatment condition. PC1 and PC2 explain 81% and 10% of the total variance, respectively. Samples cluster primarily according to tissue type.

To characterise the tumour-specific expression profile and distinguish it from the non-tumour-related, but chronic inflammation-associated signature likely globally induced by the AOM/DSS model, tumour tissue-specific differentially expressed genes (DEGs) and pathways were compared with those of non-tumoral mucosa from untreated mice, which, although distant from the tumour site, may also be affected by carcinogen/irritant-induced chronic inflammation. Gene set enrichment analysis performed using the Reactome pathway database (Korotkevich et al., 2019) (Figure 20A) revealed an upregulation of pathways related to proliferation (cell cycle, mitosis, synthesis of DNA), invasion (activation of metalloproteinases), epithelial integrity (keratinization, formation of the cornified envelope), mucosal defence (defensins, antimicrobial peptides) and inflammation (interleukins, cytokine and chemokines signalling) in tumour tissue compared to non-tumoral mucosa. In contrast, pathways involved in drug metabolism and metabolic processes appeared impaired, with a downregulation of mitochondrial metabolism-related pathways (aerobic respiration and respiratory electron transport) in particular. Differential gene expression analysis (Figure 20B) partially confirmed GSEA analysis showing an AOM/DSS-induced transcriptional reprogramming in tumour tissue compared to adjacent non-tumoral mucosa. In particular, genes involved in lipid metabolism, including *Pparα, Pparγ, Ppargc1β, Fabp2* and *Fabp4,* were significantly downregulated. Consistently, markers of intestinal cells differentiation (*Muc2, Clca1, Alpi, Cdx2*) were also reduced, suggesting a loss of mature epithelial identity (Genecards.org). The role of PPAR in CRC remains complex and context-dependent. *Pparα* has been implicated in inflammation-associated colorectal tumorigenesis, and its deficiency has been reported to enhance tumour development in experimental models. Interestingly, *Pparγ,* a key gene of adipogenesis and lipid metabolism highly expressed in adipose tissue and colon mucosa, is generally considered to exert tumour-suppressive

functions by limiting cell proliferation and modulating inflammatory responses (C. Wang et al., 2025a). In particular, *Pparγ* has been shown to negatively regulate pro-inflammatory signalling pathways, including NF-κB-mediated transcription (Genecards.org). *In vitro* and *in vivo* studies, including AOM-induced colon cancer models, support the antitumoral effects of *Pparγ* in terms of proliferation, angiogenesis, apoptosis, invasion and tumour-supporting metabolism, making it an actionable target for anticancer therapies (Liang et al., 2023; Luconi et al., 2025; C. Wang et al., 2025b; D. Wang & DuBois, 2010). Conversely, tumour tissue displayed an upregulation of inflammatory and immune response genes, including *Tnf*, *Ccl2, Cxcl9, Cxcl10, Nos2* and *Reg4*, consistent with the proinflammatory model of treatment. Notably, *Reg4* has been reported to be upregulated in inflammatory bowel disease, dysplastic lesions, and colorectal cancer (Zheng et al., 2022). In parallel, genes associated with tissue remodelling and invasion (*Mmp7, Mmp9, Mmp13*) and keratin genes (*Krt13, Krt14, Krt17, Krt20*) were significantly upregulated, indicating epithelial remodelling and activation of tissue repair programs following injury (Genecards.org). Moreover, evidence suggest that *Keratin17* is involved in metastasis and angiogenesis in CRC (Ji et al., 2021). Finally, the stem cell marker *Lgr5* was upregulated, suggesting increased cell plasticity and regenerative capacity. It is well-known that *Lgr5* overexpression is involved in tumour proliferation, invasion and chemotherapy resistance, supporting the maintenance of cancer stem cells (W. Wang et al., 2025).

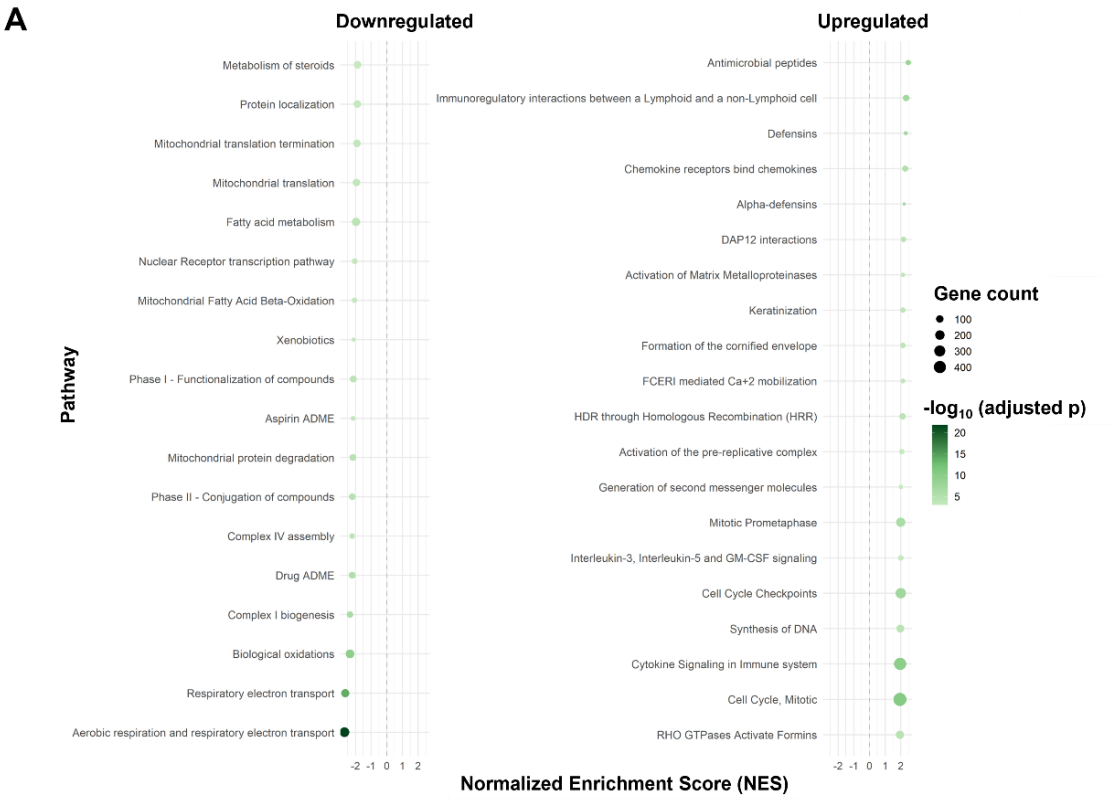
A
Downregulated
Upregulated
Metabolism of steroids
Protein localization
Mitochondrial translation termination
Mitochondrial translation
Fatty acid metabolism
Nuclear Receptor transcription pathway
Mitochondrial Fatty Acid Beta-Oxidation
Xenobiotics
Phase I - Functionalization of compounds
Aspirin ADME
Mitochondrial protein degradation
Phase II - Conjugation of compounds
Complex IV assembly
Drug ADME
Complex I biogenesis
Biological oxidations
Respiratory electron transport
Aerobic respiration and respiratory electron transport
Antimicrobial peptides
Immunoregulatory interactions between a Lymphoid and a non-Lymphoid cell
Defensins
Chemokine receptors bind chemokines
Alpha-defensins
DAP12 interactions
Activation of Matrix Metalloproteinases
Keratinization
Formation of the cornified envelope
FCERI mediated Ca+2 mobilization
HDR through Homologous Recombination (HRR)
Activation of the pre-replicative complex
Generation of second messenger molecules
Mitotic Prometaphase
Interleukin-3, Interleukin-5 and GM-CSF signaling
Cell Cycle Checkpoints
Synthesis of DNA
Cytokine Signaling in Immune system
Cell Cycle, Mitotic
RHO GTPases Activate Formins
-2 -1 0 1 2
Pathway
Normalized Enrichment Score (NES)
Gene count
100
200
300
400
-log10 (adjusted p)
20
15
10
5

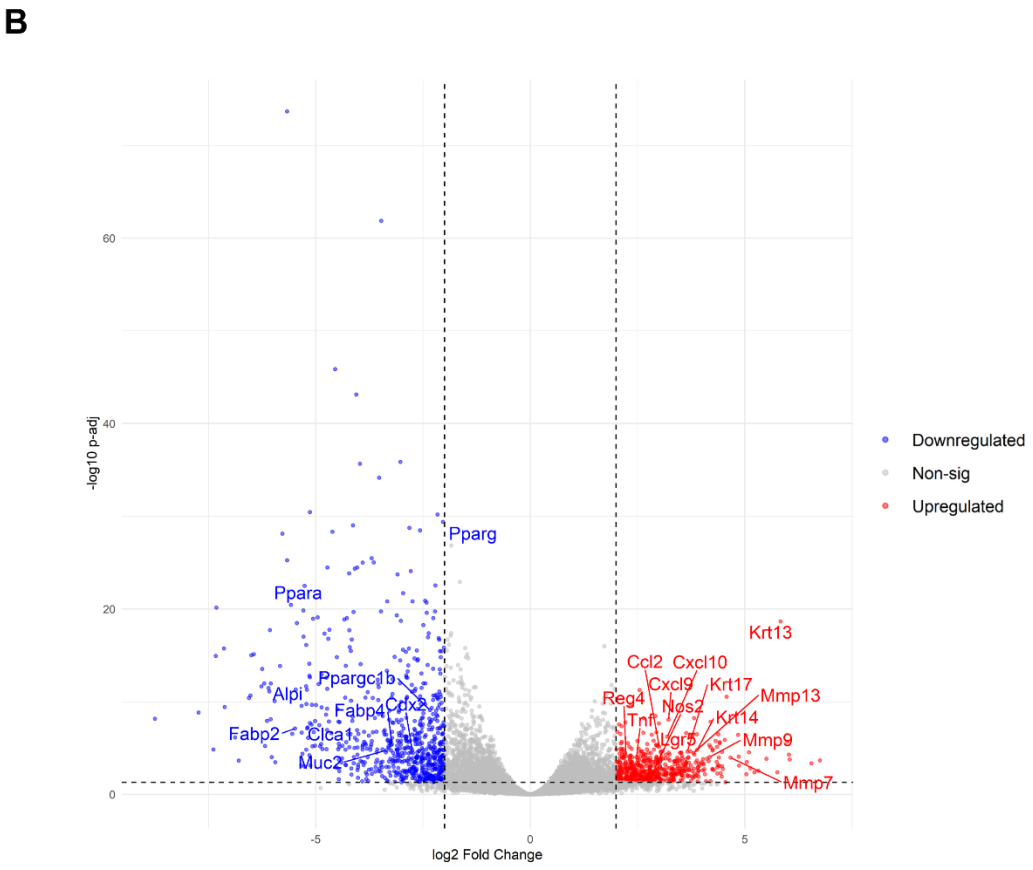
B
60
40
20
0
-log10 p-adj
-5
0
5
log2 Fold Change
Pparg
Ppara
Ppargc1b
Alpi
Fabp4
Cdx2
Fabp2
Clca1
Muc2
Krt13
Ccl2
Cxcl10
Cxcl9
Krt17
Reg4
Nos2
Mmp13
Tnf
Krt14
Lgr5
Mmp9
Mmp7
Downregulated
Non-sig
Upregulated

Figure 20. (A) Reactome pathway enrichment analysis of tumour vs adjacent non-tumoral mucosa in AOM/DSS-treated mice. Gene Set Enrichment Analysis (GSEA) was performed using the Reactome database on a ranked gene list derived from differential gene expression analysis (tumour vs non-tumoral mucosa). The first 20 significantly enriched pathways (adjusted $p < 0.001$) are shown. Each dot represents a Reactome pathway, with the x-axis indicating the normalized enrichment score (NES) and the y-axis listing pathway names. Dot size reflects the gene number count contributing to each pathway, while colour intensity corresponds to statistical significance ($-\log_{10}$ adjusted *p*-value). Pathways are stratified into upregulated (positive NES) and downregulated (negative NES) groups. (B) Volcano plot of differential gene expression in tumour vs adjacent non-tumoral mucosa in the AOM/DSS-treated mice. Genes were filtered based on statistical significance (adjusted $p < 0.05$) and fold change (absolute log2 Fold Change > 2). Significantly upregulated genes are shown in red, downregulated genes in blue, and non-significant genes in grey. Dotted vertical and horizontal lines indicate fold change thresholds and significance cut off, respectively. Selected genes of interest are highlighted.

As mentioned, mRNA-seq data showed that treatment with BMDG compounds did not induce broad transcriptional changes. However, at the macroscopic level, the preventive model was the only condition showing a measurable effect, with a significant reduction in tumour burden and multiplicity in mice treated with free BMDG or BMDG adsorbed on Biochar (data not shown). Focusing on this model to identify more subtle transcriptional alterations between tumour and adjacent non-tumoral mucosa, *Clu* gene was identified of particular interest in the context of colorectal cancer (Figure 21). Recent studies in murine injured epithelium have described a subpopulation of stem cells characterised by high *Clu* expression, which remain largely quiescent under homeostatic conditions but become activated upon injury. Higher *Clu* expression has been reported across different stages of colorectal carcinogenesis and in invasive colorectal adenocarcinomas compared to normal mucosa. Moreover, *Clu* overexpression has been associated with chemoresistance in colorectal cancer patient-derived organoids (Hlavca et al., 2024).

In untreated CRC mice (Figure 21A), *Clu* was significantly upregulated in tumour tissue compared to adjacent non-tumoral mucosa (log2 fold change ≈ 2.8). Notably, in mice treated with BMDG alone (Figure 21B) or BMDG absorbed on Biochar (Figure 21C), *Clu* expression levels in tumour tissue were reduced to levels comparable to non-tumoral mucosa, resulting in a loss of any statistical significance. Of note, the loss of significance is not due to a significant increase in *Clu* gene expression in non-tumoral mucosa (data not shown). In contrast, treatment with BMDG absorbed on Norit-B did not reproduce this effect, as *Clu* expression remained elevated in tumour tissue compared to non-tumoral mucosa (log2 fold change ≈ 3.2), similar to untreated controls. These findings suggest that, despite the absence of widespread transcriptional changes, specific modulation of *Clu* expression may reflect differences in injury-associated stem cell activation and tumour cell plasticity across experimental conditions, although further studies are needed to clarify this relationship.

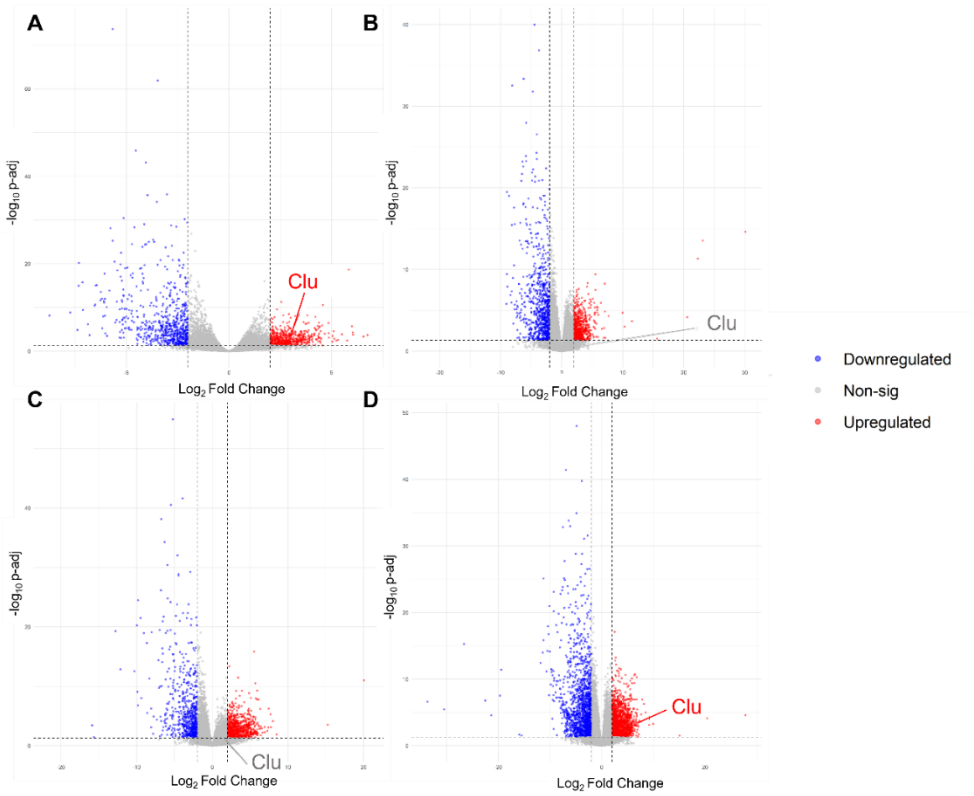

Figure 21. Volcano plot of differential gene expression in tumour vs adjacent non-tumoral mucosa in the AOM/DSS mice treated with BMDG compounds according to the preventive model. Genes were filtered based on statistical significance (adjusted $p < 0.05$) and fold change (absolute log2 Fold Change > 2). Significantly upregulated genes are shown in red, downregulated genes in blue, and non-significant genes in grey. Dotted vertical and horizontal lines indicate fold change thresholds and significance cut off, respectively. *Clu* gene is highlighted. (A) Tumour vs non-tumoral mucosa in untreated control mice. *Clu* gene displayed an adjusted *p*-value of 0.03 and a log2 Fold Change of 2.8. (B) Tumour vs non-tumoral mucosa in mice treated with BMDG alone. No significant differential expression was observed for the *Clu* gene. (C) Tumour vs non-tumoral mucosa in mice treated with BMDG-Biochar. No significant differential expression was observed for the *Clu* gene. (D) Tumour vs non-tumoral mucosa in untreated control mice. *Clu* gene displayed an adjusted *p*-value of 0.01 and a log2 Fold Change of 3.2.

To investigate tumour-adjacent influence on the microenvironment, and its potential role as a target for BMDG compounds, first the transcriptome of peritumoral adipose tissue was analysed and compared with that of abdominal adipose tissue located distally from the tumour. Principal component analysis (Figure 22A) showed that samples clustered primarily along PC1, which accounted for 87% of the total variance, indicating a strong separation driven by tissue origin. Differential gene expression analysis (Figure 22B) further revealed significant transcriptional differences between the two adipose depots. In particular, key markers of adipocyte terminal differentiation, including *Adipoq*, *Plin1* and *Fabp4* genes were downregulated in peritumoral adipose tissue compared to distant abdominal fat. *Adipoq* encodes adiponectin, a protective adipokine produced exclusively by the adipose tissue that plays a key role in positive control of glucose and lipid homeostasis and exerts anti-proliferative, anti-inflammatory and anti-apoptotic effects in physiological conditions (Booth et al., 2015). Similarly, Fabp4 and Perilipin 1 (*Plin1*) are involved in lipid transport and storage, respectively (Genecard.org). These transcriptional changes are consistent with previously described tumour-adipocyte crosstalk (section 1.3.1), whereby cancer cells induce metabolic reprogramming in

adjacent adipocytes. In this context, adipocytes undergo delipidation, reduced cell size, and dedifferentiation-like processes that support tumour progression. Notably, *Clu* upregulation and secretion from tumour cells has been described to induce cachexic fat wasting associated with delipidation and browning of adipose tissue (Liu et al., 2025), supporting our findings. Overall, these findings indicate that peritumoral adipose tissue in this experimental model is transcriptionally influenced by its proximity to the tumour, reflecting a functional interaction between cancer cells and the surrounding adipose microenvironment.

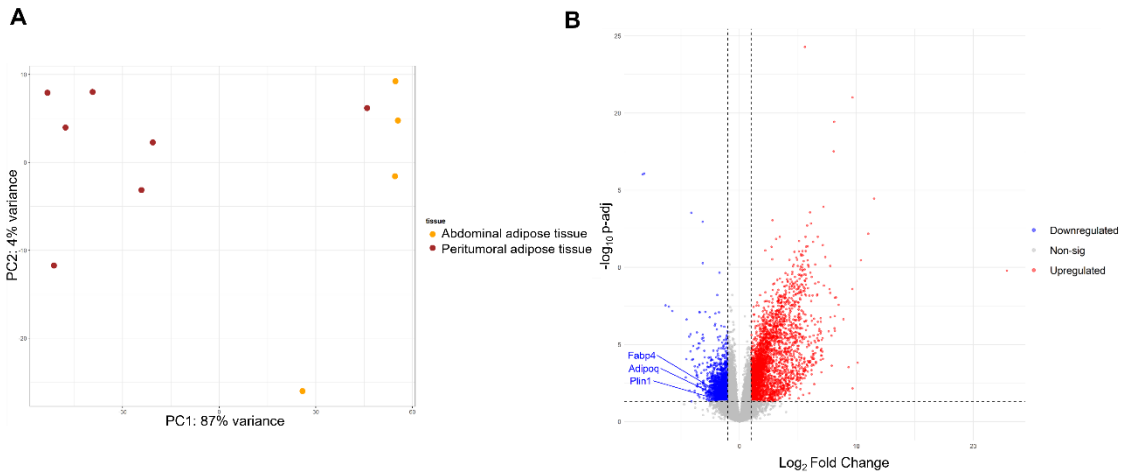

Figure 22. (A) Principal Component Analysis (PCA) of RNA-seq performed on abdominal and peritumoral adipose tissue of AOM/DSS control mice, based on data obtained by applying variance stabilizing transformation (vst) to raw counts using the DESeq2 package. Samples are coloured by tissue type. PC1 and PC2 explain 87% and 4% of the total variance, respectively. Samples cluster primarily according to tissue type. (B) Volcano plot of differential gene expression in peritumoral vs abdominal adipose tissue in the AOM/DSS control mice. Genes were filtered based on statistical significance (adjusted $p < 0.05$) and fold change (absolute log2 Fold Change > 2). Significantly upregulated genes are shown in red, downregulated genes in blue, and non-significant genes in grey. Dotted vertical and horizontal lines indicate fold change thresholds and significance cut off, respectively. Selected genes gene are highlighted.

PCA comparing peritumoral adipose tissue and tumour samples of the preventive treatment model (Figure 23A), confirmed a clear separation between the two tissue types,

with samples clustering distinctly and PC1 explaining 78% of the total variance. This separation supports the absence of tumour tissue contamination during sample collection. Differential gene expression analysis (Figure 23B) further corroborated this distinction, revealing a significant upregulation of canonical adipose tissue markers, including *Adipoq*, *Plin1* and *Lep* in peritumoral adipose tissue compared to tumour samples. In contrast, epithelial markers typically associated with intestinal mucosa, such as *EpCam*, *Muc2*, Keratin family genes (*Krt*), *Vil1*, *Reg4*, *Tff3*, were downregulated in adipose tissue relative to tumour tissue, consistent with the distinct cellular identity of the two compartments (GeneCard.org). Notably, several genes upregulated in adipose tissue, including *Lpl*, *Fasn*, *Lipe*, *Pnpla2*, *Cd36* and *Cebpa* are not strictly adipose-specific but represent key regulators of lipid metabolism and have been implicated in the bidirectional metabolic and signalling crosstalk between tumour cells and the surrounding microenvironment (Grigoraș & Amalinei, 2023; J. Park et al., 2014).

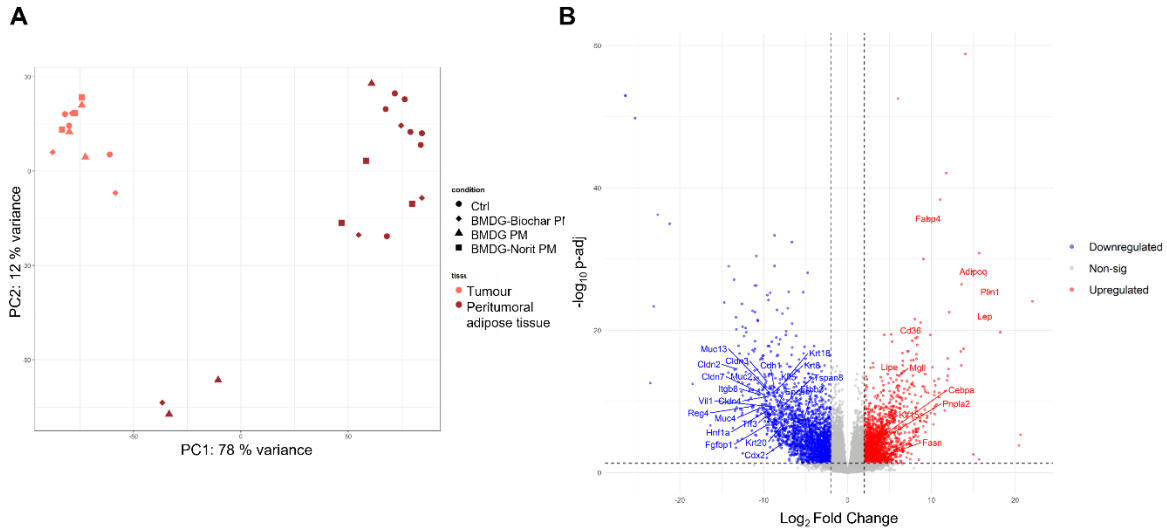

Figure 23. (A) Principal Component Analysis (PCA) of RNA-seq performed on tumour and peritumoral adipose tissue of AOM/DSS mice of the preventive treatment model, based on data obtained by applying variance stabilizing transformation (vst) to raw counts using the DESeq2 package. Samples are coloured by tissue type and shaped by experimental treatment condition. PC1 and PC2 explain 78% and 12% of the total variance, respectively. Samples cluster primarily according to tissue type. The apparent outliers were examined and did not meet the criteria for exclusion. (B) Volcano plot of differential gene expression in

peritumoral adipose tissue vs tumour tissue in the AOM/DSS mice subjected to the preventive model of treatment. Genes were filtered based on statistical significance (adjusted $p < 0.05$) and fold change (absolute log2 Fold Change > 2). Significantly upregulated genes are shown in red, downregulated genes in blue, and non-significant genes in grey. Dotted vertical and horizontal lines indicate fold change thresholds and significance cut off, respectively. Selected genes gene are highlighted.

Finally, the effect of BMDG compounds on the adipose microenvironment was investigated. As shown in Figure 23A, preventive treatment with any of the compounds did not induce major changes at the global transcriptomic level. Therefore, potential subtle transcriptional differences were further explored. Among these, *Fabp2* emerged as a differentially expressed gene of particular interest. Notably, in mice treated with BMDG alone (Figure 24A) or BMDG absorbed on Biochar (Figure 24B), *Fabp2* expression was markedly increased compared to untreated controls, with log2 fold changes of approximately 9.6 and 8.1, respectively. In contrast, treatment with BMDG absorbed on Norit-B (Figure 24C) did not result in a significant modulation of *Fabp2* expression relative to untreated mice, and, overall, did not induce substantial transcriptional changes. *Fabp2* encodes Intestinal Fatty Acid Binding Protein involved in fat absorption and transport specifically in intestinal epithelial cells. In colorectal cancer, *Fabp2* expression has been reported to be reduced in tumour epithelium compared to normal mucosa, suggesting a potential protective and a tumour-suppressive role (P. Wang et al., 2026). Accordingly, in this experimental model, this gene was found significantly downregulated comparing tumour tissue to normal mucosa (log2 fold change ≈ -5.5, Figure 20B) and was not significantly regulated under any treatment condition in tumour tissue samples. Given its intestinal specificity, *Fabp2* was not found to be upregulated in peritumoral adipose tissue compared to tumour tissue, as expected but, remarkably, it was found to be upregulated in the peritumoral adipose tissue of mice treated with BMDG

alone and BMDG adsorbed on Biochar compared to untreated controls (Figure 24 A, B). Of note, when comparing the peritumoral adipose tissue and tumour tissue in treated mice, a statistically significant upregulation of *Fabp2* (adjusted *p*-value = 0.02 and log2 fold change ≈ 6.1) in the BMDG group, and a trend towards upregulation (adjusted *p*-value = 0.15 and log2 fold change ≈ 3.7) in the BMDG-Biochar group were observed, in contrast with the comparison between untreated peritumoral adipose and tumour tissues, where such changes were not observed. No detectable differences were found in the BMDG-Norit group. Although further investigations are required, these data may support the hypothesis of the presence of infiltrating tumour cells within surrounding adipose tissue, characterised by an increased expression of *Fabp2*, potentially driven by treatment-related changes in the adipose microenvironment and in the bidirectional crosstalk.

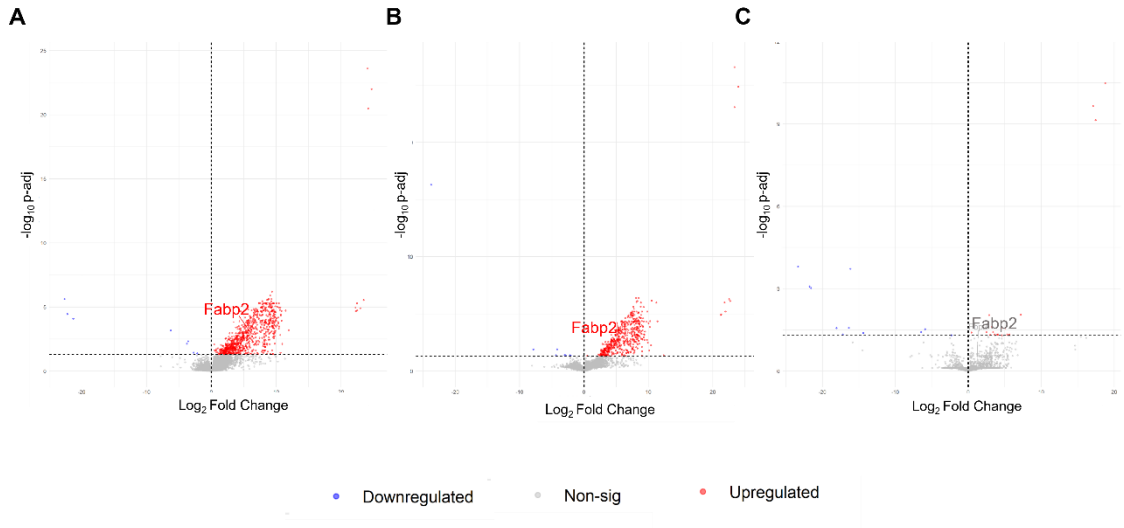

Figure 24. Volcano plot of differential gene expression in peritumoral adipose tissues of AOM/DSS mice treated with BMDG compounds according to the preventive model. Genes were filtered based on statistical significance (adjusted $p < 0.05$) and fold change (absolute log2 Fold Change > 0.05). Significantly upregulated genes are shown in red, downregulated genes in blue, and non-significant genes in grey. Dotted vertical and horizontal lines indicate fold change thresholds and significance cut off, respectively. *Fabp2* gene is highlighted. (A) Peritumoral adipose tissue of AOM/DSS mice treated with BMDG alone. *Fabp2* gene displayed an adjusted *p* -value of 0.0004 and a log2 Fold Change of 9.6. (B) Peritumoral adipose tissue of AOM/DSS mice treated with BMDG-Biochar. *Fabp2* gene displayed an adjusted *p* -value of 0.002 and

a log2 Fold Change of 8.1. (C) Peritumoral adipose tissue of AOM/DSS mice treated with BMDG-Norit. No significant differential expression was observed for the *Fabp2* gene.

5. Discussion

Colorectal cancer, the third most common cancer worldwide in terms of both incidence and mortality, represents a growing global health concern, particularly due to the increasing burden of early-onset cases in young adults (Akimoto et al., 2021; Cancer (IARC), s.d.; Siegel et al., 2026). Given the well-established role of gut microbiota dysbiosis in CRC development, along with the anti-tumoral properties of short-chain fatty acids - especially butyrate (Bordonaro, 2025; McNabney & Henagan, 2017b; Yoon & Kim, 2018) - several compounds aiming at enhancing SCFA-producing bacteria and restoring butyrate levels in patients with CRC have been constantly explored for both therapeutic and prevention purposes (Gomes et al., 2023; Kvakova et al., 2022). Notably, oral butyrate supplementation has shown potential in inhibiting CRC progression (Alvandi et al., 2022; Hodgkinson et al., 2023).

In this context, by adopting multiple *in vitro* models of colorectal cancer, the present study provides the first evidence of the direct inhibitory effect exerted by a novel, well-defined butyrate formulation absorbed on a tailored biochar. Furthermore, considering the supportive role of the tumour microenvironment and the dynamic crosstalk between adipocytes and infiltrating cancer cells (Olszańska et al., 2023; J. Park et al., 2014; Tabuso et al., 2017), this work also offers insight into the *in vivo* impact of this green compound on the transcriptomic profiles of both tumour tissue and surrounding adipose microenvironment.

The novelty of this formulation consists in the use of tailor-made biochar from alder wood feedstock with a specific meso-porosity that optimises the absorption and the release of a mixture of butyrate glycerides. This bioactive molecule, already used in animal nutrition

to promote eubiosis (Rimoldi et al., 2018; Yang et al., 2018), enables a colon-targeted delivery strategy: glycerol esterification allows butyrate to be released in the lower gastrointestinal tract through the action of intestinal lipases, thereby limiting its absorption in the upper digestive tract (Rimoldi et al., 2018). To date, only a few published studies have explored biochar as a delivery carrier, mainly in the context of silver nanoparticles, where it has been shown to enhance antiproliferative, antiangiogenic, and anti-inflammatory effects in lung (Abu Hajleh et al., 2023) and colon (Alqaraleh et al., 2023) cancer. Therefore, the present study investigates the anti-cancer properties of butyrate in the form of mono- and di- glycerides (BMDG), either alone or absorbed on tailor-made, mesoporous Biochar or microporous activated carbon (Norit-B).

The distinct porous structures of these carriers appeared to be critical: the meso- and macro- porosity of Biochar, determined by controlled pyrolysis of alder chips, enhanced both absorption and release of BMDG compared to the microporous structure of the steam-activated Norit-B, more prone to absorption than release (Ahuja & Pathak, 2009; Solano-Umaña & Vega-Baudrit, 2015; Zhao et al., 2017; Zhu et al., 2018). Moreover, Norit-B showed a greater ability to absorb glucose.

Functionally, as previously described for butyrate (McNabney & Henagan, 2017), which exerts a selective inhibition of cell proliferation on colon cancer cells and conversely a trophic stimulatory effect on normal colonocytes, BMDG demonstrated a marked antiproliferative effect in CRC cell lines, inhibiting DNA replication of around 50% at 24 hours with a similar effect on both HT29 and HCT116 cells, which started to be more evident in the latter at longer incubation. The difference observed in the extent of the response may be ascribed to the less aggressive phenotype of HT29, which are more differentiated than HCT116 cells, thus more comparable to the differentiated normal

colonocytes. When BMDG was carried by Biochar, the difference in the inhibitory effect between the two cell types was even amplified, suggesting an additional effect of Biochar that seemed to be specific for the more aggressive line. Specifically, among the two cell lines tested, HCT116 cells were more sensitive than HT29 cells, showing approximately 62% inhibition compared to 41% when treated with BMDG-Biochar. The specificity of the incremental inhibitory effect associated with Biochar as carrier, was supported by the absence of any effect when BMDG was absorbed on Norit-B or when Biochar was administered alone, further supporting the specificity and efficacy of the combined green formulation. The butyrate glyceride mixture appeared to require direct interaction between Biochar and HCT116 cells to achieve enhanced inhibition of cell proliferation and this was supported by experiments using media enriched with released BMDG but depleted of carbon, which showed reduced efficacy. Conversely, Norit-B administered alone was associated with a stimulation of thymidine uptake. This paradoxical effect on proliferation, which was specific for the free activated-carbon and was mitigated when Norit-B absorbed BMDG, might be explained by the ability of the specific micro-porosity of activate carbon to absorb small molecules such as glucose, likely including tritiated thymidine, potentially resulting in contamination of the liquid scintillator by residual, unwashed Norit-B. It would be interesting to further assess whether activated carbons maintain the ability to absorb small molecules other than glucose.

In AKPS mouse colon organoids, which better recapitulate the epithelial complexity and the *in vivo* multi-hit nature of CRC, higher doses of BMDG were required to achieve maximal effects. Nevertheless, the antiproliferative activity was even more pronounced than in the cell lines, reaching approximately 92%, 90%, and 32% inhibition for BMDG alone, BMDG-biochar, and BMDG-Norit, respectively. Notably, a significant reduction in organoids area was observed only with BMDG absorbed on Biochar. Overall, these

findings highlight the superior ability of Biochar to enhance the biological activity of BMDG. Importantly, the observed inhibitory effects appeared to be selective for CRC models, with no detectable impact on the proliferation or viability of non-tumoral colon epithelial cells.

Surprisingly, as revealed by TEM analysis, CRC cells can actively internalise both Biochar and Norit-B carbon particles, resulting in morphology deformation associated with slight signs of differentiation, particularly evident for the more undifferentiated HCT116 cells, and characterised by the appearance of some microvilli, reminiscent of the normal colonic surface epithelium. Cell internalisation of Biochar or Norit-B particles did not seem to be responsible for cell death, as the cells that had included char particles did not show any morphological sign of injury. Conversely, TEM images showed some cells with protruding lamellipodia to engulf the carbon particles into large lysosomes. AKPS organoids, embedded in basement membrane extract, did not internalise char particles, yet still exhibited moderate signs of differentiation, accompanied by slight depolarization. In contrast to what was observed in cell lines, mitochondria of untreated organoids show features of dysfunction, which are less evident following treatment with BMDG-Biochar. Similar to HT29 cells, organoids displayed an increase in lipid droplet content in the presence of free BMDG and BMDG-Norit; however, it is reasonable to hypothesise that this accumulation reflected enhanced lipogenesis and triglyceride storage, probably as a consequence of mitochondrial dysfunction. Several studies have demonstrated that mitochondrial impairment - resulting in increased ROS production - and the accumulation of lipid droplets, which serve as an energy source for highly malignant cancer cells, both contribute to cancer progression (H. Du et al., 2025; Nisticò & Chiarella, 2023). Based

on TEM qualitative observations, BMDG-Biochar appeared as the only treatment able to mitigate mitochondrial dysfunction signs and lipid droplets accumulation.

Considering these ultrastructural observations, and given that the rapid proliferation of cancer cells depends on metabolic reprogramming, cell metabolism was investigated to better understand the tumour-specific antiproliferative effect observed with BMDG compounds. The metabolic profiling performed using Seahorse technology provided important insights into the differential sensitivity of cancer and normal models to BMDG-based treatments, highlighting a strong link between metabolic phenotype and drug response. Basal characterisation of cell lines, confirmed that HCT116 cells exhibit a more metabolically active phenotype compared to HT29 and HCEC-1CT, observation consistent with their higher responsiveness to metabolic challenge and their predominantly glycolytic metabolism that ensures a metabolic flexibility and high energy production. The ability of cancer cells to dynamically switch between oxidative phosphorylation and glycolysis is widely recognized as a key driver of tumour progression and drug resistance. Consequently, there is growing interest in therapeutic strategies that target both mitochondrial function and glycolytic pathways as promising approaches in cancer treatment (Dong & Neuzil, 2019). In this context, free BMDG was more effective at inhibiting respiratory parameters, including ATP production, in HT29 cells, more dependent on mitochondrial respiration. However, BMDG effect was attenuated upon absorption on carbon carriers - particularly on Biochar compared to Norit-B - while becoming more pronounced in HCT116 cells. These findings suggest that the formulation of BMDG compound critically influences its bioavailability and intracellular activity, potentially due to differences in cellular uptake, release kinetics, and/or the specific metabolic phenotype of the target cells. This was more evident if

considering normal epithelial colon cell lines, which not only showed to be resistant to mitochondrial impairment by BMDG, but also displayed an increased mitochondrial activity in the presence of BMDG-Biochar, further supporting the tumour-specific inhibitory action of BMDG compounds. The ATP rate assay further clarified the distinct metabolic adaptations of the tumour cell lines. In HT29 cells, mitochondrial impairment appeared to promote a compensatory shift toward glycolysis under all treatment conditions, despite the fact that only free BMDG significantly affected mitochondrial respiration parameters. In contrast, in HCT116 cells, all BMDG compounds interfered with the glycolytic component of cellular metabolism, with BMDG-Biochar exerting the strongest inhibitory effect. This indicates an inability to compensate for energetic stress, resulting in a shift toward a more quiescent, less energetically active - less glycolytic - phenotype. These data suggest the potential use of BMDG targeting specifically CRC aggressive phenotypes characterised by a high Warburg condition, supporting not only ATP production but also providing intermediates for biosynthetic pathways essential for proliferation.

The AKPS organoid model, with its particular pathophysiological relevance, represents a more complex and physiologically representative system than conventional CRC cell lines, and was inherently more challenging to investigate at the metabolic level. Organoid treatment with free BMDG or BMDG absorbed on Biochar did not fully recapitulate the mitochondrial alterations observed in cell lines. These discrepancies can be explained by a resistance in terms of mitochondrial functionality in the organoid model, though difference in the drug concentrations and in the experimental protocols required by the complexity of the model, may also play a role. A different scenario emerged when considering total ATP production in organoids, which was reduced by both BMDG-

Biochar and BMDG-Norit, indicating that these treatments effectively impair cellular energetics. Notably, the ATP rate assay performed using Seahorse technology confirmed that glycolysis remains a primary target of BMDG, particularly when absorbed on carbon carriers and most prominently in the case of Biochar. Notably, results obtained with Norit-B require careful interpretation, as its intrinsic capacity to absorb small molecules - such as glucose - may independently influence cellular metabolism, potentially confounding the effects attributed to BMDG absorption.

Overall, these data demonstrate that the metabolic effects of BMDG are highly dependent on the cellular context, metabolic vulnerability and the formulation of the compounds. BMDG absorbed on Biochar appears particularly effective in targeting glycolysis in highly glycolytic models such as HCT116 cells and AKPS organoids, likely contributing significantly to the stronger antiproliferative effects observed with BMDG-Biochar compounds in these two *in vitro* models of CRC. The additional inhibitory effect exerted by Biochar in HCT116 and AKPS, might be explained by a direct effect of the char particles and not only by their activity as BMDG carrier. For instance, it might be associated with the alkaline pH characteristic of Biochar compared to the slightly acid values characterising Norit-B, therefore potentially interfering with the acidic tumour microenvironment, which is mainly due to the massive tumour production of lactate derived by the glycolytic metabolism. Neutralization of the extracellular acid pH of the tumour microenvironment has recently been highlighted as a potential anti-cancer strategy (Rahman et al., 2024). Results obtained with HCT116 and AKPS are in line with previous studies demonstrating that butyrate can inhibit the Warburg effect. In particular, metabolic remodelling has been associated with activation of pyruvate kinase M2 (PKM2) and downregulation of key glycolytic enzymes such as GLUT1 and glucose-6-

phosphate dehydrogenase (G6PD) (Geng et al., 2021; Q. Li et al., 2018). However, the mechanisms by which butyrate differentially modulates metabolic pathways across CRC models remain incompletely understood. Indeed, in HT29 cells, despite a reduction in proliferation, the present study reveals a paradoxical increased glycolytic contribution to total ATP production under all treatment conditions, suggesting a distinct adaptive response. Moreover, in HCT116 cells - but not in AKPS organoids, where a stronger antiproliferative effect was observed - a combined inhibition of both glycolytic and mitochondrial metabolism was detected, particularly with BMDG-Biochar. These findings support the hypothesis that not only the drug responsiveness but even the underlying mechanisms can vary significantly across CRC models, and that BMDG activity is not restricted to glycolytic inhibition. It would be of particular interest to investigate whether the mutational profile may contribute to the observed differences. Indeed, HT29 cells exhibit an enterocyte-like mucinous phenotype and harbour mutations in *Apc, Braf*^{V600E}*, Trp53, PIK3CA, Smad4,* along with microsatellite stability (MSS) status. In contrast, HCT116 cells display an undifferentiated, mesenchymal-like phenotype with microsatellite instability (MSI), and carry mutations in *Kras*^{G13D}, *PIK3CA, CTNNB1* and *Tgfbr2* mutations. The mutational profile of HT29 is typically associated with chemotherapy resistance and poor prognosis, whereas the MSI status of HCT116 is linked to improved responsiveness to immunotherapy but resistance to EGFR-targeted therapies (Al-Kabani et al., 2025). In light of the dual metabolic effect of BMDG-Biochar specifically observed in HCT116 cells, resulting in a strong antiproliferative response, its potential use as an adjuvant in immunotherapy for MSI-high CRC - representing approximately 15% of sporadic colorectal cancers (Harada & Morlote, 2020) - deserves further investigation. The selective action on tumoral cells further supports the therapeutic potential of this novel combined compound.

The project that included this thesis work aimed to evaluate BMDG compounds also in an *in vivo* mouse model of inflammation-driven CRC tumorigenesis. Two treatment strategies were applied - preventive and therapeutic - using BMDG either in free form or absorbed on Biochar or Norit-B to test the ability of chars to carry the mixture in a physiological context. In this scenario, a key objective of this thesis was to investigate whether BMDG compounds could modulate transcriptional programs not only within the tumour tissue, but also in the adjacent and distal compartments, with particular attention to the adipose microenvironment. At the global level, mRNA-seq analyses revealed that tissue identity represents the dominant driver of gene expression variability in both preventive and therapeutic settings, with no clear clustering based on treatment, indicating that BMDG compounds do not induce large-scale transcriptional changes, but rather exert more subtle effects**.** Comparison between tumour tissue and adjacent non-tumoral mucosa in untreated AOM/DSS mice confirmed a tumour-associated transcriptional signature, characterised by enhanced proliferation, inflammation, tissue remodelling, and epithelial plasticity and suppression of metabolic pathways, particularly those related to mitochondrial respiration, and downregulation of genes involved in lipid metabolism and epithelial differentiation. Of note, *Pparγ* was downregulated in tumour tissue compared to non-tumoral mucosa in this model, supporting its proposed tumour-suppressive role - long debated in the literature - and highlighting its potential as a promising therapeutic target. These findings support the efficacy of the AOM/DSS model to induce tumour nodules and that, despite the global chronic inflammation, it was possible to recognise and distinguish a tumour-specific expression profile from a chronic inflammation-associated signature. Within this context, one of the most interesting findings emerging from the preventive model concerned the modulation of *Clu* (Clusterin) expression. In untreated tumour bearing mice, *Clu* was significantly

upregulated in tumour tissue, consistent with its association with injury-responsive stem cell populations and tumour progression. Treatment with free BMDG or BMDG-Biochar normalised *Clu* expression levels in tumour tissue, abolishing its differential expression relative to non-tumoral mucosa. Given the reported role of *Clu* in epithelial regeneration, tumour plasticity, and chemoresistance (Hlavca et al., 2024), its modulation may reflect a reduction in injury-associated stemness, potentially contributing to the reduced tumour burden observed *in vivo* (data not included in this thesis) and highlighting the potential preventive action of BMDG. Beyond the tumour compartment, this study aimed to provide evidence of BMDG treatments on functional crosstalk between tumour cells and the surrounding adipose tissue. Also within the AOM/DSS scenario it was possible to observe a distinct transcriptional profile between peritumoral adipose tissue and distal abdominal tissue, supporting the suitability of this system as a reliable model in which investigate the modulation apported by BMDG compounds to adipose microenvironment. Indeed, a downregulation of key adipocyte differentiation markers such as *Adipoq*, *Plin1*, and *Fabp4* was observed, consistent with the dedifferentiated, metabolically reprogrammed adipocyte phenotype described in tumour-associated adipose tissue, contributing to tumour progression through lipid mobilization and paracrine signalling (J. Park et al., 2014). Adipose tissue identity appeared preserved in comparison to tumour tissue, with adipose-specific and epithelial markers expressed accordingly. Importantly, treatment with BMDG compounds did not induce major transcriptomic shifts in adipose tissue, mirroring observations in tumour samples. Focusing on specific and subtle changes, *Fabp2* gene expression in peritumoral adipose tissue, represented a particularly intriguing finding. *Fabp2* is typically restricted to intestinal epithelial cells and is associated with fatty acid absorption. Lower expression levels of *Fabp2* are associated with tumour epithelium, compared to normal mucosa, suggesting a tumour suppressor

role (P. Wang et al., 2026). The upregulation of *Fabp2* exclusively in peritumoral adipose tissue following treatment with free BMDG and BMDG-Biochar likely reflects the presence of tumour cells infiltrating the adipose tissue, exhibiting higher *Fabp2* expression in response to BMDG compounds, suggesting treatment-related modulation supported by the adipose microenvironment and the bidirectional tumour-adipose crosstalk.

Taken together, these findings highlight that BMDG compounds do not influence the global transcriptome either in the tumour and in the adipose microenvironment, but could be relevant for specific molecular targets. Their activity appears to be highly dependent on formulation, consistent with *in vitro* observations, with Biochar emerging as a more effective carrier compared to Norit-B. Importantly, these results warrant further investigation into the effects of treatment on the adipose microenvironment, both as a target and as a mediator of therapeutic response.

6. Conclusions and future prospective

In conclusion, these findings suggest that through controlled pyrolysis starting from well-selected wood stocks, reactor type and thermochemical process conditions, it is possible to produce Biochar with specific tailor-made properties. This green product can be used as a carrier that potentiates the inhibitory effects of a defined mixture of different butyrate glyceride compounds, with a promising potential use especially in aggressive, undifferentiated CRC phenotypes. Further studies are required to elucidate the cellular mechanisms underlying these effects and to assess their translational potential. In addition, the intrinsic biological activity of Biochar - particularly its role as a pH modulator beyond its function as a carrier - warrants deeper investigation.

BMDG compounds exerted selective effects *in vivo*, modulating specific molecular targets, rather than inducing broad transcriptomic reprogramming. In particular, a potential role of BMDG in interfering with tumour cell plasticity and tumour-adipose crosstalk is highlighted in a preventive setting, with Biochar emerging as the most effective delivery system. Future studies should focus on elucidating the cellular mechanisms underlying these effects, including the role of microenvironment to treatment response. Although the results are generally consistent across the different CRC models used in this thesis, the reduced efficacy observed in the most complex *in vivo* model requires further clarification. In particular, the differences between the preventive and curative settings warrant optimization of the experimental conditions. This may help to determine whether the dose administered in both settings was adequate and the timing of pre-treatment in the preventive context was optimal to elicit a therapeutic effect, or whether these factors do not significantly influence treatment efficacy.

Biochar as a natural carrier, might be investigated to be used as an adjuvant in CRC therapy as well as in a preventive setting to limit tumour progression.

7. References

Aarons, C. B., Shanmugan, S., & Bleier, J. I. S. (2014). Management of malignant colon polyps: Current status and controversies. *World Journal of Gastroenterology*, *20*(43), 16178–16183. https://doi.org/10.3748/wjg.v20.i43.16178

Abu Hajleh, M. N., Al-limoun, M., Al-Tarawneh, A., Hijazin, T. J., Alqaraleh, M., Khleifat, K., Al-Madanat, O. Y., Qaisi, Y. A., AlSarayreh, A., Al-Samydai, A., Qaralleh, H., & Al-Dujaili, E. A. S. (2023). Synergistic Effects of AgNPs and Biochar: A Potential Combination for Combating Lung Cancer and Pathogenic Bacteria. *Molecules*, *28*(12), Articolo 12. https://doi.org/10.3390/molecules28124757

Agrawal, N., Lanjhiyana, S. K., Jaiswal, M., Siddiqui, M. A., & Gupta, S. (2025). Colorectal cancer spectrum: From subtypes and epidemiology to oncotherapies. *Gastroenterology & Endoscopy*, *3*(2), 55–64. https://doi.org/10.1016/j.gande.2025.01.002

Ahadi, M., Sokolova, A., Brown, I., Chou, A., & Gill, A. J. (2021). The 2019 World Health Organization Classification of appendiceal, colorectal and anal canal tumours: An update and critical assessment. *Pathology*, *53*(4), 454–461. https://doi.org/10.1016/j.pathol.2020.10.010

Ahmed, D., Eide, P. W., Eilertsen, I. A., Danielsen, S. A., Eknæs, M., Hektoen, M., Lind, G. E., & Lothe, R. A. (2013). Epigenetic and genetic features of 24 colon cancer cell lines. *Oncogenesis*, *2*(9), e71–e71. https://doi.org/10.1038/oncsis.2013.35

Ahuja, G., & Pathak, K. (2009). Porous carriers for controlled/modulated drug delivery. *Indian Journal of Pharmaceutical Sciences*, *71*(6), 599–607. https://doi.org/10.4103/0250-474X.59540

Aiderus, A., Barker, N., & Tergaonkar, V. (2024). Serrated colorectal cancer: Preclinical models and molecular pathways. *Trends in Cancer*, *10*(1), 76–91. https://doi.org/10.1016/j.trecan.2023.09.011

Akimoto, N., Ugai, T., Zhong, R., Hamada, T., Fujiyoshi, K., Giannakis, M., Wu, K., Cao, Y., Ng, K., & Ogino, S. (2021). Rising incidence of early-onset colorectal cancer—A call to action. *Nature Reviews Clinical Oncology*, *18*(4), 230–243. https://doi.org/10.1038/s41571-020-00445-1

Al-Kabani, A., Huda, B., Haddad, J., Yousuf, M., Bhurka, F., Ajaz, F., Patnaik, R., Jannati, S., & Banerjee, Y. (2025). Exploring Experimental Models of Colorectal Cancer: A Critical Appraisal from 2D Cell Systems to Organoids, Humanized Mouse Avatars, Organ-on-Chip, CRISPR Engineering, and AI-Driven Platforms—Challenges and Opportunities for Translational Precision Oncology. *Cancers*, *17*(13), 2163. https://doi.org/10.3390/cancers17132163

Alqaraleh, M., Khleifat, K. M., Abu Hajleh, M. N., Farah, H. S., & Ahmed, K. A.-A. (2023). Fungal-Mediated Silver Nanoparticle and Biochar Synergy against Colorectal Cancer Cells and Pathogenic Bacteria. *Antibiotics*, *12*(3), Articolo 3. https://doi.org/10.3390/antibiotics12030597

Alvandi, E., Wong, W. K. M., Joglekar, M. V., Spring, K. J., & Hardikar, A. A. (2022). Short-chain fatty acid concentrations in the incidence and risk-stratification of colorectal cancer: A systematic review and meta-analysis. *BMC Medicine*, *20*(1), 323. https://doi.org/10.1186/s12916-022-02529-4

Alzahrani, S., Al Doghaither, H., & Al-Ghafari, A. (2021). General insight into cancer: An overview of colorectal cancer (Review). *Molecular and Clinical Oncology*, *15*(6), 271. https://doi.org/10.3892/mco.2021.2433

Arneth, B. (2019). Tumor Microenvironment. *Medicina*, *56*(1), 15. https://doi.org/10.3390/medicina56010015

Baglioni, S., Cantini, G., Poli, G., Francalanci, M., Squecco, R., Franco, A. D., Borgogni, E., Frontera, S., Nesi, G., Liotta, F., Lucchese, M., Perigli, G., Francini, F., Forti, G., Serio, M., & Luconi, M. (2012). Functional Differences in Visceral and Subcutaneous Fat Pads Originate from Differences in the Adipose Stem Cell. *PLOS ONE*, *7*(5), e36569. https://doi.org/10.1371/journal.pone.0036569

Barker, N., Ridgway, R. A., van Es, J. H., van de Wetering, M., Begthel, H., van den Born, M., Danenberg, E., Clarke, A. R., Sansom, O. J., & Clevers, H. (2009). Crypt stem cells as the cells-of-origin of intestinal cancer. *Nature*, *457*(7229), 608–611. https://doi.org/10.1038/nature07602

Benedix, F., Kube, R., Meyer, F., Schmidt, U., Gastinger, I., Lippert, H., & Group, the C. C. (Primary T. S. (2010). Comparison of 17,641 Patients With Right- and Left-Sided Colon Cancer: Differences in Epidemiology, Perioperative Course, Histology, and Survival. *Diseases of the Colon & Rectum*, *53*(1), 57. https://doi.org/10.1007/DCR.0b013e3181c703a4

Betzler, A. M., Nanduri, L. K., Hissa, B., Blickensdörfer, L., Muders, M. H., Roy, J., Jesinghaus, M., Steiger, K., Weichert, W., Kloor, M., Klink, B., Schroeder, M., Mazzone, M., Weitz, J., Reissfelder, C., Rahbari, N. N., & Schölch, S. (2021). Differential Effects of Trp53 Alterations in Murine Colorectal Cancer. *Cancers*, *13*(4), 808. https://doi.org/10.3390/cancers13040808

Bhatia, A., Shatanof, R. A., & Bordoni, B. (2025). Embryology, Gastrointestinal. In *StatPearls*. StatPearls Publishing. http://www.ncbi.nlm.nih.gov/books/NBK537172/

Birbrair, A. (A c. Di). (2020). *Tumor Microenvironments in Organs: From the Brain to the Skin – Part A* (Vol. 1226). Springer International Publishing. https://doi.org/10.1007/978-3-030-36214-0

Bird, R. P. (1987). Observation and quantification of aberrant crypts in the murine colon treated with a colon carcinogen: Preliminary findings. *Cancer Letters*, *37*(2), 147–151. https://doi.org/10.1016/0304-3835(87)90157-1

Bird, R. P. (1995). Role of aberrant crypt foci in understanding the pathogenesis of colon cancer. *Cancer Letters*, *93*(1), 55–71. https://doi.org/10.1016/0304-3835(95)03788-X

Blachier, F., de Sá Resende, A., da Silva Fogaça Leite, G., Vasques da Costa, A., & Lancha Junior, A. H. (2018). Colon epithelial cells luminal environment and physiopathological consequences: Impact of nutrition and exercise. *Nutrire*, *43*(1), 2. https://doi.org/10.1186/s41110-018-0061-6

Booth, A., Magnuson, A., Fouts, J., & Foster, M. (2015). Adipose tissue, obesity and adipokines: Role in cancer promotion. *Hormone Molecular Biology and Clinical Investigation*, *21*(1), 57–74. https://doi.org/10.1515/hmbci-2014-0037

Bordonaro, M. (2025). A Model of Butyrate Activity and Resistance in CRC. *Journal of Cellular and Molecular Medicine*, *29*(11), e70656. https://doi.org/10.1111/jcmm.70656

Breton, L. A., Mahdi, Z., Pratt, C., & Hanandeh, A. E. (2021). Modification of Hardwood Derived Biochar to Improve Phosphorus Adsorption. *Environments*, *8*(5). https://doi.org/10.3390/environments8050041

Bürtin, F., Mullins, C. S., & Linnebacher, M. (2020). Mouse models of colorectal cancer: Past, present and future perspectives. *World Journal of Gastroenterology*, *26*(13), 1394–1426. https://doi.org/10.3748/wjg.v26.i13.1394

Cancer (IARC), T. I. A. for R. on. (s.d.). *Global Cancer Observatory*. Recuperato 7 febbraio 2026, da https://gco.iarc.fr/

Cantini, G., Trabucco, M., Franco, A. D., Mannucci, E., & Luconi, M. (2019). Glucagon modulates proliferation and differentiation of human adipose precursors. *Journal of Molecular Endocrinology*, *63*(4), 249–260. https://doi.org/10.1530/JME-19-0095

Carethers, J. M. (2021). Racial and ethnic disparities in colorectal cancer incidence and mortality. *Advances in Cancer Research*, *151*, 197–229. https://doi.org/10.1016/bs.acr.2021.02.007

Casini, D., Barsali, T., Rizzo, A. M., & Chiaramonti, D. (2021). Production and characterization of co-composted biochar and digestate from biomass anaerobic digestion. *Biomass Conversion and Biorefinery*, *11*(6), 2271–2279. https://doi.org/10.1007/s13399-019-00482-6

Chen, C., Su, Q., Zi, M., Hua, X., & Zhang, Z. (2025). Harnessing gut microbiota for colorectal cancer therapy: From clinical insights to therapeutic innovations. *Npj Biofilms and Microbiomes*, *11*(1), 190. https://doi.org/10.1038/s41522-025-00818-3

Chen, F., Zhuang, X., Lin, L., Yu, P., Wang, Y., Shi, Y., Hu, G., & Sun, Y. (2015). New horizons in tumor microenvironment biology: Challenges and opportunities. *BMC Medicine*, *13*(1), 45. https://doi.org/10.1186/s12916-015-0278-7

Chen, H., Lei, Y., Zhou, J., Lv, C., & Xuan, Q. (2025). Advances in bevacizumab in colorectal cancer: A bibliometric analysis from 2004 to 2023. *Frontiers in Oncology*, *15*, 1552914. https://doi.org/10.3389/fonc.2025.1552914

Cheng, L. K., O'Grady, G., Du, P., Egbuji, J. U., Windsor, J. A., & Pullan, A. J. (2010). Gastrointestinal system. *Wiley interdisciplinary reviews. Systems biology and medicine*, *2*(1), 65–79. https://doi.org/10.1002/wsbm.19

Chowdhury, S., Hofree, M., Lin, K., Maru, D., Kopetz, S., & Shen, J. P. (2021). Implications of Intratumor Heterogeneity on Consensus Molecular Subtype (CMS) in Colorectal Cancer. *Cancers*, *13*(19), 4923. https://doi.org/10.3390/cancers13194923

Colombo, A., & Porretto, C. M. (2023). Anti-vascular endothelial growth factor receptor in colorectal cancer: A review. *International Journal of Gastrointestinal Intervention*, *12*(3), 110–114. https://doi.org/10.18528/ijgii230011

De Robertis, M., Massi, E., Poeta, M. L., Carotti, S., Morini, S., Cecchetelli, L., Signori, E., & Fazio, V. M. (2011). The AOM/DSS murine model for the study of colon carcinogenesis: From pathways to diagnosis and therapy studies. *Journal of Carcinogenesis*, *10*, 9. https://doi.org/10.4103/1477-3163.78279

Dhillon, A. S., Hagan, S., Rath, O., & Kolch, W. (2007). MAP kinase signalling pathways in cancer. *Oncogene*, *26*(22), 3279–3290. https://doi.org/10.1038/sj.onc.1210421

Dong, L., & Neuzil, J. (2019). Targeting mitochondria as an anticancer strategy. *Cancer Communications*, *39*, 63. https://doi.org/10.1186/s40880-019-0412-6

Drost, J., van Jaarsveld, R. H., Ponsioen, B., Zimberlin, C., van Boxtel, R., Buijs, A., Sachs, N., Overmeer, R. M., Offerhaus, G. J., Begthel, H., Korving, J., van de Wetering, M., Schwank, G., Logtenberg, M., Cuppen, E., Snippert, H. J., Medema, J. P., Kops, G. J. P. L., & Clevers, H. (2015). Sequential cancer mutations in cultured human intestinal stem cells. *Nature*, *521*(7550), 43–47. https://doi.org/10.1038/nature14415

Du, H., Xu, T., Yu, S., Wu, S., & Zhang, J. (2025). Mitochondrial metabolism and cancer therapeutic innovation. *Signal Transduction and Targeted Therapy*, *10*(1), 245. https://doi.org/10.1038/s41392-025-02311-x

Du, Y., Tang, G., & Yuan, W. (2020). Suppression of HDAC2 by sodium butyrate alleviates apoptosis of kidney cells in db/db mice and HG-induced NRK-52E cells. *International Journal of Molecular Medicine*, *45*(1), 210–222. https://doi.org/10.3892/ijmm.2019.4397

Duong, M. N., Geneste, A., Fallone, F., Li, X., Dumontet, C., & Muller, C. (2017). The fat and the bad: Mature adipocytes, key actors in tumor progression and resistance. *Oncotarget*, *8*(34), 57622–57641. https://doi.org/10.18632/oncotarget.18038

Elnour, A. Y., Alghyamah, A. A., Shaikh, H. M., Poulose, A. M., Al-Zahrani, S. M., Anis, A., & Al-Wabel, M. I. (2019). Effect of Pyrolysis Temperature on Biochar Microstructural Evolution, Physicochemical Characteristics, and Its Influence on Biochar/Polypropylene Composites. *Applied Sciences*, *9*(6), Articolo 6. https://doi.org/10.3390/app9061149

Eroglu, S., Birsenogul, I., Bowen, A. P., Doyle, J. F., Pupkin, S. E., Villar, J., Tarney, C. M., Gandia, E., Pastor, D. M., & Estrada-Veras, J. I. (2025). Lynch Syndrome in Focus: A Multidisciplinary Review of Cancer Risk, Clinical Management, and Special Populations. *Cancers*, *17*(24), 3981. https://doi.org/10.3390/cancers17243981

Esposito, A., Agostini, A., Quero, G., Piro, G., Priori, L., Caggiano, A., Scaglione, G., Battaglia, A., Calegari, M. A., Salvatore, L., Bensi, M., Maratta, M. G., Ceccarelli, A., Trovato, G., Genovese, G., Gurreri, E., Ascrizzi, S., Martini, M., Fiorillo, C., … Carbone, C. (2024). Colorectal cancer patients-derived immunity-organoid platform unveils cancer-specific tissue markers associated with immunotherapy resistance. *Cell Death & Disease*, *15*(12), 878. https://doi.org/10.1038/s41419-024-07266-5

Ewels, P. A., Peltzer, A., Fillinger, S., Patel, H., Alneberg, J., Wilm, A., Garcia, M. U., Di Tommaso, P., & Nahnsen, S. (2020). The nf-core framework for community-curated bioinformatics pipelines. *Nature Biotechnology*, *38*(3), 276–278. https://doi.org/10.1038/s41587-020-0439-x

Fatima, S. (2025). Tumor Microenvironment: A Complex Landscape of Cancer Development and Drug Resistance. *Cureus*, *17*(4), e82090. https://doi.org/10.7759/cureus.82090

Faye, A. S., Holmer, A. K., & Axelrad, J. E. (2022). Cancer in Inflammatory Bowel Disease. *Gastroenterology Clinics of North America*, *51*(3), 649–666. https://doi.org/10.1016/j.gtc.2022.05.003

Fearon, E. R., & Vogelstein, B. (1990). A genetic model for colorectal tumorigenesis. *Cell*, *61*(5), 759–767. https://doi.org/10.1016/0092-8674(90)90186-I

Fei and Propato, Propato, A. P., Lotti, G., Nardini, P., Guasti, D., Polvani, S., Bani, D., Galli, A., Casini, D., Cantini, G., Chiaramonti, D., & Luconi, M. (2025). Tailor-made Biochar enhances the anti-tumour effects of butyrate-glycerides in colorectal cancer. *Biomedicine & Pharmacotherapy*, *184*, 117900. https://doi.org/10.1016/j.biopha.2025.117900

Figueiredo, P., Donato, M., Urbano, M., Goulão, H., Gouveia, H., Sofia, C., Leitão, M., & Freitas, D. (2009). Aberrant crypt foci: Endoscopic assessment and cell kinetics characterization. *International Journal of Colorectal Disease*, *24*(4), 441–450. https://doi.org/10.1007/s00384-008-0576-z

Fujii, M., Matano, M., Nanki, K., & Sato, T. (2015). Efficient genetic engineering of human intestinal organoids using electroporation. *Nature Protocols*, *10*(10), 1474–1485. https://doi.org/10.1038/nprot.2015.088

Gates, T., Wangmo, D., Bergerud, K., Keel, B., Staley, C., & Subramanian, S. (2025). SMAD4 mutation drives gut microbiome shifts toward tumor progression in colorectal cancer. *Discover Oncology*, *16*. https://doi.org/10.1007/s12672-025-02580-6

Geng, H.-W., Yin, F.-Y., Zhang, Z.-F., Gong, X., & Yang, Y. (2021). Butyrate Suppresses Glucose Metabolism of Colorectal Cancer Cells via GPR109a-AKT Signaling Pathway and Enhances Chemotherapy. *Frontiers in Molecular Biosciences*, *8*. https://doi.org/10.3389/fmolb.2021.634874

Giglia, M. D., & Chu, D. I. (2016). Familial Colorectal Cancer: Understanding the Alphabet Soup. *Clinics in Colon and Rectal Surgery*, *29*(3), 185–195. https://doi.org/10.1055/s-0036-1584290

Gomes, S., Rodrigues, A. C., Pazienza, V., & Preto, A. (2023). Modulation of the Tumor Microenvironment by Microbiota-Derived Short-Chain Fatty Acids: Impact in Colorectal Cancer Therapy. *International Journal of Molecular Sciences*, *24*(6), 5069. https://doi.org/10.3390/ijms24065069

Goosenberg, E., Kaur, A., & Babiker, H. M. (2025). A Review of Hereditary Colorectal Cancers. In *StatPearls*. StatPearls Publishing. http://www.ncbi.nlm.nih.gov/books/NBK538195/

Grigoraș, A., & Amalinei, C. (2023). Multi-Faceted Role of Cancer-Associated Adipocytes in Colorectal Cancer. *Biomedicines*, *11*(9). https://doi.org/10.3390/biomedicines11092401

Hamilton, W., & Bailey, S. E. R. (2023). Colorectal cancer in symptomatic patients: How to improve the diagnostic pathway. *Best Practice & Research Clinical Gastroenterology, Colorectal cancer: From the prevention to treatment*, *66*, 101842. https://doi.org/10.1016/j.bpg.2023.101842

Han, B., Chai, Q., Chen, Q., Liu, M., Wang, T., Zhang, Y., Li, Z., Chen, Z., Li, B., Li, X., Sui, H., & Tang, Q. (2025). Sodium butyrate inhibits colorectal cancer development by reducing M2 macrophage polarization and PD-L1 expression. *mSystems*, *10*(12), e00692-25. https://doi.org/10.1128/msystems.00692-25

Hanahan, D., & Weinberg, R. A. (2011). Hallmarks of Cancer: The Next Generation. *Cell*, *144*(5), 646–674. https://doi.org/10.1016/j.cell.2011.02.013

Harada, S., & Morlote, D. (2020). Molecular Pathology of Colorectal Cancer. *Advances in Anatomic Pathology*, *27*(1), 20–26. https://doi.org/10.1097/PAP.0000000000000247

Harkins, J. M., & Sajjad, H. (2025). Anatomy, Abdomen and Pelvis, Sigmoid Colon. In *StatPearls*. StatPearls Publishing. http://www.ncbi.nlm.nih.gov/books/NBK549824/

He, X., & Xu, C. (2020). Immune checkpoint signaling and cancer immunotherapy. *Cell Research*, *30*(8), 660–669. https://doi.org/10.1038/s41422-020-0343-4

Hlavca, S., Chan, W. H., Engel, R. M., & Abud, H. E. (2024). Clusterin: A marker and mediator of chemoresistance in colorectal cancer. *Cancer Metastasis Reviews*, *43*(1), 379–391. https://doi.org/10.1007/s10555-024-10173-y

Hodgkinson, K., El Abbar, F., Dobranowski, P., Manoogian, J., Butcher, J., Figeys, D., Mack, D., & Stintzi, A. (2023). Butyrate's role in human health and the current progress towards its clinical application to treat gastrointestinal disease. *Clinical Nutrition (Edinburgh, Scotland)*, *42*(2), 61–75. https://doi.org/10.1016/j.clnu.2022.10.024

Hou, K., Wu, Z.-X., Chen, X.-Y., Wang, J.-Q., Zhang, D., Xiao, C., Zhu, D., Koya, J. B., Wei, L., Li, J., & Chen, Z.-S. (2022). Microbiota in health and diseases. *Signal Transduction and Targeted Therapy*, *7*(1), 135. https://doi.org/10.1038/s41392-022-00974-4

Jasperson, K. W., Tuohy, T. M., Neklason, D. W., & Burt, R. W. (2010). Hereditary and familial colon cancer. *Gastroenterology*, *138*(6), 2044–2058. https://doi.org/10.1053/j.gastro.2010.01.054

Jha, M. K., Joshi, S., Sharma, R. K., Kim, A. A., Pant, B., Park, M., & Pant, H. R. (2021). Surface Modified Activated Carbons: Sustainable Bio-Based Materials for Environmental Remediation. *Nanomaterials*, *11*(11), 3140. https://doi.org/10.3390/nano11113140

Ji, R., Ji, Y., Ma, L., Ge, S., Chen, J., Wu, S., Huang, T., Sheng, Y., Wang, L., Yi, N., & Liu, Z. (2021). Keratin 17 upregulation promotes cell metastasis and angiogenesis in colon adenocarcinoma. *Bioengineered*, *12*(2), 12598–12611. https://doi.org/10.1080/21655979.2021.2010393

Kim, T. H., Lim, S. H., Lee, H., Chae, Y. C., & Min, D. S. (2026). Metabolic crosstalk among cancer-associated fibroblasts, adipocytes and immune cells as an immunosuppressive tumor microenvironment driver. *Experimental & Molecular Medicine*, 1–16. https://doi.org/10.1038/s12276-026-01650-1

Korotkevich, G., Sukhov, V., & Sergushichev, A. (2019). *Fast gene set enrichment analysis* (p. 060012). bioRxiv. https://doi.org/10.1101/060012

Kranjec, C., Eilertsen, I. A., Nunes, L., Moosavi, S. H., Berg, K. C. G., Eknæs, M., Hektoen, M., Niederdorfer, B., Lind, G. E., Skotheim, R. I., Sveen, A., & Lothe, R. A. (2026). Common gene mutations in 103 authenticated colorectal cancer cell lines. *Oncogenesis*. https://doi.org/10.1038/s41389-026-00599-0

Kumar, A., Gautam, V., Sandhu, A., Rawat, K., Sharma, A., & Saha, L. (2023). Current and emerging therapeutic approaches for colorectal cancer: A comprehensive review. *World Journal of Gastrointestinal Surgery*, *15*(4), 495–519. https://doi.org/10.4240/wjgs.v15.i4.495

Kvakova, M., Kamlarova, A., Stofilova, J., Benetinova, V., & Bertkova, I. (2022). Probiotics and postbiotics in colorectal cancer: Prevention and complementary therapy. *World Journal of Gastroenterology*, *28*(27), 3370–3382. https://doi.org/10.3748/wjg.v28.i27.3370

Laskar, R. S., Murphy, N., Ferrari, P., Brennan, P., Cross, A. J., Guevara, M., Pala, V., Smith-Byrne, K., Tjønneland, A., Fortner, R. T., Braaten, T. B., Nøst, T. H., Skeie, G., Campbell, P. T., Gunter, M. J., & Borch, K. B. (2025). A prospective investigation of early-onset colorectal cancer risk factors–pooled analysis of three large-scale European cohorts. *British Journal of Cancer*. https://doi.org/10.1038/s41416-025-03303-y

Leiphrakpam, P. D., & Are, C. (2024). PI3K/Akt/mTOR Signaling Pathway as a Target for Colorectal Cancer Treatment. *International Journal of Molecular Sciences*, *25*(6), 3178. https://doi.org/10.3390/ijms25063178

Li, Q., Cao, L., Tian, Y., Zhang, P., Ding, C., Lu, W., Jia, C., Shao, C., Liu, W., Wang, D., Ye, H., & Hao, H. (2018). Butyrate Suppresses the Proliferation of Colorectal Cancer Cells via Targeting Pyruvate Kinase M2 and Metabolic Reprogramming. *Molecular & Cellular Proteomics : MCP*, *17*(8), 1531–1545. https://doi.org/10.1074/mcp.RA118.000752

Li, Q., Geng, S., Luo, H., Wang, W., Mo, Y.-Q., Luo, Q., Wang, L., Song, G.-B., Sheng, J.-P., & Xu, B. (2024). Signaling pathways involved in colorectal cancer: Pathogenesis and targeted therapy. *Signal Transduction and Targeted Therapy*, *9*(1), 266. https://doi.org/10.1038/s41392-024-01953-7

Li, X., Nadauld, L., Ootani, A., Corney, D. C., Pai, R. K., Gevaert, O., Cantrell, M. A., Rack, P. G., Neal, J. T., Chan, C. W.-M., Yeung, T., Gong, X., Yuan, J., Wilhelmy, J., Robine, S., Attardi, L. D., Plevritis, S. K., Hung, K. E., Chen, C.-Z., … Kuo, C. J. (2014). Oncogenic transformation of diverse gastrointestinal tissues in primary organoid culture. *Nature Medicine*, *20*(7), 769–777. https://doi.org/10.1038/nm.3585

Liang, J., Yang, C., Li, P., Zhang, M., Xie, X., Xie, X., Chen, Y., Wang, Q., Zhou, L., & Luo, X. (2023). Astragaloside IV inhibits AOM/DSS-induced colitis-associated tumorigenesis *via* activation of PPARγ signaling in mice. *Phytomedicine*, *121*, 155116. https://doi.org/10.1016/j.phymed.2023.155116

Liu, Y., Zhou, Y., Zhang, M., Zhang, J., Chen, J., Chen, L., Tian, J., Lv, X., Ma, X., Xu, J., Shi, J., & Chen, L. (2025). Tumor-secreted clusterin promotes cachectic fat wasting via disrupting circadian gene expression and adipogenesis. *The EMBO Journal*, *45*(3), 856–878. https://doi.org/10.1038/s44318-025-00661-4

Lopes, S. R., Martins, C., Santos, I. C., Teixeira, M., Gamito, É., & Alves, A. L. (2024). Colorectal cancer screening: A review of current knowledge and progress in research. *World Journal of Gastrointestinal Oncology*, *16*(4), 1119–1133. https://doi.org/10.4251/wjgo.v16.i4.1119

Love, M. I., Huber, W., & Anders, S. (2014). Moderated estimation of fold change and dispersion for RNA-seq data with DESeq2. *Genome Biology*, *15*(12), 550. https://doi.org/10.1186/s13059-014-0550-8

Luconi, M., Cantini, G., & Crescioli, C. (2025). Repurposing glucose-lowering drugs for cancer therapy. *Trends in Cancer*, *11*(7), 691–710. https://doi.org/10.1016/j.trecan.2025.04.010

Ludikhuize, M. C., Meerlo, M., Burgering, B. M. T., & Colman, M. J. R. (2021). Protocol to profile the bioenergetics of organoids using Seahorse. *STAR Protocols*, *2*(1). https://doi.org/10.1016/j.xpro.2021.100386

Ma, Y., Nenkov, M., Chen, Y., & Gaßler, N. (2024). The Role of Adipocytes Recruited as Part of Tumor Microenvironment in Promoting Colorectal Cancer Metastases. *International Journal of Molecular Sciences*, *25*(15), 8352. https://doi.org/10.3390/ijms25158352

Manzi, J., Hoff, C. O., Ferreira, R., Pimentel, A., Datta, J., Livingstone, A. S., Vianna, R., & Abreu, P. (2023). Targeted Therapies in Colorectal Cancer: Recent Advances in Biomarkers, Landmark Trials, and Future Perspectives. *Cancers*, *15*(11), 3023. https://doi.org/10.3390/cancers15113023

Maqbool, A. (2023). Colon: Structure, function, and disorders. In *Encyclopedia of Human Nutrition* (pp. 184–206). Elsevier. https://doi.org/10.1016/B978-0-12-821848-8.00059-7

Mármol, I., Sánchez-de-Diego, C., Pradilla Dieste, A., Cerrada, E., & Rodriguez Yoldi, M. (2017). Colorectal Carcinoma: A General Overview and Future Perspectives in Colorectal Cancer. *International Journal of Molecular Sciences*, *18*(1), 197. https://doi.org/10.3390/ijms18010197

Martinelli, S., Cantini, G., Propato, A. P., Bani, D., Guasti, D., Nardini, P., Calosi, L., Mello, T., Bechmann, N., Danza, G., Villanelli, F., Canu, L., Maggi, M., Mannelli, M., Rapizzi, E., & Luconi, M. (2024). The 3D in vitro Adrenoid cell model recapitulates the complexity of the adrenal gland. *Scientific Reports*, *14*(1), 8044. https://doi.org/10.1038/s41598-024-58664-w

Masters, J. R. (2000). Human cancer cell lines: Fact and fantasy. *Nature Reviews. Molecular Cell Biology*, *1*(3), 233–236. https://doi.org/10.1038/35043102

Matano, M., Date, S., Shimokawa, M., Takano, A., Fujii, M., Ohta, Y., Watanabe, T., Kanai, T., & Sato, T. (2015). Modeling colorectal cancer using CRISPR-Cas9–mediated engineering of human intestinal organoids. *Nature Medicine*, *21*(3), 256–262. https://doi.org/10.1038/nm.3802

Matsuda, T., Fujimoto, A., & Igarashi, Y. (2025). Colorectal Cancer: Epidemiology, Risk Factors, and Public Health Strategies. *Digestion*, *106*(2), 91–99. https://doi.org/10.1159/000543921

Matsumoto, T., Ikoma, T., Yamamura, S., Miura, K., Tsuduki, T., Watanabe, T., Nagai, H., Takatani, M., & Yasui, H. (2023). Regorafenib is suitable for advanced colorectal cancer patients who have previously received trifluridine/tipiracil plus bevacizumab. *Scientific Reports*, *13*(1), 2433. https://doi.org/10.1038/s41598-023-29706-6

McCabe, M. A., Mauro, A. J., & Schoen, R. E. (2025). Novel colorectal cancer screening methods—Opportunities and challenges. *Nature Reviews Clinical Oncology*, *22*(8), 581–591. https://doi.org/10.1038/s41571-025-01037-7

McLellan, E. A., & Bird, R. P. (1988). Aberrant crypts: Potential preneoplastic lesions in the murine colon. *Cancer Research*, *48*(21), 6187–6192.

McNabney, S. M., & Henagan, T. M. (2017a). Short Chain Fatty Acids in the Colon and Peripheral Tissues: A Focus on Butyrate, Colon Cancer, Obesity and Insulin Resistance. *Nutrients*, *9*(12), 1348. https://doi.org/10.3390/nu9121348

McNabney, S. M., & Henagan, T. M. (2017b). Short Chain Fatty Acids in the Colon and Peripheral Tissues: A Focus on Butyrate, Colon Cancer, Obesity and Insulin Resistance. *Nutrients*, *9*(12), 1348. https://doi.org/10.3390/nu9121348

Meng, M., Zhong, K., Jiang, T., Liu, Z., Kwan, H. Y., & Su, T. (2021). The current understanding on the impact of KRAS on colorectal cancer. *Biomedicine & Pharmacotherapy*, *140*, 111717. https://doi.org/10.1016/j.biopha.2021.111717

Menon, G., & Kasi, A. (2025). Familial Adenomatous Polyposis. In *StatPearls*. StatPearls Publishing. http://www.ncbi.nlm.nih.gov/books/NBK538233/

Miriyala, N., Ouyang, D., Perrie, Y., Lowry, D., & Kirby, D. J. (2017). Activated carbon as a carrier for amorphous drug delivery: Effect of drug characteristics and carrier wettability. *European Journal of Pharmaceutics and Biopharmaceutics*, *115*, 197–205. https://doi.org/10.1016/j.ejpb.2017.03.002

Mujtaba, G., Hayat, R., Hussain, Q., & Ahmed, M. (2021). Physio-Chemical Characterization of Biochar, Compost and Co-Composted Biochar Derived from Green Waste. *Sustainability*, *13*(9). https://doi.org/10.3390/su13094628

Müller, M. F., Ibrahim, A. E. K., & Arends, M. J. (2016). Molecular pathological classification of colorectal cancer. *Virchows Archiv*, *469*(2), 125–134. https://doi.org/10.1007/s00428-016-1956-3

Nagl, L., Horvath, L., Pircher, A., & Wolf, D. (2020). Tumor Endothelial Cells (TECs) as Potential Immune Directors of the Tumor Microenvironment – New Findings and Future Perspectives. *Frontiers in Cell and Developmental Biology*, *8*. https://doi.org/10.3389/fcell.2020.00766

Nair, P. S., P S, S. M., Suresh, S., A J, S., K, S., S, A. K., P R, A., Krishnan, N., S, P., Chakraborty, S., Chopra, H., Akash, S., Amin, R., Dey, A., Alagawany, M., Chandran, D., & Dhama, K. (2023). Beneficial impacts of biochar as a potential feed additive in animal husbandry. *Journal of Experimental Biology and Agricultural Sciences*, *11*(3), 479–499. https://doi.org/10.18006/2023.11(3).479.499

Nanda, S., Dalai, A. K., Berruti, F., & Kozinski, J. A. (2016). Biochar as an Exceptional Bioresource for Energy, Agronomy, Carbon Sequestration, Activated Carbon and Specialty Materials. *Waste and Biomass Valorization*, *7*(2), 201–235. https://doi.org/10.1007/s12649-015-9459-z

Nguyen, A. L., Lausten, M. A., & Boman, B. M. (2025). The Colonic Crypt: Cellular Dynamics and Signaling Pathways in Homeostasis and Cancer. *Cells*, *14*(18), 1428. https://doi.org/10.3390/cells14181428

Nisticò, C., & Chiarella, E. (2023). An Overview on Lipid Droplets Accumulation as Novel Target for Acute Myeloid Leukemia Therapy. *Biomedicines*, *11*(12), 3186. https://doi.org/10.3390/biomedicines11123186

Ogunwa, K. I., Nnadozie, E. C., Dube, N., Oladoye, P. O., & Obayomi, K. S. (2026). The evolving role of biochar: Recent advances and future directions - a review. *Biomass and Bioenergy*, *208*, 108844. https://doi.org/10.1016/j.biombioe.2025.108844

Olszańska, J., Pietraszek-Gremplewicz, K., Domagalski, M., & Nowak, D. (2023). Mutual impact of adipocytes and colorectal cancer cells growing in co-culture conditions. *Cell Communication and Signaling : CCS*, *21*, 130. https://doi.org/10.1186/s12964-023-01155-8

Panczyk, T., Wolski, P., & Lajtar, L. (2016). Coadsorption of Doxorubicin and Selected Dyes on Carbon Nanotubes. Theoretical Investigation of Potential Application as a pH-Controlled Drug Delivery System. *Langmuir*, *32*(19), 4719–4728. https://doi.org/10.1021/acs.langmuir.6b00296

Panwar, N. L., Pawar, A., & Salvi, B. L. (2019). Comprehensive review on production and utilization of biochar. *SN Applied Sciences*, *1*(2), 168. https://doi.org/10.1007/s42452-019-0172-6

Park, A., Kim, W. K., & Bae, K.-H. (2014). Distinction of white, beige and brown adipocytes derived from mesenchymal stem cells. *World Journal of Stem Cells*, *6*(1), 33–42. https://doi.org/10.4252/wjsc.v6.i1.33

Park, C. H., Eun, C. S., & Han, D. S. (2018). Intestinal microbiota, chronic inflammation, and colorectal cancer. *Intestinal Research*, *16*(3), 338–345. https://doi.org/10.5217/ir.2018.16.3.338

Park, J., Morley, T. S., Kim, M., Clegg, D. J., & Scherer, P. E. (2014). Obesity and cancer—Mechanisms underlying tumour progression and recurrence. *Nature Reviews Endocrinology*, *10*(8), 455–465. https://doi.org/10.1038/nrendo.2014.94

Pereira, J. F. S., Awatade, N. T., Loureiro, C. A., Matos, P., Amaral, M. D., & Jordan, P. (2016). The third dimension: New developments in cell culture models for colorectal research. *Cellular and Molecular Life Sciences*, *73*(21), 3971–3989. https://doi.org/10.1007/s00018-016-2258-2

Prasai, T. P., Walsh, K. B., Bhattarai, S. P., Midmore, D. J., Van, T. T. H., Moore, R. J., & Stanley, D. (2016). Biochar, Bentonite and Zeolite Supplemented Feeding of Layer Chickens Alters Intestinal Microbiota and Reduces Campylobacter Load. *PloS One*, *11*(4), e0154061. https://doi.org/10.1371/journal.pone.0154061

Qin, Y., Liu, L., Luo, S., He, H., Sun, X., Zhang, Q., Bian, Z., & Sun, S. (2025). Sodium butyrate induces colorectal cancer cell apoptosis via the MCU/Drp1 pathway. *International Immunopharmacology*, *161*, 115052. https://doi.org/10.1016/j.intimp.2025.115052

Rahman, M. A., Yadab, M. K., & Ali, M. M. (2024). Emerging Role of Extracellular pH in Tumor Microenvironment as a Therapeutic Target for Cancer Immunotherapy. *Cells*, *13*(22). https://doi.org/10.3390/cells13221924

Rao, J. N., & Wang, J.-Y. (2010). Intestinal Architecture and Development. In *Regulation of Gastrointestinal Mucosal Growth*. Morgan & Claypool Life Sciences. https://www.ncbi.nlm.nih.gov/books/NBK54098/

Requena, D. O., & Garcia-Buitrago, M. (2020). Molecular Insights Into Colorectal Carcinoma. *Archives of Medical Research, Cancer: A Chronic Pandemic*, *51*(8), 839–844. https://doi.org/10.1016/j.arcmed.2020.09.014

Rimoldi, S., Gliozheni, E., Ascione, C., Gini, E., & Terova, G. (2018). Effect of a specific composition of short- and medium-chain fatty acid 1-Monoglycerides on growth performances and gut microbiota of gilthead sea bream (Sparus aurata). *PeerJ*, *6*, e5355. https://doi.org/10.7717/peerj.5355

Rizzo, A. M., Pettorali, M., Nistri, R., & Chiaramonti, D. (2019). Mass and energy balances of an autothermal pilot carbonization unit. *Biomass and Bioenergy*, *120*, 144–155. https://doi.org/10.1016/j.biombioe.2018.11.009

Rizzo, G., Bertotti, A., Leto, S. M., & Vetrano, S. (2021). Patient-derived tumor models: A more suitable tool for pre-clinical studies in colorectal cancer. *Journal of Experimental & Clinical Cancer Research : CR*, *40*, 178. https://doi.org/10.1186/s13046-021-01970-2

Roy, M. K., Pipara, A., & Kumar, A. (2021). Surgical management of adenocarcinoma of the transverse colon: What should be the extent of resection? *Annals of Gastroenterological Surgery*, *5*(1), 24–31. https://doi.org/10.1002/ags3.12380

Sabol, R. A., Giacomelli, P., Beighley, A., & Bunnell, B. A. (2019). Adipose Stem Cells and Cancer: Concise Review. *STEM CELLS*, *37*(10), 1261–1266. https://doi.org/10.1002/stem.3050

Sahai, E., Astsaturov, I., Cukierman, E., DeNardo, D. G., Egeblad, M., Evans, R. M., Fearon, D., Greten, F. R., Hingorani, S. R., Hunter, T., Hynes, R. O., Jain, R. K., Janowitz, T., Jorgensen, C., Kimmelman, A. C., Kolonin, M. G., Maki, R. G., Powers, R. S., Puré, E., … Werb, Z. (2020). A framework for advancing our understanding of cancer-associated fibroblasts. *Nature Reviews Cancer*, *20*(3), 174–186. https://doi.org/10.1038/s41568-019-0238-1

Sato, T., & Clevers, H. (2013). Growing Self-Organizing Mini-Guts from a Single Intestinal Stem Cell: Mechanism and Applications. *Science*, *340*(6137), 1190–1194. https://doi.org/10.1126/science.1234852

Sato, T., Stange, D. E., Ferrante, M., Vries, R. G. J., van Es, J. H., van den Brink, S., van Houdt, W. J., Pronk, A., van Gorp, J., Siersema, P. D., & Clevers, H. (2011). Long-term Expansion of Epithelial Organoids From Human Colon, Adenoma, Adenocarcinoma, and Barrett's Epithelium. *Gastroenterology*, *141*(5), 1762–1772. https://doi.org/10.1053/j.gastro.2011.07.050

Sato, T., Vries, R. G., Snippert, H. J., van de Wetering, M., Barker, N., Stange, D. E., van Es, J. H., Abo, A., Kujala, P., Peters, P. J., & Clevers, H. (2009). Single Lgr5 stem cells build crypt-villus structures in vitro without a mesenchymal niche. *Nature*, *459*(7244), 262–265. https://doi.org/10.1038/nature07935

Sawicki, T., Ruszkowska, M., Danielewicz, A., Niedźwiedzka, E., Arłukowicz, T., & Przybyłowicz, K. E. (2021). A Review of Colorectal Cancer in Terms of Epidemiology, Risk Factors, Development, Symptoms and Diagnosis. *Cancers*, *13*(9), 2025. https://doi.org/10.3390/cancers13092025

Shin, Y., Han, S., Kwon, J., Ju, S., Choi, T. G., Kang, I., & Kim, S. S. (2023). Roles of Short-Chain Fatty Acids in Inflammatory Bowel Disease. *Nutrients*, *15*(20), 4466. https://doi.org/10.3390/nu15204466

Siegel, R. L., Wagle, N. S., & Jemal, A. (2026). Leading Cancer Deaths in People Younger Than 50 Years. *JAMA*, *335*(7), 632–634. https://doi.org/10.1001/jama.2025.25467

Singh, G., Chaudhry, Z., Boyadzhyan, A., Sasaninia, K., & Rai, V. (2025). Dysbiosis and colorectal cancer: Conducive factors, biological and molecular role, and therapeutic prospectives. *Exploration of Targeted Anti-Tumor Therapy*, *6*, 1002329. https://doi.org/10.37349/etat.2025.1002329

Slama, Y., Ah-Pine, F., Khettab, M., Arcambal, A., Begue, M., Dutheil, F., & Gasque, P. (2023). The Dual Role of Mesenchymal Stem Cells in Cancer Pathophysiology: Pro-Tumorigenic Effects versus Therapeutic Potential. *International Journal of Molecular Sciences*, *24*(17), 13511. https://doi.org/10.3390/ijms241713511

Solano-Umaña, V., & Vega-Baudrit, J. R. (2015). Micro, Meso and Macro Porous Materials on Medicine. *Journal of Biomaterials and Nanobiotechnology*, *6*(4), Articolo 4. https://doi.org/10.4236/jbnb.2015.64023

Sun, J., Chen, S., Zang, D., Sun, H., Sun, Y., & Chen, J. (2024). Butyrate as a promising therapeutic target in cancer: From pathogenesis to clinic (Review). *International Journal of Oncology*, *64*(4), 44. https://doi.org/10.3892/ijo.2024.5632

Sung, M., Park, E., Choi, Y., Hwang, J., & Oh, E.-S. (2025). Regional Differences in Structure, Function, and Inflammatory Response of the Large Intestine. *Innovations in Acupuncture and Medicine*, *18*(1), 6. https://doi.org/10.1186/s44424-025-00006-2

Sveen, A., Bruun, J., Eide, P. W., Eilertsen, I. A., Ramirez, L., Murumägi, A., Arjama, M., Danielsen, S. A., Kryeziu, K., Elez, E., Tabernero, J., Guinney, J., Palmer, H. G., Nesbakken, A., Kallioniemi, O., Dienstmann, R., & Lothe, R. A. (2018). Colorectal Cancer Consensus Molecular Subtypes Translated to Preclinical Models Uncover Potentially Targetable Cancer Cell Dependencies. *Clinical Cancer Research: An Official Journal of the American Association for Cancer Research*, *24*(4), 794–806. https://doi.org/10.1158/1078-0432.CCR-17-1234

Symonds, E. L., Dix, M., Wassie, M. M., Bulamu, N. B., Young, G. P., & Winter, J. M. (2025). Is blood the new stool? Status of blood tests for CRC screening. *Best Practice & Research Clinical Gastroenterology*, 102049. https://doi.org/10.1016/j.bpg.2025.102049

Tabuso, M., Homer-Vanniasinkam, S., Adya, R., & Arasaradnam, R. P. (2017). Role of tissue microenvironment resident adipocytes in colon cancer. *World Journal of Gastroenterology*, *23*(32), 5829–5835. https://doi.org/10.3748/wjg.v23.i32.5829

Thanki, K., Nicholls, M. E., Gajjar, A., Senagore, A. J., Qiu, S., Szabo, C., Hellmich, M. R., & Chao, C. (2017). Consensus Molecular Subtypes of Colorectal Cancer and their Clinical Implications. *International biological and biomedical journal*, *3*(3), 105–111.

Thomas, E. M., Wright, J. A., Blake, S. J., Page, A. J., Worthley, D. L., & Woods, S. L. (2023). Advancing translational research for colorectal immuno-oncology. *British Journal of Cancer*, *129*(9), 1442–1450. https://doi.org/10.1038/s41416-023-02392-x

Thrumurthy, S. G., Thrumurthy, S. S. D., Gilbert, C. E., Ross, P., & Haji, A. (2016). Colorectal adenocarcinoma: Risks, prevention and diagnosis. *BMJ*, i3590. https://doi.org/10.1136/bmj.i3590

Tong, G.-J., Zhang, G.-Y., Liu, J., Zheng, Z.-Z., Chen, Y., Niu, P.-P., & Xu, X.-T. (2018). Comparison of the eighth version of the American Joint Committee on Cancer manual to the seventh version for colorectal cancer: A retrospective review of our data. *World Journal of Clinical Oncology*, *9*(7), 148–161. https://doi.org/10.5306/wjco.v9.i7.148

Toor, S. M., Sasidharan Nair, V., Decock, J., & Elkord, E. (2020). Immune checkpoints in the tumor microenvironment. *Seminars in Cancer Biology, Resistance mechanisms to cancer immunotherapy*, *65*, 1–12. https://doi.org/10.1016/j.semcancer.2019.06.021

Valdeolivas, A., Amberg, B., Giroud, N., Richardson, M., Gálvez, E. J. C., Badillo, S., Julien-Laferrière, A., Túrós, D., Voith von Voithenberg, L., Wells, I., Pesti, B., Lo, A. A., Yángüez, E., Das Thakur, M., Bscheider, M., Sultan, M., Kumpesa, N., Jacobsen, B., Bergauer, T., … Hahn, K. (2024). Profiling the heterogeneity of colorectal cancer consensus molecular subtypes using spatial transcriptomics. *Npj Precision Oncology*, *8*(1), 10. https://doi.org/10.1038/s41698-023-00488-4

Vancamelbeke, M., & Vermeire, S. (2017). The intestinal barrier: A fundamental role in health and disease. *Expert review of gastroenterology & hepatology*, *11*(9), 821–834. https://doi.org/10.1080/17474124.2017.1343143

Vara, J. Á. F., Casado, E., Castro, J. de, Cejas, P., Belda-Iniesta, C., & González-Barón, M. (2004). PI3K/Akt signalling pathway and cancer. *Cancer Treatment Reviews*, *30*(2), 193–204. https://doi.org/10.1016/j.ctrv.2003.07.007

Virtanen, K. A., Lidell, M. E., Orava, J., Heglind, M., Westergren, R., Niemi, T., Taittonen, M., Laine, J., Savisto, N.-J., Enerbäck, S., & Nuutila, P. (2009). Functional Brown Adipose Tissue in Healthy Adults. *New England Journal of Medicine*, *360*(15), 1518–1525. https://doi.org/10.1056/NEJMoa0808949

Wang, C., Lv, T., Jin, B., Li, Y., & Fan, Z. (2025a). Regulatory role of PPAR in colorectal cancer. *Cell Death Discovery*, *11*(1), 28. https://doi.org/10.1038/s41420-025-02313-2

Wang, C., Lv, T., Jin, B., Li, Y., & Fan, Z. (2025b). Regulatory role of PPAR in colorectal cancer. *Cell Death Discovery*, *11*(1), 28. https://doi.org/10.1038/s41420-025-02313-2

Wang, D., & DuBois, R. N. (2010). Peroxisome proliferator-activated receptors in chronic inflammation and colorectal cancer. *Gastroenterology clinics of North America*, *39*(3), 697–707. https://doi.org/10.1016/j.gtc.2010.08.014

Wang, E., Xiang, K., Zhang, Y., & Wang, X.-F. (2022). Patient-derived organoids (PDOs) and PDO-derived xenografts (PDOXs): New opportunities in establishing faithful pre-clinical cancer models. *Journal of the National Cancer Center*, *2*(4), 263–276. https://doi.org/10.1016/j.jncc.2022.10.001

Wang, F., Song, Y., Huang, J., Wu, B., Wang, Y., Pang, Y., Zhang, W., Zhu, Z., Ma, F., Wang, X., & Zhang, X. (2021). Lollipop-Inspired Multilayered Drug Delivery Hydrogel for Dual Effective, Long-Term, and NIR-Defined Glaucoma Treatment. *Macromolecular Bioscience*, *21*(11), 2100202. https://doi.org/10.1002/mabi.202100202

Wang, P., Du, K., Tian, Y., Qiao, X., Yang, Y., Zheng, G., He, W., Kang, J., Zhang, J., Zhang, Z., Feng, F., & Zheng, J. (2026). Multi-omics analysis reveals that FABP2 suppresses colorectal cancer progression by regulating sphingomyelin metabolism via the PPAR signaling pathway. *Cancer Cell International*, *26*, 98. https://doi.org/10.1186/s12935-025-04159-1

Wang, W., Lokman, N. A., Barry, S. C., Oehler, M. K., & Ricciardelli, C. (2025). LGR5: An emerging therapeutic target for cancer metastasis and chemotherapy resistance. *Cancer and Metastasis Reviews*, *44*(1), 23. https://doi.org/10.1007/s10555-024-10239-x

Wang, Y.-X., Zhu, N., Zhang, C.-J., Wang, Y.-K., Wu, H.-T., Li, Q., Du, K., Liao, D.-F., & Qin, L. (2019). Friend or foe: Multiple roles of adipose tissue in cancer formation and progression. *Journal of Cellular Physiology*, *234*(12), 21436–21449. https://doi.org/10.1002/jcp.28776

Wei, H.-J., Zeng, R., Lu, J.-H., Lai, W.-F. T., Chen, W.-H., Liu, H.-Y., Chang, Y.-T., & Deng, W.-P. (2015). Adipose-derived stem cells promote tumor initiation and accelerate tumor growth by interleukin-6 production. *Oncotarget*, *6*(10), 7713–7726. https://doi.org/10.18632/oncotarget.3481

Wen, Y.-A., Xing, X., Harris, J. W., Zaytseva, Y. Y., Mitov, M. I., Napier, D. L., Weiss, H. L., Mark Evers, B., & Gao, T. (2017). Adipocytes activate mitochondrial fatty acid oxidation and autophagy to promote tumor growth in colon cancer. *Cell Death & Disease*, *8*(2), e2593–e2593. https://doi.org/10.1038/cddis.2017.21

Worthley, D. L., & Leggett, B. A. (2010). Colorectal Cancer: Molecular Features and Clinical Opportunities. *The Clinical Biochemist Reviews*, *31*(2), 31–38.

Wu, Q., Li, B., Li, Z., Li, J., Sun, S., & Sun, S. (2019). Cancer-associated adipocytes: Key players in breast cancer progression. *Journal of Hematology & Oncology*, *12*(1), 95. https://doi.org/10.1186/s13045-019-0778-6

Xie, Y.-H., Chen, Y.-X., & Fang, J.-Y. (2020). Comprehensive review of targeted therapy for colorectal cancer. *Signal Transduction and Targeted Therapy*, *5*(1), 22. https://doi.org/10.1038/s41392-020-0116-z

Yan, H., Liu, J., Zhang, Y., Chen, S., Xu, J., Gao, D., Li, H., Fang, X., Wang, Y., Wang, H., & Wang, H. (2024). Efficacy and safety of regorafenib in the treatment of metastatic colorectal cancer: A retrospective cohort study. *Journal of Gastrointestinal Oncology*, *15*(3), 987–1001. https://doi.org/10.21037/jgo-24-180

Yan, S., Wang, W., Feng, Z., Xue, J., Liang, W., Wu, X., Tan, Z., Zhang, X., Zhang, S., Li, X., & Zhang, C. (2024). Immune checkpoint inhibitors in colorectal cancer: Limitation and challenges. *Frontiers in Immunology*, *15*. https://doi.org/10.3389/fimmu.2024.1403533

Yang, X., Yin, F., Yang, Y., Lepp, D., Yu, H., Ruan, Z., Yang, C., Yin, Y., Hou, Y., Leeson, S., & Gong, J. (2018). Dietary butyrate glycerides modulate intestinal microbiota composition and serum metabolites in broilers. *Scientific Reports*, *8*(1), 4940. https://doi.org/10.1038/s41598-018-22565-6

Yoon, K., & Kim, N. (2018). The Effect of Microbiota on Colon Carcinogenesis. *Journal of Cancer Prevention*, *23*(3), 117–125. https://doi.org/10.15430/JCP.2018.23.3.117

Zhan, T., Rindtorff, N., & Boutros, M. (2017). Wnt signaling in cancer. *Oncogene*, *36*(11), 1461–1473. https://doi.org/10.1038/onc.2016.304

Zhao, Q., Lin, Y., Han, N., Li, X., Geng, H., Wang, X., Cui, Y., & Wang, S. (2017). Mesoporous carbon nanomaterials in drug delivery and biomedical application. *Drug Delivery*, *24*(sup1), 94–107. https://doi.org/10.1080/10717544.2017.1399300

Zheng, H.-C., Xue, H., & Zhang, C.-Y. (2022). REG4 promotes the proliferation and anti-apoptosis of cancer. *Frontiers in Cell and Developmental Biology*, *10*. https://doi.org/10.3389/fcell.2022.1012193

Zhu, X., Li, C., Li, J., Xie, B., Lü, J., & Li, Y. (2018). Thermal treatment of biochar in the air/nitrogen atmosphere for developed mesoporosity and enhanced adsorption to tetracycline. *Bioresource Technology*, *263*, 475–482. https://doi.org/10.1016/j.biortech.2018.05.041

Zhuo, Q., Liang, Y., Hu, Y., Shi, M., Zhao, C., & Zhang, S. (2023). Applications of biochar in medical and related environmental fields: Current status and future perspectives. *Carbon Research*, *2*(1), 32. https://doi.org/10.1007/s44246-023-00066-0

7.1 Online references

https://cancer-screening-and-care.jrc.ec.europa.eu/en/ecicc/european-colorectal-cancer-guidelines?topic=345&usertype=282

https://www.worldgastroenterology.org/guidelines/colorectal-cancer-screening/colorectal-cancer-screening-english

SEER*Explorer: An interactive website for SEER cancer statistics [Internet]. Surveillance Research Program, National Cancer Institute; 2025 Apr 16. [updated: 2026 Jan 8; cited 2026 Feb 12]. Available from: https://seer.cancer.gov/statistics-network/explorer/. Data source(s): SEER Incidence Data, November 2024 Submission (1975-2022), SEER 21 registries (excluding Illinois). Expected Survival Life Tables by Socio-Economic Standards.

https://www.wcrf.org/wp-content/uploads/2024/10/Body-fatness-and-weight-gain_0.pdf

GeneCards – the human gene database (www.genecards.org)

https://www.bio-rad-antibodies.com/measuring-cytotoxicity-proliferation spectrophotometry-fluorescence-alamarblue.html

Posit team (2025). RStudio: Integrated Development Environment for R. Posit Softwar, PBC, Boston, MA. URL http://www.posit.co/.

8. Acknowledgements

I would like to express my gratitude to my supervisor, Prof. Michaela Luconi, for her guidance and support throughout this research. I am also grateful to my tutor, Dr. Giulia Cantini, and my lab colleagues, Chiara Lepri and Anna Aurora Dedonno, for creating such an extremely supporting environment. I am deeply grateful to Dr. Kevin Myant and the entire lab group, with a special mention to Dr. Sebastian Pohl, for hosting me at the Institute of Genetics and Cancer (University of Edinburgh) during my PhD period abroad; they provided crucial help in producing the data for this thesis. The opportunity to work in such a stimulating environment has been invaluable for my academic growth and helped to make this wonderful experience in this marvellous city even more special.

La borsa di dottorato è stata finanziata con risorse dell'Unione europea-*NextGeneration EU*
Piano Nazionale di Ripresa e Resilienza Missione 4 – Componente 2 – "Dalla ricerca all'impresa" –
Investimento 1.5 - THE - Tuscany Health Ecosystem - ECS00000017 – *CUP B83C22003920001*